

STRUCTURAL INVESTIGATION  
OF STAR POLYMER NETWORKS  
USING NMR AND SAXS

Dissertation

zur Erlangung des akademischen Grades *doctor  
rerum naturalium* (Dr. rer. nat.)

der

Naturwissenschaftlichen Fakultät II  
Chemie, Physik und Mathematik  
der Martin-Luther-Universität  
Halle-Wittenberg

vorgelegt von

Lucas Löser

- 
1. Gutachter: Prof. Dr. Kay Saalwächter
  2. Gutachter: Prof. Dr. Dariush Hinderberger
  3. Gutachter: Prof. Dr. Michael Gradzielski

Öffentliche Verteidigung: 20.06.2024



## ABSTRACT

---

In this thesis, the structure of different polymer gels consisting of star precursors is investigated using  $^1\text{H}$ -NMR and small-angle x-ray scattering (SAXS). Due to their ability of potentially forming networks with a predictable model-like structure, they provide a promising toolbox for wet applications such as biological matrices, separation membranes, water desalination, or drug-release systems. To better understand the fundamental properties of such networks, and ultimately optimize them for applications, we rely on model-like structures, thus motivating research of methods that can provide quantitative information on the local chain-level architecture of these type of gels. To this end,  $^1\text{H}$  Multi-Quantum NMR is used to extract quantitative information on the connectivity motif distribution for different variations of gels synthesized utilizing both permanent and transient crosslinks. To better understand the influence of the synthesis conditions on the emerging network structure, variations on preparation concentration, temperature, solvent, and precursors were investigated. The results are complemented by an in-depth structural investigation of the amphiphilic tetraPEG-tetraPCL system using Pulsed-Field Gradient NMR for the characterization of the diffusion of probe molecules and SAXS for an estimate on correlation length and length scales of microphase separation. Both methods were performed with the network being swollen in selective (water) and nonselective (toluene) solvents, allowing for a comparison of these parameters. Finally,  $^1\text{H}$  MAS DQ NMR is used to demonstrate an immobilization effect of the PEG chain along the PCL cluster surface.

## ZUSAMMENFASSUNG

---

In dieser Arbeit wird die Struktur verschiedener Polymergele, die aus Sternpolymeren bestehen, untersucht. Dafür werden  $^1\text{H}$ -NMR und Röntgenkleinwinkelstreuung (SAXS) verwendet. Aufgrund ihres Potenzials, Netzwerke mit einer vorhersagbaren und modellartigen Struktur zu bilden, stellen sie eine vielversprechende Grundlage für lösemittelhaltige Anwendungen wie biologische Matrizen, Trennmembranen, Wasserentsalzung oder Drug-Release-Systemen dar. Um die grundlegenden Eigenschaften solcher Netzwerke besser zu verstehen und sie für Anwendungen zu optimieren, sind modellartige Netzwerke unabdingbar. Daher werden Methoden benötigt, die quantitative Informationen über die lokale Netzwerkstruktur von Gelen auf Kettenebene liefern können. Hierfür wird  $^1\text{H}$ -Multiquanten-NMR verwendet, um die Verteilung der Konnektivitätsmotive für verschiedene Varianten von Gelen (permanent und transient vernetzt) zu quantifizieren. Um den Einfluss der Synthesebedingungen auf die entstehende Netzwerkstruktur besser zu verstehen, wurden Variationen in Präparationskonzentration, Temperatur, Lösungsmittel und Sternpolymeren untersucht. Die Ergebnisse werden durch eine detaillierte strukturelle Untersuchung des amphiphilen TetraPEG-TetraPCL-Systems ergänzt. Hierbei wurden Feldgradienten-NMR zur Charakterisierung der Diffusion von Sondenmolekülen und SAXS zur Abschätzung von Korrelationslänge und Längenskala der Mikrophasenseparation eingesetzt. Um einen Vergleich der genannten Parameter im präparierten und phasenseparierten Zustand zu ermöglichen, werden beide Methoden sowohl im nicht-selektiven Lösemittel (Toluol) als auch im selektiven Lösemittel (Wasser) angewendet. Zusätzlich wurde mittels  $^1\text{H}$  MAS DQ NMR im phasenseparierten Zustand ein Immobilisierungseffekt der PEG-Ketten entlang der PCL-Clusteroberfläche festgestellt.



# PUBLIKATIONEN

---

Parts of this thesis were published in the following articles:

- [1] Mostafa Ahmadi, Lucas Löser, Karl Fischer, Kay Saalwächter, Sebastian Seiffert, "*Connectivity Defects and Collective Assemblies in Model Metallo-Supramolecular Dual-Network Hydrogels*", *Macromol. Chem. Phys.* 2020, 221, 1900400.
- [2] Paola Nicoletta, Martha Franziska Koziol, Lucas Löser, Kay Saalwächter, Mostafa Ahmadi, Sebastian Seiffert, "*Defect-controlled softness, diffusive permeability, and mesh-topology of metallo-supramolecular hydrogels*", *Soft Matter* 2022 18: 1071-1081.
- [3] Michael Lang, Reinhard Scholz, Lucas Löser, Carolin Bunk, Nora Fribiczter, Sebastian Seiffert, Frank Böhme, and Kay Saalwächter, "*Swelling and Residual Bond Orientations of Polymer Model Gels: The Entanglement-Free Limit*", *Macromolecules* 2022 55 (14), 5997-6014.
- [4] Carolin Bunk, Lucas Löser, Nora Fribiczter, Hartmut Komber, Lothar Jakisch, Reinhard Scholz, Brigitte Voit, Sebastian Seiffert, Kay Saalwächter, Michael Lang, and Frank Böhme, "*Amphiphilic Model Networks Based on PEG and PCL Tetra-arm Star Polymers with Complementary Reactivity*", *Macromolecules* 2022 55 (15), 6573-6589.
- [5] Mostafa Ahmadi, Lucas Löser, Gerard Pareras, Albert Poater, Kay Saalwächter, and Sebastian Seiffert, "*Connectivity Defects in Metallo-Supramolecular Polymer Networks at Different Self-Sorting Regimes*", *Chemistry of Materials* 2023 35 (10), 4026-4037.
- [6] Lucas Löser, Reinhard Scholz, Carolin Bunk, Frank Böhme, Michael Lang, Kay Saalwächter, "*Structural Characterization of amphiphilic co-networks in selective and non-selective solvents using  $^1\text{H-NMR}$  and SAXS*", *Macromolecules* 2024 57 (3), 940-954.
- [7] Carolin Bunk, Nora Fribiczter, Lucas Löser, Martin Geisler, Brigitte Voit, Sebastian Seiffert, Kay Saalwächter, Michael Lang, Frank Böhme, "*Amphiphilic Polymer Co-networks Based on crosslinked tetra-PEG-b-PCL Star Block Copolymers*", *Polymer* 2024 304, 127149.
- [8] Zhao Meng, Lucas Löser, Kay Saalwächter, Urs Gasser, Harm-Anton Klok, "*Disulfide-Crosslinked Tetra-PEG Gels*", *Macromolecules* 2024 57 (7), 3058-3065.

# Contents

<b>1</b>	<b>Introduction</b>	<b>1</b>
<b>2</b>	<b>Polymer chains and networks</b>	<b>6</b>
2.1	Polymer chains: Conformations and length scales . . . . .	6
2.2	Thermodynamic properties of polymers in solution . . . . .	9
2.3	Star polymer networks . . . . .	15
<b>3</b>	<b>NMR methodology</b>	<b>22</b>
3.1	Basic principles . . . . .	22
3.2	Dipolar interaction in solid-state NMR . . . . .	23
3.3	Relationship of dipolar interactions and local chain motion . . . . .	25
3.4	Static $^1\text{H}$ MQ NMR . . . . .	27
3.5	$^1\text{H}$ MAS DQ-NMR: The POST-C7 Experiment . . . . .	31
3.6	Pulsed-Field Gradient NMR . . . . .	34
<b>4</b>	<b>X-Ray Scattering</b>	<b>38</b>
4.1	Basic Concepts of X-Ray Scattering (SAXS) . . . . .	38
4.2	SAXS as a Tool for Polymer Network Characterization . . . . .	41
<b>5</b>	<b>Samples and experimental setup</b>	<b>46</b>
5.1	Samples . . . . .	46
5.2	Experimental setup . . . . .	48
<b>6</b>	<b>Chain-level investigation of gels using MQ-NMR</b>	<b>52</b>
6.1	Improvements of the Baum-Pines evaluation procedure . . . . .	52
6.2	Model tPEG-tPEG and amphiphilic tPEG-tPCL co-networks . . . . .	56
6.3	Hydrogels from homocomplementary tPEG precursors . . . . .	67
6.4	Quantification of ion-mediated structures in metal dual-networks . . . . .	71
6.5	Defect-controlled transient tPEG networks . . . . .	77
6.6	Connectivity motifs of transient networks at different self-sorting regimes . . . . .	81
<b>7</b>	<b>Structural investigation of ACPNs</b>	<b>87</b>
7.1	SAXS on swollen polymer networks . . . . .	87
7.2	Diffusion of probe molecules inside a polymer matrix . . . . .	95
7.3	MAS DQ NMR for phase-specific estimates of dipolar couplings . . . . .	104
<b>8</b>	<b>Summary</b>	<b>108</b>
	<b>References</b>	<b>110</b>

# Chapter 1

## Introduction

Polymer networks are three-dimensional structures emerging from permanent or transient crosslinking of polymeric precursors with more than two functional sites per precursor. For that, telechelic polymer chains ('strands') are crosslinked with functional groups ('junctions' with a given *functionality*  $f$ ) in order to constitute a macroscopic 'infinite polymer' (the network). Due to the typically high flexibility and large conformational space of the strands, a high degree of entropic elasticity is achieved, yielding a flexible material suitable to countless applications of the modern age [1, 2]. By combining different monomer architectures, crosslinking methods and other chemical variables, a plentiful toolbox of building blocks is available for producing networks with different properties [3, 4]. While the choice of the specific precursor broadly dictates the type of network and its solution properties (e.g., what is considered a "good solvent" or a "poor solvent"), the size of the network strands and the choice of crosslinking method are factors that strongly determine the mechanical properties such as the elastic modulus and stretchability [5]. Especially for transiently-linked networks, the kinetics of the linking agent determines the timescale of elastic response and flow [6–8].

### Polymer gels

A popular subclass of polymer networks are polymer gels, which constitute networks that are swollen in a solvent with the solvent commonly being the majority volume fraction of the system. As an approximation, their high degree of swelling is determined by a balance of the entropic elasticity of the chain and the free energy of mixing dominated by the solvent quality [9]. With high equilibrium degree of swellings beyond up to hundreds of times of their dry weight [10], they are uniquely suitable to wet applications, including e.g., superabsorbers [10], water desalination [11] or translational applications in the medical sector [12]. A subset of swollen polymer gels is constructed by exchanging parts of the precursors with a precursor of different polarity, resulting in the synthesis of an amphiphilic structure - so called *amphiphilic polymer co-networks* (APCNs). Their unique solution behavior makes them especially interesting for applications requiring phase-specific molecular transport, such as eye lens material [13], conductive layers in batteries [14], separation membranes [15], cell growth matrices [16, 17] or drug-release systems [18].

It is immediately apparent that most of these applications rely on a predictable and efficient

polymer-solvent interaction (e.g., equilibrium degree of swelling or efficient diffusion of surrounding liquid/probe molecule) or a certain mechanical strength, both of which depend on a controlled and reproducible network architecture that will be addressed later on in more detail. To this end, many different synthesis strategies were successfully pursued to better understand the relationship of synthesis and remove this restrictive factor, paving the way for more advanced applications. Early works pursuing this path by mentioning the idea of *model networks* with a controlled crosslink molecular weight and crosslink density date back until at least 1976, where Allen et al. [19] synthesized model polyurethane networks made from linear and trifunctional precursors, already discussing the impact of cyclic chain defects ("closed loop structures within the network") on the elastic modulus. Only one year later, Mark et al. [20] published on a model PDMS network already making use of tetrafunctional precursors while trying to reduce entanglements between the chains. A major improvement was achieved by the team of Takamasa Sakai in 2008 [21], who developed a procedure where two different 4-functional PEG precursors ("tetra-PEG" or "tPEG") are heterocomplementary end-linked for achieving a network with low overall defect content (in the sense of dangling chain ends) and high homogeneity [22]. The success of this synthesis is attributed to two facts: Usage of a heterocomplementary synthesis (also called A-B type synthesis) prevents highly probable intra-precursor end-linking reactions that result in elastically inactive structures, while the usage of multifunctional precursors with  $f > 2$  (here  $f = 4$ ) suppresses another probable elastically inactive loop defect where a linear chain would occupy two functional groups of the same precursor. Nevertheless, a combined NMR and Monte Carlo simulation study of Lange et al. [23] in 2011 revealed, that even in this case, major contributions from other cyclic connectivity defects (e.g., the end-linking of more than one arm between two given precursors) remain and influence the mechanical properties of the emerging gel [24, 25].

Since then, many variations of these two important key messages from the study of Sakai et al. have been published, resulting in a wide range of networks and synthetic procedures currently available. As reviewed in detail by Nakagawa et al. [3], these include both chemically-crosslinked variations [26–29], systems that vary the functionality of the precursors [30–32] or transiently-crosslinked variations (using e.g., ion-mediated bonds) [33, 34]. The latter systems are of special interest, as their transient links enable a degree of self-repair by structure equilibration, thus potentially reducing network defects [35, 36].

For the aforementioned special subclass, ACPNs, where precursors of different polarity are linked, an additional challenge in the form of proper solubilization and mixing of the precursors may arise. Most commonly, this is circumvented by adding a common good solvent in combination with varying synthetic approaches. Pioneering experiments for the synthesis of model ACPNs were done in the 1980s [37], using living carbocationic polymerization [38], whereas today a variety of approaches has been investigated, such as fast click-reactions [39–41], condensation reactions [42, 43], GTP [44], RAFT [45] or end-linking using small crosslinkers [46]. In this work, the comparably slow heterocomplementary end-linking of benzoxazinone- / amino-terminated star precursors is investigated in more detail [47].

## Structural investigation of polymer gels

Due to the complex structure of polymer gels, spanning length scales from the near molecular chain-level (1 – 10 nm) up to level of multiple junctions (10 – 100 nm), a multitude of methods has been developed to characterize both the network structure and the application properties. In this work only the former will be treated and discussed (although some of these methods will be applicable to both topics).

It is known that the chain-level structure and its corresponding defects (e.g., unreacted chain ends and cyclic defects) have a significant impact on the emerging mechanical properties of the network due to their influence on the chain-level elasticity with the details yet to be fully understood [24, 25]. However, research on the architecture of networks on this scale is still ongoing due to the difficulty in accessing these. While different methods such as simulations [48] or mechanical experiments [49] are used to deduce chain-level information, these strictly rely on strong assumptions that cannot always be tested [50] such as the type of deformation (affine or phantom model) or are strong simplifications (e.g., neglecting elastically active loop defects). Recently, the analysis of the non-linear deformation response for the analysis of "stress-supporting strands" joined this toolbox, while remaining yet to be applied more frequently [51]. So far, there are only two methods that can successfully infer fractions of cyclic defects from a single measurement. One of these is Network Disassembly Spectroscopy (NDS), which quantifies these by preparing a chemically labelled network, which after gelation will be cleaved ('disassembled') and the cleaved products will be analyzed in terms of molar mass. By precise positioning of the cleaving sites along the backbone, this can result in a precise quantification of dangling ends as well as higher order loop structures [52]. The second is solid-state MQ NMR (see e.g., refs. [23, 53, 54]), which analyzes the residual dipolar order remaining due to anisotropic chain motion in solids. Different topological features can be distinguished via an effective molecular weight - induced contrast between the cyclic defect structures or/and via differences in their relaxation dynamics [55]. Quantification of defect structures using MQ NMR will be a major topic of this work.

For the characterization of the network structure beyond the chain-level scale, scattering methods have continuously proven themselves to be one of the most informative methods (see e.g., the review of Seiffert [56]). For swollen networks without crystalline moieties a focus is put on small-angle x-ray scattering (SAXS) and small-angle neutron scattering (SANS) with the former being extensively used in this work. While correlations between junctions themselves are not observed due to a lack of scattering contrast, it can yield information about the correlation length  $\xi_c$  or frozen inhomogeneities  $\Xi$ . The former are obtained by applying a suitable model function such as the Ornstein-Zernike function [57], whereas the latter is commonly analyzed with either an Ornstein-Zernike-like function (see e.g., ref. [22]) or a power law [58], both of which yield qualitative information. Given a suitable polymer-solvent contrast, SLS can be used to extend the SANS measurements to shorter  $q$  values for quantitative information on the length scales of frozen inhomogeneities [56].

Other methods and approaches used in the literature include imaging techniques such

as SEM, TEM or AFM for characterizing, e.g., the surface of the material [59–62] or measurements of probe diffusion using, e.g., FRAP [63–65] or PFG-NMR [66–68] which can yield information on the length scale dominating the diffusion process.

## Aim and outline

Despite at least five decades of synthetic approaches and structural characterization of polymer gels, many open questions remain. From the structural perspective, one of the least investigated aspects is the quantity and role of cyclic chain-level defects that are found even in model star polymer networks (SPNs) including the famous tPEG network of Sakai [23]. Although the pioneering work of Lange et al. [23] established a low-field solid-state NMR methodology for characterizing the most predominant cyclic defect (the *double link* - DL) in the latter type of network, only few studies were performed to establish relationships between the preparation conditions and the emerging distribution of connectivity motifs (see e.g., refs [24, 25, 48, 52, 69]) - none of which included MQ NMR and only Johnson et al. tackled this problem experimentally [24, 52, 69]. This work aims to go beyond the current-state of research by addressing open questions in the methodological procedure of Lange et al. by quantifying both measurement and analysis errors in the procedure and increasing the overall repeatability of the analysis. Furthermore, it adds empirical value by applying the given method to different SPNs, covering both transiently end-linked tPEG networks (published in [30, 55] and permanently-linked networks (published in [47, 70, 71]).

A better empirical understanding of the relationship of cyclic defects and the distribution of connectivity motifs is provided by investigating the amphiphilic tPEG-tPCL and a complementary tPEG-tPEG network in good solvents with respect to variations in key synthesis parameters (concentration  $c_{\text{prep}}$ , temperature  $T$ , solvent). Detailed MQ NMR reveals that the heterocomplementary oxazinone-based synthesis is capable of producing gels nearly free of elastically inactive defects. However, across all variations, the network showed a dominating DL fraction that was significantly higher in comparison to that of the Sakai gel, thus revealing that the DL fraction can depend on not yet understood influences of the synthesis. A homocomplementary end-linked tPEG-SH system was investigated with a variation on  $c_{\text{prep}}$  up to several times the overlap concentration  $c^*$ , which yielded the surprising result that even a homocomplementary reaction is able to produce networks reaching primary defect fractions and connectivity motif distributions comparable to the Sakai network. Although the synthesis itself is barely used in current research, the result challenges the need for a heterocomplementary reaction at least for  $c_{\text{prep}} \gg c^*$ .

For the transiently-linked networks one of the main motivations arises from the potential self-repair of network defects as mentioned before. While this behavior has already been studied in literature in terms of e.g., rheological modulus, a discussion on the connectivity motif distribution is yet missing. In this work, the latter aspect is discussed phenomenologically by studying different transient networks. A defect-rich tPEG-linPEG (A<sub>4</sub>-A<sub>2</sub>) metallo-supramolecular dual network with an additional ion-mediated terpyridine binding site (therefore a mixture of permanent and transient links) is studied with and without ions [55]. While the overall connectivity motif distribution is not impacted by the addi-

tional transient links, it could be shown that networks could be successfully reinforced to the expense of the addition of ion-mediated chain clusters. A later chapter on an A<sub>4</sub>-A<sub>4</sub> tPEG network utilizing a similar chemistry in combination with a variety of ions and an alternative (more sterically demanding) phenantroline end group focuses on the question of the feasibility of utilizing the concept of steric hindrance of different supramolecular coordination complexes as a tool for regulating the degree of self-repair. Again, MQ NMR was able to quantify chain-level connectivity motif distributions and provide successful insights into this synthesis strategy.

Finally, the microstructure of the amphiphilic tPEG-tPCL network is studied on the nm-scale using a mixture of SAXS, MAS DQ NMR (an extension of the aforementioned MQ NMR method with chemical resolution under magic-angle spinning) and pulsed-field gradient (PFG) NMR for information on the diffusion of polysaccharide (PSC) and polystyrene (PS) probes within the network. The aim of this venture is a characterization of the network morphology in a non-selective and selective solvent to characterize the changes occurring upon microphase separation (MPS) allowing for a better understanding of the interplay of MPS and network constraints by crosslinked chains. Intuitively, it can be assumed that the crosslinks pose a constraint on the rearrangement induced by the solvent change. Using SAXS, these length scales (cluster distance and size) were estimated and compared with a bond-fluctuation model (BFM) simulation prediction provided by collaborators, revealing a quantitative match. Additionally, it allowed for a critical test of the validity of the Teubner-Strey model (originally used only for liquid micro-emulsions [72]) for the case of MPS of an ACPN. The use of MAS DQ NMR allowed for a prediction of the orientation of the PEG chains after MPS, revealing a strong orientation effect along the cluster surface.

Open questions concerning the diffusivity of probes are addressed using PFG-NMR. While the current literature addresses predictions mainly for colloidal probes (see e.g. a recent review of Amsden [73] using ideas of a well-defined "mesh size", this work refrains from these models as non-colloidal probes are used. Instead, it follows up a model motivated by polymer chain diffusion in the semi-dilute regime developed by Michael Lang [74] and estimates the characteristic length scales in terms of a hydrodynamic screening length  $\xi_h$ . With that, discussions and open questions on the meaning of extracted length scales for "mesh sizes" and related discussions on the ambiguity of the term (with definitions that easily span a decade of length scales from the correlation blob size  $\xi_c$  to the geometric distance) [75, 76] are laid to rest for this particular system. By measuring  $\xi_h$  for both selective and non-selective solvent, it could be shown that MPS does not significantly affect the diffusion of probe molecules, as the surrounding PEG matrix leaves enough volume for a comparable diffusion of probe molecules.

## Chapter 2

# Polymer chains and networks

### 2.1 Polymer chains: Conformations and length scales

Many properties of polymer networks, such as the residual dipolar coupling (RDC), the corresponding correlation length scale  $\xi_c$  and length scales occurring upon microphase separation (MPS), depend on the spatial extent and orientation of the respective chains in solution. To understand the changes that occur to a chain after it is immersed in a solvent at finite concentrations, the relevant single-chain equilibrium length scales will be discussed first for establishing a foundational understanding.

The most simple description of the length scale occupied by a polymer chain can be made using the approximation of freely jointed straight rods of length  $l_c$  equal to the sum of the absolute values  $b$  of the individual bond vectors  $\vec{b}_i$ . This results in a quantity called the *contour length* and serves as the absolute maximum length a polymer chain can realize.

$$L_c = \sum_{i=1}^N |\vec{b}_i| = bN \quad (2.1)$$

However, it is clear that the contour length alone is a non-descriptive measure for the effective size of a chain given the intricate spatial arrangements and conformations that polymer chains may adopt, neglecting e.g., chain flexibility, self-avoidance and topological constraints. Due to the typically high number of monomers that constitute a polymer, stochastic quantities and distributions of length scales are typically used. The most simple model relying on a stochastic description is the *freely jointed chain model*, which assumes a random walk of conformations along the chain without further restrictions due to, e.g., steric hindrance. It results in a 3D-Gaussian distribution of end-to-end vectors as follows:

$$P_N(\vec{r}) = \left( \frac{3}{2\pi b^2 N} \right)^{3/2} \exp\left( -\frac{3\vec{r}^2}{2b^2 N} \right) \quad (2.2)$$

From this, the  $n$ -th statistical moment  $\langle \vec{r}^n \rangle$  can be easily obtained and used as a descriptor for the length scales. The square root of the second moment, being the mean squared end-to-end distance  $R_{ee}$ , is typically used, which is a non-vanishing quantity by definition. Compared to contour length, the scaling exponent of  $N$  is significantly smaller ( $\nu = 0.5$



instead of  $\nu = 1$ ), indicating much smaller distances and coil-like structures.

$$R_{ee} = \sqrt{\langle \bar{r}^2 \rangle} = bN^{1/2} \quad (2.3)$$

While this model accurately predicts a few cases where polymers have nearly ideal chain structures, it fails as a basis to accurately predict many polymer properties due to the fact, that conformational correlations of neighbouring monomers are ignored (mathematically, it is assumed that the ensemble average over the bond angle  $\theta_{ij}$  converges towards zero), which is not borne out by reality on a single-monomer level. However, instead it converges towards a finite value  $C_1$ , whose sum over all monomers  $C_n$  is referred to as *Flory's characteristic ratio* which typically is found to be on the order of 4...10 (see ref. [5] and references therein) with a finite limit value  $C_\infty$  for long chains ( $n \gg 100$ ). With that, we can approximate  $R_{ee}$  as follows:

$$R_{ee} = C_\infty^{1/2} \cdot bN^{1/2} \quad (2.4)$$

The exact values of  $C_\infty$ , as well as the values of  $N$  at which the limit value is reached, depend on the stiffness of the chains, which is translated into the correlation of the bond angle between neighboring monomers.

$$C_\infty = \frac{\langle \bar{r}^2 \rangle}{Nb^2} = \frac{l_k}{b} \quad (2.5)$$

A useful model is the projection of a real chain onto an equivalent freely-jointed chain that has the same  $R_{ee}$  and scaling law as described in eq. 2.3. with an effective number of freely-jointed monomers  $N_k$  and bond length  $l_k$  which are called *Kuhn monomers* and *Kuhn length* respectively.

$$\sqrt{\langle \bar{r}^2 \rangle} = l_k N_k^{1/2} = C_\infty^{1/2} \cdot bN^{1/2} \quad (2.6)$$

Similarly to  $C_\infty$ , the properties of the Kuhn chain ( $N_k, l_k$ ) depend on the number of monomers  $N$  needed to realize a complete conformational decoupling ( $\langle \cos \theta_{ij} \rangle_k = 0$ ) of the resulting Kuhn monomers  $N_k$ .

There are numerous more models available to accurately describe the end-to-end distance of polymer chains. These models cater to general cases as well as specific scenarios such as stiff chains, while often incorporate assumptions about bond angle (referred to as the "Freely rotating chain model") or torsion angle (known as the "hindered rotation model"), or even employ alternative theoretical approaches (like the "Worm-like chain model"). However, for the purpose of this work, none of these models is necessary, and thus are not discussed here.

As a last note concerning the actual end-to-end distance of a polymer chain, it should be noted that in all models presented, the possibility of the chain crossing itself was not considered. While this is not necessary for very short chains, it becomes increasingly probable with an increasing number of monomers. It was found by Flory and Fischer [77, 78], as well as subsequent numerical calculations [79], that the implementation of an *excluded volume* changes the exponent of eq. 2.3 qualitatively. The Flory-Fischer argument

predicts a scaling of  $R_{ee} \sim N^{0.6}$ , while numerical calculations of this behavior (commonly referred to as a *self-avoiding walk* - SAW) predict a scaling law of  $R_{ee} \sim N^{0.588}$ .

Although the provided end-to-end distances will be useful in the following chapters on microphase separation, additional limitations arise from the specific types of monomers (with more than two chain ends) used in this work. In this case, the end-to-end distance is not defined and the approximation of chains with functionality numbers  $f > 2$  by linear chains ( $f = 2$ ) is not accurate. Thus, the radius of gyration  $R_G$  can be used as another measure to describe the size of a polymer chain yielding good approximations for higher functionalities as long as the respective arms are of similar size (which is equivalent to the assumption of a globular macromer). Then, the average distance of each monomer to the center of mass ( $\vec{r}_c$ ) of the chain is defined as follows:

$$R_G^2 = \frac{1}{N} \sum_{i=1}^n (\vec{r}_i - \vec{r}_c)^2 \quad (2.7)$$

For a linear polymer chain with  $N_k$  Kuhn monomers of length  $b_k$

$$\langle R_G^2 \rangle = \frac{1}{6} N_k b_k^2 \quad (2.8)$$

is found. For the special case of  $f$ -arm star-shaped polymers (and the common case of  $f = 4$ ), this equation is reduced to the following form [5]:

$$\langle R_G^2 \rangle = \left[ \frac{N_k b_k^2}{6f} \right] \left( 3 - \frac{2}{f} \right) \stackrel{f=4}{\approx} \frac{1}{10} N_k b_k^2 \quad (2.9)$$

Hence it is shown that the radius of gyration of a 4-arm star polymer chain can be approximated by a linear chain with 3/5th of the number of Kuhn monomers, which is higher than the intuitive estimate of 1/2 obtained by considering that the diameter of a star equals the length of two arms.

Using the Gaussian distribution function of the end-to-end distance of a polymer chain presented in eq. 2.2, one can immediately derive a "0th order" approximation of the response of a polymer chain upon external deformation as follows: With prior knowledge of the distribution function, the entropy of the chain can be described by resorting to its definition as  $S = k_B \ln \Omega$ , where  $\Omega$  is the probability distribution of all states the system can realize (and therefore conveniently equals eq. 2.2).

$$S(N, \vec{r}) = k_B \ln P_N(\vec{r}) = -\frac{3}{2} \frac{k_B \vec{r}^2}{b^2 N} + S(N, 0) \quad (2.10)$$

Therefore, the Helmholtz free energy  $F = U - TS \approx -TS$  and the (microscopic) retractive force  $f_{el} = -\partial F / \partial r$  arising from an external deformation of size  $\Delta r$  can be written as:

$$f_{el} = - \left( \frac{\partial(U - TS)}{\partial r} \right)_{r=\Delta r} = -\frac{3}{2} \frac{k_B T}{b^2 N} \Delta r \quad (2.11)$$

Here,  $U = 0$  was used, since it is usually assumed that the chain is treated as a free chain at thermodynamic equilibrium without additional internal interactions. The result of this treatment is a micro state-reducing retractive force of entropic origin (*entropic elasticity*),

that expresses the urge of the system to maximize the number of accessible micro states. Although this treatment is valid only for small deformations (it is easily seen that this expression does not include any arguments of finite extensibility), it will be sufficient for the following sections and used to explain the behavior of a single polymer chain in solution.

## 2.2 Thermodynamic properties of polymers in solution

So far, polymer chains have been discussed only in the context of a set of coexisting, but not interacting, single chains, which while a useful concept, is unrealistic for practical considerations. An extension of the concept of isolated chains to polymer solutions and subsequently polymer networks needs consideration of several effects. A first extension to a single chain immersed in a solvent will describe the interaction of a chain and solvent molecules and the resulting impact on its conformation. In the second step, the impact of a finite polymer concentration (or volume fraction) will be discussed.

For describing concentration-dependent effects in polymer solutions, it is intuitive to move away from absolute concentration measures and consider relative descriptions such as the overall polymer volume fraction  $\phi$  or the internal polymer volume fraction  $\phi_i$  within the pervaded volume of a single chain. Choosing again a single chain as a starting point, one can estimate  $\phi_i$  by comparing the volume of  $N$  monomers with a respective size of  $b$  with the chain volume (described by the sphere spanned by the end-to-end distance  $R_{ee} = bN^\nu$ ).

$$\phi_i \approx \frac{b^3 N}{(bN^\nu)^3} = N^{1-3\nu} \quad (2.12)$$

Thus, it is easily seen (e.g.,  $N = 50$  and  $\nu = 3/5 \iff \phi_i \approx 0.04$ ) that an isolated chain in solution is internally highly diluted.

### 2.2.1 Polymer chains in solution

A possible description of the thermodynamic behavior of polymer chains in solution is provided by the Flory-Huggins lattice theory, where the constituents of a binary mixture (being either two polymers or a polymer and a solvent) are placed on a lattice under the assumption of an average interaction potential that is constant across the lattice (mean-field theory), since the occupation probability of a specific lattice site is based only on average compositions (neglecting spatial correlations arising from chain connectivities). The Gibbs free energy of mixing is considered as the sum of an enthalpic and entropic component, for which expressions will be derived.

$$\Delta G_{\text{mix}} = \Delta H_{\text{mix}} - T\Delta S_{\text{mix}} \quad (2.13)$$

The entropic component can be derived by counting the possible states of each molecule in the lattice and deriving the entropy according to its thermodynamic definition using  $S = k_B \ln \Omega$ . This results in the following equation that describes the entropy per lattice site, where  $R$  is the gas constant,  $\phi_{1,2}$  are the respective volume fractions and  $N_{1,2}$  the

number of lattice sites occupied.

$$\Delta S_{\text{mix}} = -R \left( \frac{\phi_1}{N_1} \ln \phi_1 + \frac{(1 - \phi_1)}{N_2} \ln \phi_2 \right) \quad (2.14)$$

The enthalpic part of eq. 2.13 is obtained considering the change in enthalpy after replacing a molecule at a lattice site with a molecule of the other kind. For that, we consider the pairwise interaction energies between molecules of the same kind ( $\epsilon_{11}$ ) and between molecules of different types ( $\epsilon_{12}$  and  $\epsilon_{21}$ ). While the probability of each pairwise interaction is governed by the respective volume fractions  $\phi_{1,2}$ , the interaction parameter (also called *Flory-Huggins parameter*) itself is defined independent of the respective volume fractions as follows:

$$\chi \propto \frac{1}{T} (\epsilon_{12} - 0.5(\epsilon_{11} + \epsilon_{22})) \quad (2.15)$$

With that definition, the enthalpy of mixing is obtained in the following way:

$$\Delta H_{\text{mix}} = \chi \phi_1 (1 - \phi_1) kT \quad (2.16)$$

With that, the Gibbs free energy of mixing for a polymer in a solution ( $N_2 = 1$ ) becomes:

$$\frac{\Delta G_{\text{mix}}}{RT} = (1 - \phi_1) \ln(1 - \phi_1) + \frac{\phi_1}{N} \ln(\phi_1) + \chi \phi_p (1 - \phi_1) \quad (2.17)$$

From this, it can be easily seen that for large  $N$  one of the two entropic terms vanishes, resulting in a mixing process that is dominated by energetic contributions and most importantly, the magnitude of  $\chi$ . In most cases,  $\chi$  is positive and large ( $> 0.5$ ), owing to the preference of chains to be surrounded by a chemically similar environment and thus rendering the overall process of mixing polymers difficult. With this in mind, it should be evident that, in polymer reactions involving two different compounds, such as ACPNs, one should always consider the possibility of component demixing as part of the overall assessment of potential issues.

While the Flory-Huggins theory provides a description for the change in the Gibbs free energy arising from "dropping" a single chain in a solvent, it neglects the entropic contribution manifested in the elastic free energy of the chain as discussed previously in eq. 2.11. Flory's approach of describing the swelling of a single chain in a good solvent is based upon the assumption that the equilibrium structure is determined by the balance of these two energy contributions and reached once the change in total free energy due to swelling equals 0 [80]. Using this idea, Flory obtained several relationships for the end-to-end distance in both, good and  $\theta$  solvent (negligible influence of the solvent).

For a  $\theta$  solvent, the chain maintains its initial conformational state because of the cancellation of both energy contributions. However, for a good solvent, the chain swells until it is limited by the elastic energy, resulting in the well-known scaling of  $R_{\text{ee}} \propto N^{3/5}$ , indicating that a single polymer chain in a good solvent will always behave as if it were a real chain independent of the exact value of  $\chi$ . It should be noted, however, that this consequence of Flory's may not reflect the behavior of real systems, and thus, the latter equation is usually generalized to the more well-known equation.

$$R_{ee} \propto bN^\nu \quad (2.18)$$

with  $\nu$  taking intermediate values in between the ideal and the real chain ( $1/2 \leq \nu \leq 3/5$ ) [76]. So far, the case of a poor solvent (resulting in a collapse of the chain) was not covered and will be only briefly mentioned as  $R_{ee} \propto bN^{1/3}$ . For more information on its derivation, the reader is referred to the concept of the Mayer-f function as a way to quantify this exponent as shown in e.g., ref. [5].

## 2.2.2 Concentration-dependent conformational changes in polymer solutions

Now, the concept of a single chain in solution will be extended to higher concentrations, revealing conformational changes arising from inter-chain correlation effects. When discussing these effects, one can easily imagine that these correlations will be strongly dependent on the size (number of monomers  $N$ ) and concentration of polymer chains in solution, as well as the conformation. For this, one commonly introduces the concept of the *overlap concentration*  $c^*$  or the *overlap volume fraction*  $\phi^*$ , both of which can be used to describe the occupied volume of the chain compared to its pervading volume as follows:

$$\phi^* = \frac{v_{\text{mon}}N}{R_{ee}^3} = \frac{b^3N}{(bN^\nu)^3} = N^{1-3\nu} \quad (2.19)$$

$$c^* = \rho\phi^* \quad (2.20)$$

Here,  $\nu$  is the excluded volume exponent ( $1/2 \dots 3/5$  under the assumption of a non-selective solvent), leading to overall exponents between  $-1/2$  and  $-4/5$  for the power law. At a polymer volume fraction of  $\phi = \phi^*$ , it is assumed that the solution is filled by spheres of pervaded chain volumes, with the chains itself being on the verge of overlap. Using this property, polymer solutions are classified into dilute systems ( $\phi < \phi^*$ ), semi-dilute systems ( $\phi^* < \phi < \phi^{**}$ ), concentrated systems ( $\phi > \phi^{**}$ ) and polymer melts ( $\phi = 1$ ).

In the dilute state, a chain will not interfere with its neighbors; therefore, its size is preserved according to  $R \sim N^\nu$  with  $\nu = 1/2$  for ideal chains ( $\theta$  solvent) and  $\nu = 3/5$  for chains in good solvent. Upon removal of the solvent (= polymer melt), this changes to  $R \sim N^{1/2}$  independent of the *initial conditions*, as the chains in the melt always behave as if the chains were ideal [81]. From this, the semi-dilute and concentrated system can be extrapolated (as changes should be gradual and not step-wise), with details given below: At concentrations above  $\phi^*$ , chains will either need to shrink to avoid overlap with neighboring chains (called the *isolated model*), or alternatively favor a mixture of shrinking and chain overlap (called the *mixed model*), which in both cases leads to a reduction in the overall end-to-end distance. However, since experiments indicate that the mixed model is more plausible, only the mixed model will be briefly explained here. Although the effective chain pressure due to the crowding condition leads to chain overlap on a large scale, it is assumed that excluded volume effects will dominate the chain conformation on a small scale. Therefore, a *concentration blob*  $\xi_c$  is constructed that is roughly equivalent to the volume of the pervaded chain. It is constructed such that, at its border, the probability

of finding a monomer of the same chain and the probability of finding a monomer of a different chain are equivalent. At the overlap  $\phi = \phi^*$  it is assumed to be equivalent to an ideal chain (see eq. 2.3). Additionally, it is assumed that it does not depend on the molecular weight of the polymer, since the blob itself (and therefore the whole system) can simply be rescaled without changing the relative length scales. With these assumptions, a scaling law is created in the following way:

$$\xi_c = R_F \left( \frac{\phi}{\phi^*} \right)^z \quad (2.21)$$

Eq. 2.21 is used to fulfill the assumption that at  $\phi = \phi^*$  the concentration blob is equivalent to the Flory radius, while it will shrink at higher concentrations. Using this equation in conjunction with eq. 2.19, we arrive at the following:

$$\xi_c = bN^{3/5} \left( \frac{\phi}{N^{-4/5}} \right)^z \sim N^{(3+4z)/5} \quad (2.22)$$

Using the obvious assumption stating that  $\xi \sim N^0$  (since it depends only on  $\phi$ ), the exponent can be calculated to  $z = -3/4$ , resulting in a power law of the form:

$$\xi_c \sim \phi^{-3/4} \quad (2.23)$$

Upon further increase in concentration, the correlation length will decrease toward the size of the thermal blob  $\xi_T$  (which is the size at which the excluded volume effects are smaller than  $kT$  and thus negligible), whose size itself is independent of the concentration. Using the result of the semi-dilute solution (eq. 2.22), we arrive (calculation not shown here) at the following simple expression for the threshold volume concentration  $\phi^{**}$  of the concentrated regime:

$$\phi^{**} \approx \frac{v}{b^3} \quad (2.24)$$

As the correlation blob size in the concentrated regime is crossing the thermal blob size, at which the chain behaves like an ideal chain with  $R = bN^{1/2}$ , it automatically follows that the entire chain will behave as if it were an ideal chain.

For a  $\theta$ -solvent, the exponent in  $N^\nu$  and  $N^{1-3\nu}$  of eq. 2.22 changes from  $3/5$  to  $1/2$ , thus resulting in a scaling of  $\xi_c$  in the semi-dilute regime of  $\xi_c \propto \phi^{-1}$ .

### 2.2.3 Diffusion of chains in solutions

The diffusion of a polymer chain within a solution of chains is one of the fundamental physical processes occurring in polymer solutions. Its conceptual treatment can take many forms, such as the treatment as a colloidal particle or a chain "reptating" along its own curvature through a dense and crowded solution of chains. This section will start by recalling the well-known diffusion principles of a simple hard-sphere probe, and extend this idea to more complex polymer chains.

As investigated by the pioneering work of Einstein and Smoluchowski [82, 83], the three-dimensional mean-square displacement of a free colloidal particle due to Brownian motion

has a linear dependence on the observation time and is connected via a proportionality called the diffusion coefficient  $D$ :

$$\langle (\vec{r}(t) - \vec{r}_0(t))^2 \rangle = 6Dt \quad (2.25)$$

Therefore, we find the average distance as the square root of the latter equation with a scaling of  $t^{1/2}$ .

The motion of this hard-sphere probe is considered to be influenced by friction, thus raising the need for a model of the frictional force  $\vec{f}$ , which will depend on the velocity of the molecule in question, as well as a size- and shape-dependent parameter  $\zeta$ , called the friction coefficient. With that, the diffusion coefficient can be expressed in dependence of the friction coefficient, leading to the Einstein relation  $D = kT\zeta^{-1}$ . For the case of a hard-sphere probe and a Newtonian liquid of a given viscosity  $\eta$ , the Stokes-Einstein equation is obtained using the Stokes law substituting  $\zeta$  by a suitable hydrodynamic radius  $R_h$  of the probe and the solution viscosity  $\eta$ .

$$D = \frac{kT}{6\pi\eta R_h} \quad (2.26)$$

For polymeric materials, which are not necessarily represented by the simple hard-sphere model, both the Rouse model or the Zimm model can be considered as possibly suitable approximations of the overall chain diffusion coefficient. The Rouse model considers a mapping of the polymer chain onto a construct of spherical beads that are interconnected by springs. Between the beads, there is no hydrodynamic interaction, which results in a friction coefficient  $\zeta$  that is independent of position and the same for each bead, which in turn results in a simple additive chain friction coefficient  $\zeta_c = N\zeta$ . Thereby, it is assumed that solvent molecules will drain freely through the chain ('free-draining limit'). Using the Einstein relation above, we can formulate an alternative equation similar to eq. 2.26 for a Rouse chain:

$$D = \frac{kT}{N\zeta} \quad (2.27)$$

As the relationship of the end-to-end distance  $R_{ee}$  (which instinctively can be assumed as a crude alternative measure to  $R_h$ ) is nonlinear to the number of monomers  $N - 1$  (see eq. 2.18), one immediately finds a distinct difference in eq. 2.26 and eq. 2.27 (as  $\nu < 1$ ).

However, the modeling of polymer diffusion using the Rouse model does not always reflect experimental observations, because of the violation of the "free-draining solvent" condition. Movement of the beads on the chain may drag surrounding solvent, resulting in an effective hydrodynamic interaction between the beads. This drag effect will result in modified hydrodynamic friction and is referred to as the "non-draining" limit. Therefore, Zimm provided a modification of the Rouse model (details in [84]) and is known as the Zimm model. Because of the drag effect on the solvent molecules, the pervaded chain volume is assumed to be a solid ("sphere-like") object with a size approximated by the overall coil size according to eq. 2.18. With the chain now being treated as a solid object, the Stokes-Einstein equation is now valid with the radius of the sphere  $R$  being approximated

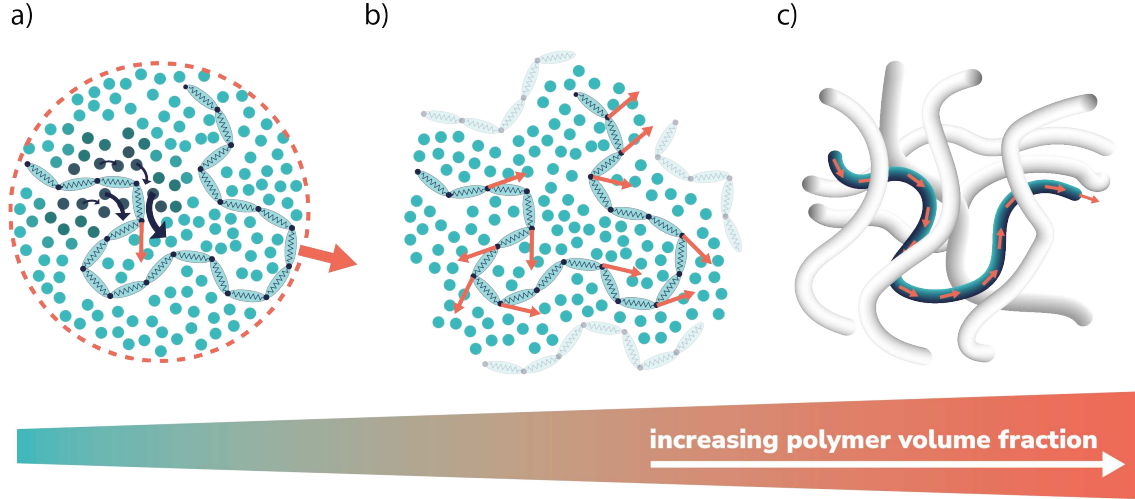


Figure 2.1: Tentative picture illustrating the diffusion models explained in this chapter. For all processes, the "random force" from the diffusive process is shown as a red arrow. a) Diffusion of a polymer chain with  $N = 20$  Kuhn segments (light blue ellipsoids) with a beads and springs representation according to the Rouse model. Random forces act on each subchain, ignoring the surrounding solvent molecules (spheres). b) The diffusive process of each subsegment induces a viscous drag effect on the solvent molecules that are close (dark blue arrows), leading to an effective diffusion of the chain + solvent as a solid sphere. c) Reptation motion of a chain along its primitive tube (blue) in a strongly-confined matrix of other chains (grey tubes).

by the chain size (up to a constant factor), resulting in the following variation of the Stokes-Einstein relation:

$$D = \frac{kT}{\eta b N^\nu} \propto M_w^{-\nu} \quad (2.28)$$

As shown by Michael Lang in ref. [74], this transition can be described by considering that in a semi-dilute solution, the hydrodynamic screening length  $\xi_h$  can be approximated by the static correlation length  $\xi_c$  of the solution (or e.g., network) [85].

$$\xi_h \approx \xi_c \approx b \left( \frac{b^3}{v} \right)^{(2\nu-1)/(3\nu-1)} \phi^{-\nu/(3\nu-1)}.$$

Here,  $\phi$  is the polymer volume fraction of the surrounding matrix and  $b$  denotes the root-mean-square end-to-end distance of a Kuhn monomer. Following steps outlined in ref. [74], the ratio of the diffusion coefficient  $D_0$  of a chain of size  $R_h$  in a dilute solution vs. the diffusion coefficient  $D$  in the crossover regime where  $\xi_h < R_h$  (but  $R_h$  still not comparable to the tube diameter) can be described by the following relation:

$$\begin{aligned} \frac{D}{D_0} &\approx \frac{g b N^\nu}{\xi N} \\ &\approx \left( \frac{b^3}{v} \right)^{\frac{2(2\nu-1)}{3\nu-1}} \left( \frac{\phi}{\phi^*} \right)^{-\frac{1-\nu}{3\nu-1}} N^{-(1-\nu)}. \end{aligned} \quad (2.29)$$

If the diffusing chain experiences additional spatial constraints due, e.g., to pores or a comparably dense mesh of a polymeric matrix, the resulting power law  $D \sim N^{-\nu}$  will



qualitatively change to the reptation regime with  $D \sim N^{-2}$  as shown by de Gennes [86], where diffusion can only occur along the primitive path ('tube') of the polymer chain.

## 2.3 Star polymer networks

In the preceding sections, we primarily examined the physical properties of polymers in terms of their individual chain structure and the interactions between chains in a solution at finite concentrations. However, it is crucial to note that the majority of polymer applications center around their mechanical properties, which are typically created through a process called crosslinking. By formation of chemical or physical bonds between the chains, a macroscopic elasticity can be achieved due to the spatial fixation of the chains' ends. Given a diversity of crosslinking methods paired with a wide selection of monomer architectures (e.g., linear precursors, star precursors or block star precursors) and different synthesis strategies (e.g., bulk and solution synthesis or homo - and heterocomplementary end-linking reactions), a plethora of different gel morphologies can be realized (see e.g., refs. [3, 4] for comprehensive reviews). Here, two important aspects of these diverse systems are shortly presented: their mechanical behavior, as well as deviations from the desired behavior due to network defects arising on a chain-level or nm-scale. As this work has a strong focus on star precursors (precursors with  $f > 2$  - but typically  $f = 4$  - end-linking sites), the latter aspect of network defects will only be discussed in this context.

### 2.3.1 Network elasticity

Generally, mechanical properties of gels (or elastomers in general) can be characterized in terms of e.g., (engineering-) stress  $\sigma_{\text{eng}}$  - elongation ratio  $\lambda$  curves, that characterize the uniaxial stretching process of a chain. Both are defined as follows:

$$\sigma = \frac{F}{A_0}$$

$$\lambda = \frac{L}{L_0}$$

Here,  $F$  is the applied force applied on the given material area  $A_0$ , and  $L_0, L$  are the respective lengths pre- and after stretching. Often, an alternative formulation is used based on the strain  $\epsilon = (L - L_0)/L_0$ . As shown in section 2.1, the ratio of the unperturbed end-to-end distance  $R_{ee}$  and the contour length (being the equivalent of a fully stretched chain) scales with  $\propto N^{1-\nu}$ , explaining experimentally observed stretching ratios of the order of 10 in terms of conformational rearrangements and rubber elasticity (see eq. 2.11). Using the definition of engineering stress above, we can define a criterion for a polymer solution to be treated as a polymer gel (or in a more general sense: *polymer network*) using an empirical observation. By measuring the time-dependent stress relaxation of the compound upon exertion of a certain stress, a fundamental difference between liquids (polymer solutions) and solids (polymer networks) is found. Viscoelastic behavior in solutions (and also polymer melts) is only observed for short time scales, resulting in an overall flow of the sample at long times and  $\sigma(t = \infty) = 0$ . Once a significant amount of crosslinks has

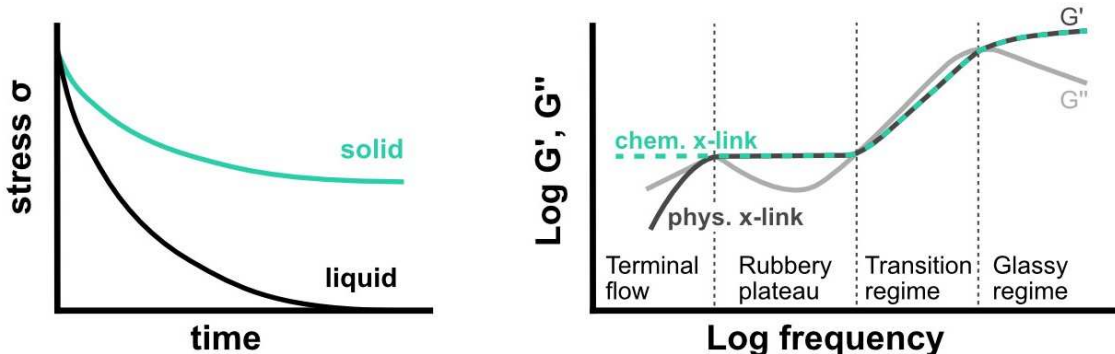


Figure 2.2: Left panel: Visualization of the differences of engineering stress  $\sigma$  over time for a liquid (e.g., polymer solution) or solid (e.g., network). Right panel: Qualitative plot of an oscillatory shear experiment for a permanent crosslink (e.g., a chemical network) or a dynamic crosslink (e.g., a physical network with transient bonds). Regimes other than the rubbery plateau are only shown for the sake of completeness, but not mentioned in the text. For the chemical (permanent) crosslink, no terminal flow is observed, whereas the physical (transient) crosslink displays a finite plateau width with an adjacent terminal flow regime. For more information, the reader is referred to e.g., ref. [5].

been reached (called the gel point), the overall behavior switches from a viscoelastic liquid towards a viscoelastic solid with  $\sigma(t = \infty) > 0$  (see Figure 2.2).

In many experiments, the mechanical properties of the emerging network are characterized by the shear modulus  $G$ , being the linking factor between stress and deformation. The storage ( $G'$ ) and loss modulus ( $G''$ ) of a sample are commonly measured under the influence of an oscillating strain of frequency  $\omega$  [87]. Crosslinked samples will experience a plateau with a weak or no dependence of  $G'$  on  $\omega$  (the so-called rubber regime or rubbery plateau), while a viscoelastic liquid will show a terminal flow regime with  $G'(\omega) \propto \omega^2$  (see Figure 2.2). The height of the plateau is determined by the crosslink density (see next paragraph for two simple models), whereas the width of the plateau is characterized by the type of crosslinking and the glass transition temperature. The high-frequency limit of the plateau (equivalent to unchanging frequency but lowered temperature by application of time-temperature superposition [5]) is dominated by the transition to the glassy state, whereas the low frequency (or high temperature) limit is either non-existent (permanent chemical crosslink) or dominated by the bond lifetime (transient/physical crosslink). As will be discussed in section 3.3, a well-defined plateau value of the shear modulus  $G'$  (translated to an unchanging bond order parameter  $S_b$  of the crosslink) is needed for successful application of the MQ NMR analysis used in this work (see section 3.3).

### Modulus prediction

One of the most simple yet applicable models of predicting the shear modulus (among other mechanical properties) of a polymer network is the affine network model. The model is based on assumption that network junctions are fixed in space, thus resulting in the idea of macroscopic network deformation carrying over to the microscopic chain deformation. Thus, a deformation of an arbitrary factor  $\lambda$  will result in a deformation of the end-to-end

distance of each chain by the same  $\lambda$ . With derivations expanding on the idea of entropic rubber elasticity of eq. 2.11 as shown in e.g., ref. [5], the shear modulus is predicted to be

$$G_{\text{aff}} = \frac{\rho RT}{M_c} \quad (2.30)$$

where  $\rho$  is the material's density,  $R$  is the gas constant,  $T$  is the temperature and  $M_c$  is the molecular weight of a crosslink (or network strand).

While the affine model yields satisfactory predictions for the case of ideal bulk networks, it fails to predict networks of higher dilutions (= gels) and those with a significant number of inelastic material (see section 2.3.2 for more information) or topological peculiarities such as entanglements. For the latter example, the reason is, that the assumption of static network junctions is easily violated once their surroundings are not fully integrated into the network. For this case, the phantom model can be applied, correcting the affine model by incorporating the possibility of crosslink fluctuations. It considers that the ends of the strands can move, subject to the given hierarchy of network connectivities (instead of being completely fixed in space), thus allowing for fluctuations. With derivations, again, given in e.g., ref. [5], the phantom model modulus can be given in terms of the affine modulus given before:

$$G_{\text{ph}} = \left(1 - \frac{2}{f}\right) G_{\text{aff}} = \left(1 - \frac{2}{f}\right) \frac{\rho RT}{M_c} \quad (2.31)$$

Here,  $G_{\text{aff}}$  is the affine modulus prediction according to eq. 2.30 and  $f$  is the functionality (number of active crosslinks per strand) of the network. Given that spatial fluctuations of the junctions are allowed, it results in a modulus significantly lower than the affine modulus (a factor of e.g., 0.5 for tetra-functional networks with  $f = 4$ ).

### Equilibrium swelling of networks

Given the entropic chain elasticity discussed before (see eq. 2.10), it is clear that - even for a good solvent - swelling until chains are fully stretched is not expected. The equilibrium degree of swelling can be determined using the Flory-Rehner relation [9], which arises from minimizing the total free energy  $F = \Delta F_{\text{mix}} + \Delta F_{\text{el}}$  (see eq. 2.11 and eq. 2.13) that is assumed to be a superposition of contributions from the mixing free energy  $\Delta F_{\text{mix}}$  and the entropic elastic contribution  $\Delta F_{\text{el}}$ . Under the further assumption of an isotropic and affine swelling process, it follows:

$$\ln(1 - \phi_2) + \phi_2 + \chi\phi_2^2 + \frac{\rho\nu_1}{M_c} \left( \phi_2^{1/3} + \frac{\phi_2}{2} \right) = 0 \quad (2.32)$$

Here,  $\phi_2$  is the polymer volume fraction (associated to the equilibrium degree of swelling as  $\phi_2 = Q_{\text{eq}}^{-1}$ ),  $\chi$  is the Flory-Huggins parameter between polymer and solvent,  $\rho$  is the bulk polymer density,  $\nu_1$  is the molar volume of the solvent and  $M_c$  is the molecular weight of the crosslink.

It should be noted that the above relation only suits as an estimate, as it comes with several limitations, including that it requires the network to be prepared under solvent-

free conditions, assumes affine stretching of the chains and requires a Gaussian distribution of end-to-end distances. For all these limitations, numerous corrections have been provided that will not be discussed in more detail [5, 88]. The key conclusion for this work is that the equilibrium degree of swelling is strongly influenced by the molecular weight of the crosslink and the solvent quality, thus e.g., providing a qualitative argument for the low  $Q_{\text{eq}}$  observed in ACPN swollen in selective solvent.

### 2.3.2 Defects in star polymer networks

Before discussing the different types of network defects that can be found in star polymer networks (SPN), a definition of ideal SPNs will be given, such that defects can be defined as deviations from the ideal structure. The swollen (equilibrium) structure arising from crosslinking star-shaped precursors of a given functionality  $f$  should yield a homogeneous network, where every precursor is crosslinked to exactly  $f$  different neighboring precursors. Network homogeneity can be defined by quantifying the end-to-end distance of the strands between two crosslinking points and its distribution. In an ideal network, this distribution will have a vanishing width.

#### Chain-level connectivity defects

A deviation from this ideal structure can arise on local chain-level scales ( $l \approx 1 - 10$  nm, see Figure 2.3) and on a mesoscopic length scale much larger than the size of a single precursor star ( $l \approx 10 - 100$  nm). The most simple defect is a dangling chain end, which is an unlinked precursor arm, arising from either a non-functionalized arm, a non-stoichiometric ratio of precursors or (in usually small amounts [48]) from remaining end groups once the synthesis is terminated after a certain time. Its occurrence results in a reduction of the storage modulus of the resulting network, as it provides a structure with reduced elastic effectiveness. Another large class of defects only found in SPNs is cyclic defects (see Figure 2.3), whose classification derives from graph theory that considers the crosslinked chains as abstract edges and the crosslink points as vertices. With that, each connectivity motif (aside from unlinked precursors or dangling chain ends) is assigned a cycle rank  $\zeta$  that is equal to the minimum number of paths needed to start from and reach the same vertex without crossing any path twice [89]. For example, a connection of two arms of a single star (commonly called primary loop) can be classified as a cyclic defect of order  $\zeta = 1$ . If two stars are connected by two of their arms each (commonly called "double link", see Figure 2.3), its order will be  $\zeta = 2$ . Furthermore, junctions can be classified as active (= contributing to the phantom modulus) if at least three edges point towards the network [90]. If a junction would only consist of two edges, it would merely be an extension between two vertices. Although not shown in Figure 2.3, it can easily be imagined by considering two adjacent 4-arm stars and taking away two arms from one of these two stars, transforming it into a linear extension between two stars, both of which are now connected by a single chain of twice the molecular weight.

Quantification of the fraction and cycle rank of these defects (using e.g., network disassembly spectroscopy [24, 52], MQ NMR as shown in section 3.4.2 or BFM simulations

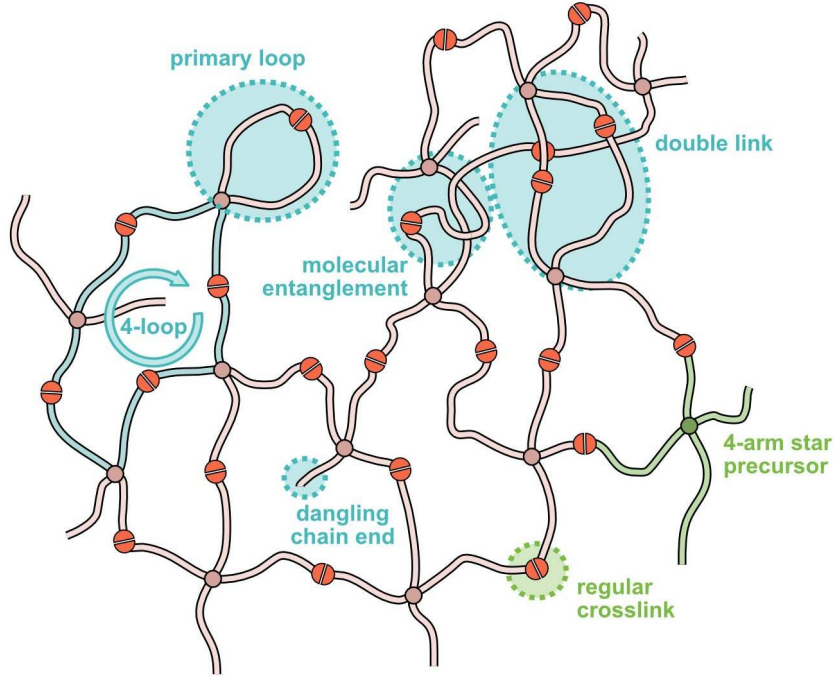


Figure 2.3: Tentative sketch of a polymer network made of homocomplementary 4-arm star precursors (see green star). The picture visualizes different kinds of connectivity defects, such as unreacted arms ('dangling chain end'), stars being connected by two instead of one arm ('double link'), entangled arms and intra-star connectivities ('primary loop'). Additionally, a more complex cyclic defect, namely a 4-loop, is shown. Three-dimensional structure and tetrahedral bond angles are neglected for simplicity.

[48]) allows for a prediction of the overall phantom modulus using e.g., RENT (real elastic network theory) [24] or simulations [25]. Both of these (and respective consecutive works) show that not only primary loops, but also elastically active higher-order cyclic defects, such as the double link, reduce the phantom modulus [24, 25]. Naturally, the impact of the fraction of elastically inactive structures is significantly higher, resulting in significant reduction of the resulting plateau modulus due to its tendency to also destabilize its surroundings. For the two other predominant connectivity defects found in SPNs with  $f = 4$  [23], being the double link (DL,  $\zeta = 2$ ) and a set of connectivity defects with  $\zeta = 3$  (referred to as higher-order connectivity defects, HOC), RENT predicts respective values of elastic effectiveness  $\epsilon$  of  $\epsilon_2 \approx 0.35$  and  $\epsilon_3 \approx 0.9$ . For all connectivity motifs with  $\zeta > 3$ , no significant reduction in elastic effectiveness is predicted for tetra-star precursors, thus rendering their mechanical properties close to those predicted for the ideal structure.

A major aim of research on swollen polymer networks is the reduction of these defects and establishing synthesis conditions that serve this aim. A popular way of suppressing a significant part of cyclic defects (more specifically, all odd-numbered defects with  $\zeta = 2n + 1$ ) is the usage of a heterocomplementary reaction (or A-B type reaction), as shown by the pioneering work of Sakai et al. [21, 91]. This type of reaction uses two types of  $f$ -functional star precursors ( $f = 4$  in the aforementioned work) which cannot react with their own type of precursor (hence "A-B type" reaction). Thus, one of the most prevalent types of defects, the loop with  $\zeta = 1$  where two arms of the same precursors are

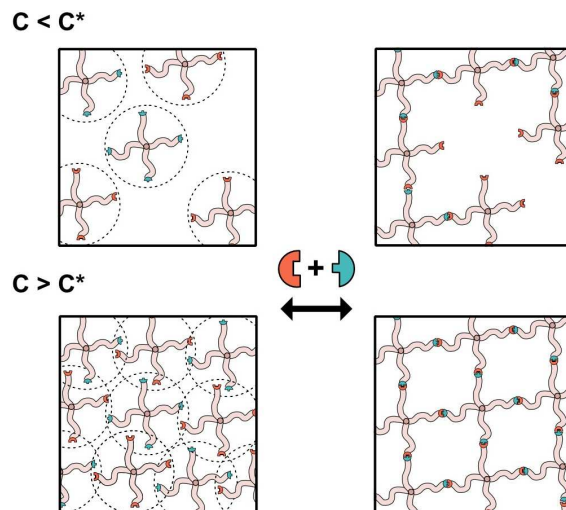


Figure 2.4: Visualization of concentration-dependent large-scale network defects (‘frozen fluctuations’) on a polymer network based on 4-arm star precursors. The top panel visualizes the situation for  $c < c^*$ , where inhomogeneities are produced due to the non-existing overlap in pervaded volume (dotted circles) of the stars. This feature is not found in the bottom panel ( $c > c^*$ ). The shown concept is strictly based on the assumption of a heterocomplementary end-linking reaction.

linked, is completely prevented by chemical means. When this type of reaction is combined with carefully chosen reaction conditions that ensure proper mixing of precursors and slow reaction kinetics (shifting the overall process to reaction-controlled kinetics [92]), even most of the unlinked chain ends ( $\zeta = 0$ ) can be prevented, resulting in a network with the predominant defect being the double link connection with  $\zeta = 2$  [23], which - unlike the other defects mentioned above - is an elastically active connectivity motif. Thus, more mechanically stable network properties can be achieved.

Another well-known factor influencing the amount of chain-level defects is the preparation concentration. At concentrations higher than the overlap concentration  $c^*$ , the overall volume is homogeneously filled with star precursors (per definition, see section 2.2.2), thus reducing the chance of built-in spatial heterogeneities that originate from heterogeneities already present in the precursor solution (see Figure 2.4). Therefore, many model networks aim for concentrations around or above the overlap concentration to significantly reduce defective connectivity motifs [23, 52, 93]. As will be shown in section 6.3, a significant increase in preparation concentration can even overcome the disadvantages of a homocomplementary reaction, yielding gels with an overall structure that is comparable to the heterocomplementary tPEG-water system.

### Trapped entanglements

Another defect, which occurs only at higher polymer volume fractions, is trapped entanglements. At concentrations  $c > c^*$ , the star precursors may intrude the pervaded volume of their neighbors and lead to entanglements. Upon crosslinking, these interpenetrated structures can be connected to the overall network, leading to a trapped entanglement as shown in Figure 2.3. Experimental studies have shown that entanglements for the 10 kDa tPEG-

water system are negligible [94] even with each arm being above the molecular weight for entanglements ( $M_e = 2.2$  kDa for a linear PEG chain in bulk;  $c \leq 2c^*$  was studied), whereas mixtures of star precursors and linear extenders are more prone to form these structures. A reason for this behavior can be speculated to be that star precursors are less prone to interpenetration effects due to a higher monomer density within their pervaded volume as compared to their linear counterpart (see e.g., ref. [95] for empirical evidence found for the polystyrene-benzene system). Due to a trapped entanglement, an additional crosslink-like structure is introduced, hence changing both the effective crosslink density (resulting in a small-scale network inhomogeneity) while also decreasing the effective molecular weight of the crosslink.

### **Nano- to microscale inhomogeneities**

Finally, these small-scale defects introduced in the previous paragraphs may result in larger-scale inhomogeneities upon swelling (length scales are typically several times larger than the length scale of a crosslinked chain) [56] as most of these defects result in a heterogeneous distribution of crosslinks. As exemplarily shown in a combined SANS + SLS study in the tPEG-water system [22], a minimization of the chain-level inhomogeneities mentioned above can also result in a strong reduction in these nanoscale inhomogeneities. Although these inhomogeneities have a strong impact on the equilibrium degree of swelling (thus, play an important role on the properties of the swollen material), they will not be discussed further, as this work does not employ methods by which these can be detected (e.g., SANS, SLS).

## Chapter 3

# NMR methodology

The following chapter will provide a basis for the principles needed for the methods used in this thesis. While it will provide a short general introduction, its focus will be mainly on multi-quantum (MQ) NMR, as well as pulsed-field gradient (PFG) NMR. For additional information on relevant topics not discussed in this thesis, such as technical details, relaxation phenomena, and derivations of some used concepts, the reader is referred to, e.g. ref. [96–98].

### 3.1 Basic principles

The most basic principle used in Nuclear Magnetic Resonance (NMR) is the Zeeman interaction of a nucleus with a spin quantum number  $I \neq 0$ , which, in short, results in a splitting of the energy levels of a spin into  $2I + 1$  distinct levels in the presence of an external magnetic field  $B_0$ . For the nucleus most commonly used in NMR, hydrogen with  $I = 1/2$ , two different energy levels (called  $\alpha$ -state and  $\beta$ -state) with an energetic difference of

$$\Delta E = -\gamma\hbar B_0 = \hbar\omega_L$$

are found, where  $\gamma$  is the gyromagnetic ratio and  $\omega_L$  is defined as the *Larmor frequency*. According to Boltzmann statistics, the energy difference will be translated into a population difference in states with the result of a net magnetic moment  $\vec{\mu}$  based on the population difference between the  $\alpha$  and  $\beta$  states. Treating this magnetic moment in the electro-dynamical 'classical' sense, it will be oriented parallel to  $B_0$  due to an acting torque  $T$  of magnitude

$$T = \mu \times B_0$$

and result in a build-up of so-called *longitudinal magnetization*  $M_z = d\mu/dV$  [96] over a time scale  $T_1$  (called spin-lattice relaxation). An additional consequence of this electro-dynamic treatment is the precession of  $\mu$  around the director of  $B_0$  with the Larmor frequency with  $\omega_L = 400$  MHz for all high-field measurements ( $B_0 \approx 9.4$  T) and  $\omega_L = 20$  MHz for all low-field ( $B_0 \approx 0.5$  T) in this work.

As NMR does not detect  $M_z$ , but only parts of the magnetization that are perpendicular to  $B_0$ , the longitudinal magnetization is manipulated by applying radiofrequency (rf) pulses



with a much smaller magnetic field  $B_1$  (and a director usually perpendicular to  $B_0$ ) that is in resonance with the precession frequency  $\omega_L$  [96]. Application of these pulses for a suitable duration (*pulse length*) results in a rotation of  $M_z$  around the director of  $B_0$  onto the transversal x-y plane and a transformation of  $M_z$  to  $M_x$  or  $M_y$ .

The precession of  $M_{x/y}$  with  $\omega_L$  (for the case of an isolated single spin) can be detected by a coil within the probe head part of the spectrometer, as the rotating magnetic field will induce a current of the same frequency within the coil due to Ampère’s circuital law (or Maxwell’s 4th law).

The resulting signal will be an oscillation modulated by a decaying exponential function (other shapes may arise due to technical specifications or multispin interactions), which is called the *Free Induction Decay* (FID). The decay time scale is characterized by the  $T_2$  relaxation time, which in turn depends on a variety of factors, including magnetic field homogeneity and spin-spin interactions.

Using this as a basis, NMR can access structural information on the molecular level about substances by studying shifts of the energetic gap (and therefore the measured frequency  $\omega = \omega_L \pm \Delta\omega$ ) based on additional spin-based interactions, such as chemical shifts, dipolar couplings or J-couplings. In general, it can be said that nearby nuclei will influence the precession frequency of an observed nucleus/spin by partially shielding it from the static magnetic field (chemical shift), via through-space coupling of spins through their local magnetic fields (dipolar coupling) or by indirect coupling through chemical bonds (J-coupling). In the simplest case, the chemical structure of a probe can be identified via a Fourier transform of the superposed FID signal of the individual spins; more refined statements on, e.g., molecular dynamics can be made by studying the interactions through rigorous application of quantum mechanics and thereof derived pulse sequences (see the following sections for exemplary applications). Depending on the specific sample and the timescale of its molecular reorientation through Brownian motion, e.g. a small molecule in solution (fast) vs. a polymeric chain in a rubber (slow), some of the aforementioned interactions can be neglected, as their orientational dependence will result in averaging of the interactions toward zero. Although the chemical shift will have an isotropical average unequal zero, leaving the possibility of studying molecules in solution (*solution NMR*), the dipolar interaction will be fully averaged out and only be relevant once molecules exhibit molecular motions slower than the interaction frequency ( $\approx$  kHz) or have significant motional constraints. The latter regime, being dominated by dipolar couplings, is commonly called *Solid-state NMR* and will be discussed in the following section.

## 3.2 Dipolar interaction in solid-state NMR

As mentioned above, the regime of solid-state NMR is mainly governed by orientation-dependent interactions, which being the chemical shift anisotropy (orientation-dependent shielding effects of the observed nucleus from the external magnetic field  $B_0$  by surrounding electrons), the dipole-dipole interaction (through-space coupling of nearby nuclei with  $I \neq 0$  due to their local magnetic fields), and the quadrupolar interaction (local electric field gradients for spins with  $I > 1/2$ ). As a result, it is found that the spectral line of a given

nucleus depends not only on its environment but also on the orientation of the respective interaction vector with respect to  $B_0$ . Although fundamentally different in physical nature, they unite as a consequence of a change in the observed interaction frequency  $\omega$  by a few Hz to several tens of kHz [99]. Although, generally speaking, these interactions must be discussed separately in terms of their interaction matrices, this work refrains from doing so because only the homonuclear dipolar coupling between neighboring protons will be relevant for the upcoming chapters. It has the special property of an underlying axial symmetry (parallel to the connecting vector), hence the relevant calculus can be broken down to a scalar value, as well as a single angle  $\theta$ , being the angle between the proton-proton connection vector and  $B_0$ , which will be briefly mentioned below.

Generally, the dipolar coupling interaction between two neighboring nuclei is caused by their magnetic moment  $\vec{\mu}$  (assuming that they have a non-zero nuclear spin) and can be described by a Hamilton operator (equivalent to the textbook case of two magnetic dipoles in spatial vicinity):

$$H_{\text{DD}} = \sum_{i < j} \frac{\hbar \mu_0 \gamma_i \gamma_j}{4\pi r_{ij}^3} \left( \vec{I}_j \cdot \vec{I}_i - 3 \frac{(\vec{I}_i \cdot \vec{r}_{ij})(\vec{I}_j \cdot \vec{r}_{ij})}{r_{ij}^2} \right) \quad (3.1)$$

Here,  $\gamma$  are the respective gyromagnetic ratios,  $\vec{r}_{ij}$  is the internuclear vector (pointing from one nucleus to the other) and  $\vec{I}$  are the spin operators. The distance-dependent prefactor of the brackets can be condensed into  $D_{12}$  and is then called the dipolar coupling constant and serves as a measure of the interaction strength. Depending on the relative orientation (parallel or antiparallel), two different potential energies are accessible, resulting in a possible spectral doublet. The resulting spectral shift can then be described by  $\omega_0$  (the interaction strength) and the second Legendre polynomial  $P_2(\cos \theta)$  (the orientation dependence), which yields the following form:

$$\omega(\theta) = \pm \omega_0 P_2(\cos \theta) \stackrel{\text{homo.}}{=} \pm \frac{3}{2} D_{12} P_2(\cos \theta) \quad (3.2)$$

Consequently, the real part of the observed FID (within the rotating frame) will be modified by the emerging spread of spectral lines, leading to a signal of the form

$$I_{\text{FID}}^\dagger \propto \cos(\omega_0(3 \cos^2 \theta - 1)t) \quad (3.3)$$

for a single spin pair orientation, as well as

$$I_{\text{FID}} \propto \langle I_{\text{FID}}^\dagger \rangle_\theta = \int_0^\pi \cos(\omega_0(3 \cos^2 \theta - 1)t) \sin \theta d\theta \quad (3.4)$$

as the result for a sample with isotropic distribution of orientations, where  $\langle \dots \rangle_\theta$  denotes the average over all orientations and will be referred to as *powder average*. The emerging shape  $I(\omega)$  in the spectral domain is called *Pake pattern* (see Figure 3.2) and will have a width equivalent to  $3D$  with two distinct peaks separated by  $3/2D$  (see Figure 3.2). In practical applications, however, isolated spin pairs are rarely observed. Instead, complex multi-spin systems are more commonly encountered. As a result, the distinct and well-defined Pake

pattern of most substances becomes washed out, making it difficult to use the spectral response to determine the value of  $D_{12}$  or even the average value  $D_{\text{avg}}$ . To access intra- or intermolecular distances, as described in e.g., ref. 3.2, more sophisticated techniques are required. These techniques mostly operate in the time domain because there is simply no advantage of using the Fourier transform because of the presence of multi-spin interactions and the chemical simplicity of many polymers. The following sections will delve into one of these advanced methods, being Time-Domain Multi-Quantum (MQ) NMR, that can be used to access the dipolar coupling values of substances within the rubbery plateau.

### 3.3 Relationship of dipolar interactions and local chain motion

As mentioned before, the orientation dependence of the dipolar couplings of a spin pair follows the second Legendre polynomial  $P_2(\cos \theta)$ . It will be reasoned that a similar observable (following the same orientational dependence) is found in polymers and thus the suitability of mapping observable dipolar couplings onto polymer dynamics will be shown. For now, it is assumed that the polymer chain of interest will be far above the glass transition temperature  $T_g$ , therefore displaying fast intra-segmental motions. The set of spin pairs is assumed to be rigidly attached to the moving chain, which, as shown by Cohen-Addad et al. [100, 101] and Brereton et al. [102, 103] leads to a pre-averaging of the individual dipolar coupling (see Figure 3.1). Therefore, a chain can be thought of as a set of *NMR submolecules* (an idea that strongly resembles the idea of the Kuhn segment of eq. 2.6) with each of these having its own dipolar coupling vector being close to parallel to the backbone chain, as long as the chain segment of interest is not motionally decoupled by, e.g. residing in a side chain or other peculiarities. Note that the exact size of the NMR submolecule is vastly different for both authors (see ref. [102]), which, however, for the following discussion does not matter due to another effect: The dipolar truncation effect, see [104, 105], which describes how the presence of strong dipolar-coupled spin pairs can influence the observation of long-range weakly coupled protons, causes an apparent narrowing of the range of observed dipolar couplings. Therefore, we can assume for simplicity that our chain will have a measurable effective dipolar coupling value ( $D_{\text{eff}}$ ), which is then mapped to the polymer chain by introducing the concept of the segmental order parameter  $s$  [106, 107] as will be shown in the next equations. The segmental order itself is defined as

$$\mathbf{s} = \frac{1}{2} [(3\langle \cos^2(\beta) \rangle) - 1] = \frac{3}{5} \left( \frac{lR^2}{R_0^2} \right)^2 \quad (3.5)$$

Here,  $\mathbf{s}$  is the segmental (tensor) order parameter,  $\beta$  is the angle between the orientational vector of the polymer segment and the end-to-end vector,  $\langle \dots \rangle$  denotes the thermal average over all conformations and  $[ \dots ]$  denotes the bulk average over all segments. For this to be valid (and additionally converge to a non-zero value), it is assumed that the chain experiences orientational constraints at the chain ends due to e.g. crosslinks or entanglements. The same order parameter can also be defined in terms of the above-discussed  $D_{\text{eff}}$  by measuring its reduction due to chain motions. The residual dipolar coupling that survives the

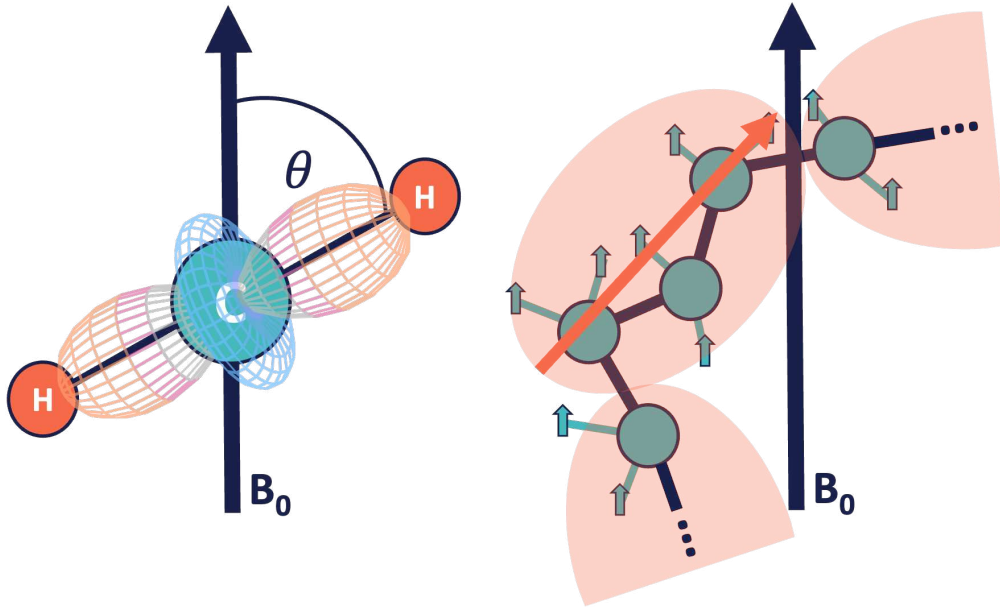


Figure 3.1: Left: visual representation of the dipolar coupling tensor of a CH<sub>2</sub>-group with the definition of the angle  $\theta$  and the external magnetic field  $B_0$  as a reference. Right: tentative picture of the definition of the NMR submolecule (and the pre-averaged dipolar coupling vector shown as red arrow) according to Cohen-Addad within a polymer chain consisting of CH<sub>2</sub>-groups. It can be seen that it comes close to the simplification procedure of a complex polymer chain used for the definition of a Kuhn monomer.

(incomplete) thermal average over all conformations is defined in terms of an orientational autocorrelation function (OACF)  $C(t)$  as follows:

$$C(|t_a - t_b|) = \langle P_2(\cos \theta_b) P_2(\cos \theta_a) \rangle \quad (3.6)$$

For the case of an isotropically-moving chain, the structural average for both eq. 3.5 as well as eq. 3.6 will approach zero, while structural constraints will result in a non-zero average due to incomplete sampling of all angles  $\theta$ . For the case of the OACF, this results in a functional form, as shown in Figure 3.2, where the order parameter  $S_b$  is found as the squared long-term limit value. Both order parameters are of the same value up to a constant  $k$  (originating from the pre-averaged  $D_{\text{eff}}$ ) that cannot be estimated a priori, as it depends on the specific molecular structure of interest. Therefore, we can now define the non-zero residual dipolar coupling (RDC) in terms of an order parameter  $S_b$ , as well as in terms of the length of a network strand (using eq. 3.5) as follows:

$$S_b = k \frac{D_{\text{res}}}{D_{\text{stat}}} = \frac{3R^2}{5N} \quad (3.7)$$

From this, it is immediately evident, that the accessibility of the RDC allows the investigation of polymeric samples in terms of e.g., rubber-, network-, or swelling theory, as will be shown in Chapter 6. It should be noted that the latter equation is only valid when  $C(t)$  shows a flat plateau value (and thus  $S_b$  can be properly defined as shown in Figure

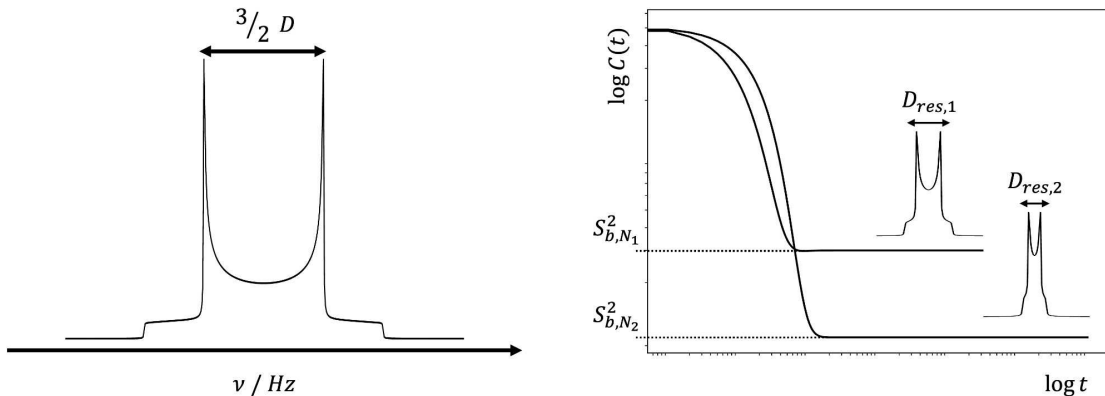


Figure 3.2: Left: Exemplary plot of an ideal Pake pattern for a rigid solid. Right: Conceptual sketch of the orientational autocorrelation function (OACF) explained in section 3.3 for an elastomer with two different residual dipolar couplings (RDCs) after incomplete averaging of  $D_{\text{eff}}$  due to motional constraints.

3.2). From now on, it is always assumed that the discussed system is a crosslinked polymer network, therefore fulfilling this requirement.

### 3.4 Static $^1\text{H}$ MQ NMR

Proton Multi-Quantum NMR ( $^1\text{H}$  MQ NMR) is an umbrella term for a set of methods whose aim it is to quantify the non-zero RDCs in systems where the motion of the respective moieties is constrained, such as entangled or crosslinked polymer systems, as well as liquid crystals or even some biological systems. In general, this subclass of pulse sequences follows the scheme given in Figure 3.3, which is a set of two blocks constructed equally but phase shifted (called the *excitation block* and the *reconversion block*). During the excitation block, a set of pulses and delays is used to generate coherences of even order (but predominantly second order *double quantum* (DQ) coherences) through the dipolar coupling of spin pairs. However, the hereby generated magnetization is not detectable and needs to be converted to observable magnetization, relying on the usage of a reconversion block that is symmetric to the excitation block. After the reconversion block, the longitudinal magnetization is converted to transversal (observable) magnetization.

For the case of the (improved) Baum-Pines sequence [108] used in this work, all pulses are executed with a certain relative phase shift  $\phi_{\text{ref}}$  or  $\phi_{\text{DQ}}$ . Depending on the phase shift, cycled in four  $90^\circ$  steps, either a so-called double-quantum build-up curve intensity  $I_{\text{DQ}}$ , comprising all excited multi-quantum (MQ) coherence orders  $(4n + 2)$ , or a reference curve  $I_{\text{ref}}$  comprising all  $4n$  coherence orders that did not evolve into MQ coherences, can be detected. Then a time dependency is introduced by repeating the latter pulse sequence for different DQ evolution times  $\tau_{\text{DQ}}$  by increasing either the number of excitation/reconversion cycles or by increasing the delay within a single cycle <sup>i</sup>.

<sup>i</sup>For all hereby presented static  $^1\text{H}$  MQ NMR experiments the latter variant was used due to technical advantages on the used low-field machine

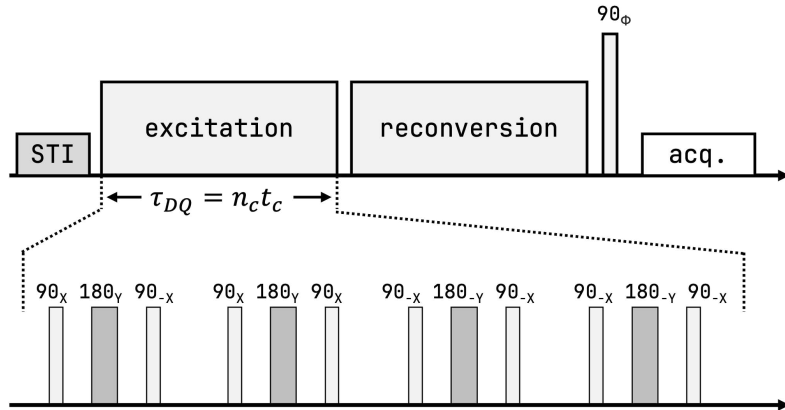


Figure 3.3: Top: Schematic representation of the MQ NMR sequence used (the improved Baum-Pines sequence [110, 111]). The STI (spin temperature inversion) block indicates an additional composite pulse to remove unwanted longitudinal magnetization [112]. Although not strictly necessary, it improves the reliability towards the regime where  $\tau_{DQ} \approx T_1$ . The phases of the read-out pulse at the end follow phase cycles of  $\phi = [x, -x, x, -x]$  for recording  $I_{DQ}$  and  $\phi = [x, y, -x, -y]$  for recording  $I_{ref}$ , while the overall sequence and receiver phase follow a CYCLOPS supercycle (not described here, see e.g., ref. [113]) .

For the case of polymers, the RDC values corresponding to elastically active network chains are found in  $I_{DQ}$  in the form of a build-up curve with a superimposed exponential relaxation function, whereas all magnetization that has not evolved into  $4n + 2$  coherence orders (including all  $4n$  quantum coherences, as well as sample moieties with RDC=0 ) are found in  $I_{ref}$  with the same exponential term. Therefore, by adding both functions and quantifying the exponentially decaying excess component (often called *tail*) towards long  $\tau_{DQ}$  (where the corresponding  $I_{DQ}(\tau_{DQ}) = 0$ , one can, e.g., quantify the relative proton fraction of the isotropic component (e.g., isotropically moving defects, unlinked precursors (sol) or protonated solvent), allowing for an estimate of network defects.

In the following, a short overview of possible evaluation methods of the data obtained from the Baum-Pines MQ NMR sequence will be given (more details can be found, for example, in [54, 109]). A rather complex procedure is necessary, because the desired RDC values cannot be easily extracted from  $I_{DQ}$ , as it is a multiplicative superposition of the RDC-encoded build-up curve and an exponential  $T_2$ -like relaxation term that is dominated by the segmental motions of the polymer backbone. However, due to recording of the reference function  $I_{ref}$ , prior knowledge of the relaxation term can be obtained by calculating the sum function  $I_{\Sigma MQ} = I_{DQ} + I_{ref}$ , which is equivalent to a fully refocussed (=relaxation-only) dipolar echo. This leads to two possible ways of handling it: In short, it can be eliminated by manipulating the  $I_{DQ}$  data or the nonlinear regression procedure can be modified so that it handles both data sets  $I_{DQ}$  and  $I_{\Sigma MQ}$ , simultaneously.

### 3.4.1 Evaluation by point-by-point normalization

One way to evaluate the pairwise sets of  $(I_{ref}, I_{DQ})$  data obtained by the Baum-Pines experiment makes use of a point-by-point normalization approach to eliminate the relaxation function and thus access the non-relaxing normalized DQ intensity contribution  $I_{nDQ}$ . To

be applied successfully, two small empirically motivated assumptions are made: (1) For a given dipolar coupling  $D_{\text{res},i}$ , there is no significant difference in the transverse relaxation time  $T_{2,i}$  for the coherence orders  $4n + 2$  (MQ signal) and remaining coherence orders  $4n$  (reference signal) of the associated spins, thus justifying that both curves can be fitted using the same relaxation function. (2) The  $I_{\Sigma MQ}$  signal will consist of a superposition of one relaxing component ( $T_{2,\text{el}}$ ) corresponding to the elastically active sample fraction, as well as a singular isotropic tail that relaxes with a monoexponential decay ( $T_{2,\text{tail}}$ ) with  $\beta = 1$ . Under these assumptions, the tail can be quantified by fitting the long-time component of  $I_{\Sigma MQ}$  towards long  $\tau_{\text{DQ}}$  (see Figure 3.4) and the result used for a calculation of the pure DQ build-up function by point-by-point normalization as follows.

$$I_{\text{nDQ}} = \frac{I_{\text{DQ}}(\tau_{\text{DQ}})}{I_{\text{ref}}(\tau_{\text{DQ}}) + I_{\text{DQ}}(\tau_{\text{DQ}}) - f_{\text{tail}} \cdot \exp(-\tau_{\text{DQ}}/T_{2,\text{tail}})} \quad (3.8)$$

The normalized DQ intensity  $I_{\text{nDQ}}$  has to reach the plateau value of  $I = 0.5$  due to an equal partitioning of excited  $4n$  and  $4n + 2$  coherences over  $I_{\text{ref}}$  and  $I_{\text{DQ}}$  after subtracting the isotropic fraction  $I_{\text{tail}}$  [53]. The modeling of  $I_{\text{nDQ}}$  itself can be realized by a set of different functions, depending on the specific use case. While originally an inverted Gaussian of the form  $I_{\text{nDQ}} = 0.5(1 - \exp(-kD_{\text{res}}^2\tau_{\text{DQ}}^2))$  was used (see ref. [114] for explanations and application of the second-moment approximation), nowadays an empirical function found by Chassé et al. [115], the so-called *Abraham-like* (A.-l.) function is used, as it models the true multi-spin build-up curve of the observed  $I_{\text{nDQ}}$  functions more accurately. It reads as follows:

$$I_{\text{nDQ}}(\tau_{\text{DQ}}) = 0.5[1 - \exp(-(0.378D_{\text{res}}\tau_{\text{DQ}}))^{1.5} \cdot \cos(0.583D_{\text{res}}\tau_{\text{DQ}})] \quad (3.9)$$

For networks that display a smoothly distributed RDC (due to, e.g., spatial crosslinking inhomogeneities), one can evaluate  $I_{\text{nDQ}}$  using a distribution function:

$$I_{\text{nDQ}} = \int_{-\infty}^{+\infty} P(D_{\text{res}})I_{\text{nDQ}}(D_{\text{res}}) dD_{\text{res}} \quad (3.10)$$

The most sensible distribution function here would be a numerically calculated log-normal distribution, as the simple approach of using a Gaussian distribution (matching motivations from both limit theorem) can lead to the appearance of negative, and therefore nonphysical, RDC values simply due to allowing an unconstrained distribution of RDC values. In contrast, the distribution function for the log-normal distribution allows only for positive values and is therefore more suitable. It reads:

$$P_{\log}(D_{\text{res}}) = \frac{1}{\sigma\sqrt{2\pi}} \exp\left[-\frac{(\ln D_{\text{res}} - \ln D_{\text{med}})^2}{2\sigma^2}\right] \quad (3.11)$$

### 3.4.2 Evaluation by multi-component fitting approach

While the latter approach is sufficient for many cases, such as well-defined elastomers (see e.g., ref [116] and references therein), it rigorously fails for the special case investigated in

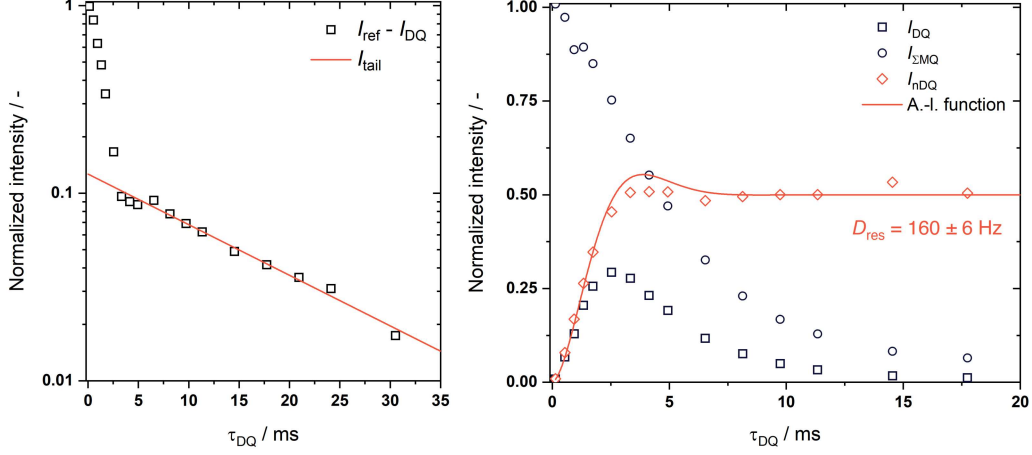


Figure 3.4: Exemplary point-by-point normalization MQ NMR fitting procedure on natural rubber at  $T = 70^\circ\text{C}$  as described in the text. Left: The tail-fitting procedure is shown using the relaxation data with the trick of plotting  $I_{\text{ref}} - I_{\text{DQ}}$  in order to make use of the fact that  $I_{\text{tail}} = I_{\text{ref}} - I_{\text{DQ}}$  when  $I_{\text{nDQ}}$  has reached the plateau. As can be seen, the tail can be easily identified and reliably fitted, yielding about 12% of isotropic defects (in this case mostly dangling chains). Right: Plot of all relevant data sets for full evaluation.  $I_{\text{nDQ}}$  was estimated using eq. 3.8 and fitted using the A.-l. function of eq. 3.9, yielding an RDC value of  $D_{\text{res}} = 160 \pm 6 \text{ Hz}$

this work, being gels made from star-shaped networks. As explained in detail in section 2.3.2, this special type of network mainly displays a certain set of discrete chain connectivity motifs, each of which has a distinct effective molecular weight and associated RDC value. Hence, investigations of  $I_{\text{DQ}}$  of this type of material display a superposition of discrete A.-l. functions weighted by the proton fraction ( $a_i$ ) with a different tuple of parameters ( $a_i, D_{\text{res},i}, T_{2,i}, \beta_i$ ). Therefore, the two signal functions can now be written as a superposition of  $n$  distinct connectivity motifs:

$$I_{\text{DQ}} = \frac{1}{2} \left( \sum_{i=1}^n a_i I_{\text{a.-l.}}(\tau_{\text{DQ}}, D_{\text{res},i}) \cdot \exp[-\tau_{\text{DQ}}/T_{2,i}]^{\beta_i} \right) \quad (3.12)$$

$$I_{\text{SMQ}} = \left( \sum_{i=1}^n a_i \exp[-\tau_{\text{DQ}}/T_{2,i}]^{\beta_i} \right) + a_{\text{tail}} \exp[-\tau_{\text{DQ}}/T_{2,\text{tail}}] \quad (3.13)$$

While one may be tempted to use the approach described above and correct for the discrete components by defining a  $I_{\text{nDQ}}$  as a superposition of A.-l.-functions, care should be taken,



as the point-by-point normalization now rigorously fails due to the following fact:

$$\begin{aligned}
I_{\text{nDQ}} &= \frac{\sum_{i=1}^n a_i I_{\text{a.-l.}}(\tau_{\text{DQ}}, D_{\text{res},i}) \cdot \exp[-\tau_{\text{DQ}}/T_{2,i}]^{\beta_i}}{\sum_{i=1}^n a_i \exp[-\tau_{\text{DQ}}/T_{2,i}]^{\beta_i}} \\
&\neq \frac{\sum_{i=1}^n a_i I_{\text{a.-l.}}(\tau_{\text{DQ}}, D_{\text{res},i})}{\sum_{i=1}^n a_i} \\
&\neq \sum_{i=1}^n a_i I_{\text{DQ},i}(\tau_{\text{DQ}})
\end{aligned}$$

In order to circumvent the fact that  $I_{\text{nDQ}}$  cannot be calculated by this approach, Lange et al. [23] developed an alternative approach that analyzes the data 'as acquired' by fitting the  $I_{\text{DQ}}$  using the A.-l. function (eq. 3.9) in conjunction with a stretched exponential. However, since a regression procedure based on  $I_{\text{DQ}}$  is not possible due to the sheer number of parameters needed (3 per component + 2 for the tail fit), Lange et al. invented a simultaneous fitting procedure where the number of parameters is dealt with by simultaneously fitting both the  $I_{\Sigma\text{MQ}}$  and the  $I_{\text{DQ}}$  signals to the eq. 3.4.2. Therefore, the parameters for the relaxation functions ('shape parameters') and the individual proton fractions  $a_i$  are shared among both curves during the regression procedure. In the following, an exemplary evaluation procedure on a tPEG-tPCL gel will be given.

As already mentioned in section 2.3, the synthesis of polymer gels based on well-defined star-shaped precursors results in a network, where individual chain-level connectivity motifs are few and well-known. Additionally, each of the motifs results in an effective molecular weight of crosslinking  $M_c$  that is very different from the other. Consequently, the RDC value of each of the different motifs will be narrowly distributed and highly different (see eq. 3.5), allowing for a quantification of the relative (proton-weighted) amounts of connectivity motifs  $a_i$  according to eq. 3.4.2 and a top-bottom argumentation in such a way that the highest RDC value that is found must correspond to the lowest  $M_c$  if there is confidence that no structures with higher restricted motional anisotropy exist (such as chain clusters) (see Figure 3.5 for a scheme). Then, the obtained MQ NMR data can be evaluated as shown exemplarily in Figure 3.5. Although in the initial publication of Lange et al. [23], a simultaneous annealing algorithm was used to further aid the regression procedure, in this work a modified approach was developed that will be explained later in section 6.1.

### 3.5 $^1\text{H}$ MAS DQ-NMR: The POST-C7 Experiment

Due to the solid nature of the samples typically investigated by the static Baum-Pines experiment, the acquired spectrum of substances with RDC  $\neq 0$  will always be a featureless one, as the chemical shifts induced by RDCs usually exceed most naturally occurring chemical shift differences. Therefore, the aforementioned static Baum-Pines sequence will not be able to yield information on RDC values with chemical information. A common solution to this problem is *magic-angle spinning* (MAS), which is able to remove remaining

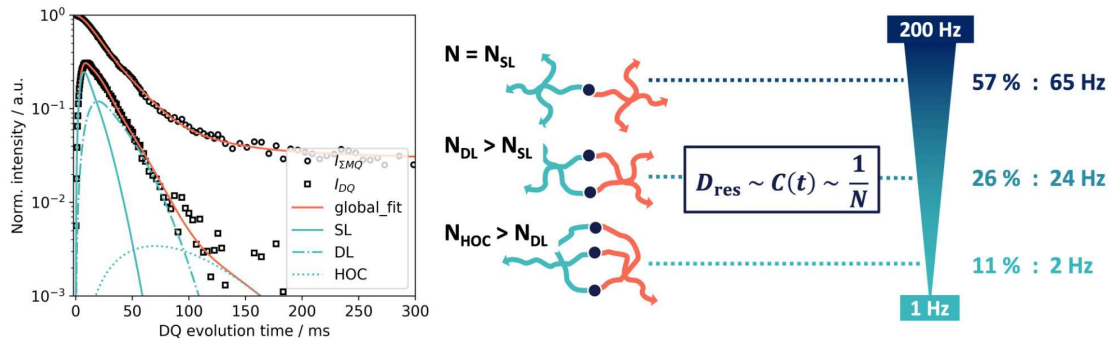


Figure 3.5: Left panel: Evaluation of a tPEG-SH ( $c_{\text{prep}} = 2.5 c^*$ ) sample in water (see section 5.1.2 for details) by the multi-component fitting procedure described here. Right panel: visualization of the assignment strategy used in the left panel. By knowing all possible connectivity motifs in advance, a top-bottom approach of assigning these by comparison of RDC values can be used. As a result, both proton fraction and corresponding RDC value can be quantified.

RDCs by macroscopically rotating the sample around an axis that is tilted by an angle  $\theta_m = 54.7^\circ$  with respect to the external magnetic field  $\vec{B}_0$ . It is found [117, 118], that a rotation by a frequency  $\nu_{\text{rot}}$  faster than the respective interaction frequencies  $\omega_d, \omega_{\text{CSA}}$  yields a high-resolution spectrum of the substance, where only the isotropic lines (and spinning sidebands, that will not be discussed in this work) are found. The specific value of the magic angle is related to the dipolar Hamiltonian (see eq. 3.1) and the fact that it vanishes for  $\theta = \theta_m$ .

Although the application of MAS alone produces spectra with high resolution, a simple usage of the Baum-Pines sequence on top of the rotation will fail for  $\tau_{\text{DQ}} > 0.5 \tau_{\text{rot}}$ , due to the averaging of the RDCs upon completion of a rotor period. With conventional spinning speeds as low as about 1 kHz without sacrificing spinning stability, an upper limit is found at  $\tau_{\text{DQ}} \approx 0.5$  ms. Hence, an alternative approach called recoupling was developed that essentially makes use of rotor-synchronized pulse sequences such as DRAMA [119], BABA [120] and C7 [121] in order to reintroduce the dipolar interaction during acquisition of a high-resolution spectrum. In this work, only the C7 sequence is relevant and will be briefly discussed in the following.

The C7 pulse sequence is a recoupling sequence proposed by Lee et al. [121] which was later abstracted into a general framework of symmetry-based sequences, referred to as  $CN_n^\nu$  sequences [122]. In short, the sequences make use of the rotational properties of the NMR interaction tensors and separate concerns based on external "space" rotations and internal "spin" (interaction tensor) rotations into multiplicative terms. It can be shown [122], that suitable pulses ("spin space rotations") can lead to changes, suppression, or reintroduction of certain interactions, such as the homonuclear dipolar coupling Hamiltonian.  $CN_n^\nu$  sequences subdivide  $n$  rotational MAS periods into equal intervals  $N$ , where each interval experiences a radio frequency pulse of phase  $k \cdot 2\pi\nu/N$  with  $k$  being the incremented index of the interval. This results in an increasing rotation of the nuclear spins by integer multiples of  $360^\circ$ , which, depending on the specific rotational properties of the desired interaction, can lead, for example, to a reintroduction or suppression. For

the C7 (or more specifically the  $CN_2^1$ ) sequence, this translates into a set of two pulse trains with seven pulses each, where each pulse has a phase incremented by  $k \cdot 2\pi/7$ . The pulse length is adjusted so that  $\omega_{\text{nut}} = 7\nu_{\text{rot}}$ , which means that the pulse train provides a nutation frequency seven times the spinning frequency. An additional improvement was found by Hohwy et al. [123], who proved that the usage of a composite pulse of the form  $C_\phi^{143} = (\pi/2)_\phi(2\pi)_{\phi+\pi}(3\pi/2)_\phi$  - instead of a single pulse as the basic element - provides greater stability against accidental deviations from  $\omega_{\text{nut}}$ , as well as cancelation of unwanted interaction terms up to a higher (5th) order in theoretical calculations (see Figure 3.6 for a scheme). This slightly modified sequence is called POST-C7.

Eventually, a high-resolution MAS spectrum is obtained with an additional excitation of DQ coherences for a time  $\tau_{\text{DQ}} \approx 2n_c(1/\nu_{\text{rot}})$ , where  $n_c$  is the number of cycles / pulse trains that the experimenter chooses. Small deviations from this may arise from experimental imperfections such as phase switching times between the pulses and additional needed delays. Therefore, repeated use of this experiment for different  $n_c$  yields a 2D data set with a set of high-resolution MAS spectra at incremented DQ evolution times. Using the same phase trick as in the Baum-Pines experiment described above, one can now obtain  $I_{\text{ref}}$  and  $I_{\text{DQ}}$  signals with chemical resolution (see Figure 3.7). After slicing along the indirection dimension, the data can, similar to the static version, be evaluated using, e.g. the A.-l. function. However, due to a caveat of the  $CN_n'$  sequences, the observed RDC values will be scaled by a factor  $\epsilon \in (0, 1)$ , leading to a slightly modified A.-l. function as follows:

$$I_{n\text{DQ}}(\tau_{\text{DQ}}) = 0.5[1 - \exp(-(0.378\epsilon D_{\text{res}}\tau_{\text{DQ}}))^{1.5} \cdot \cos(0.583\epsilon D_{\text{res}}\tau_{\text{DQ}})] \quad (3.14)$$

For the case of the POST-C7 experiment, it takes a value of  $\epsilon = 0.232$  [123].

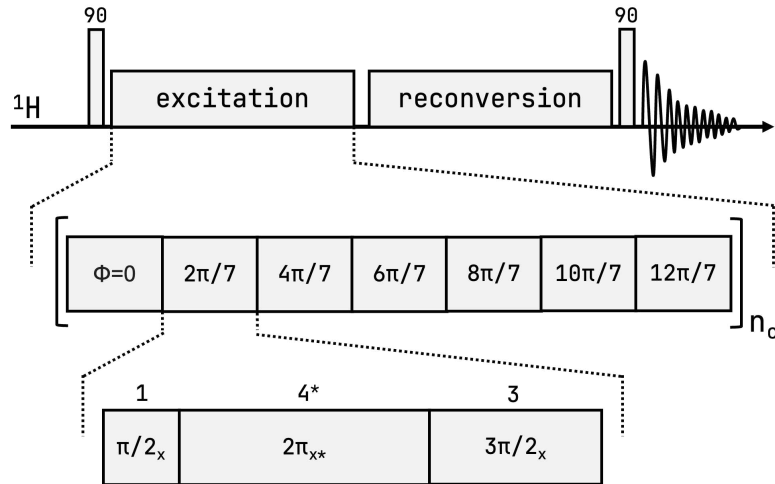


Figure 3.6: POST-C7 sequence according to ref. [123]

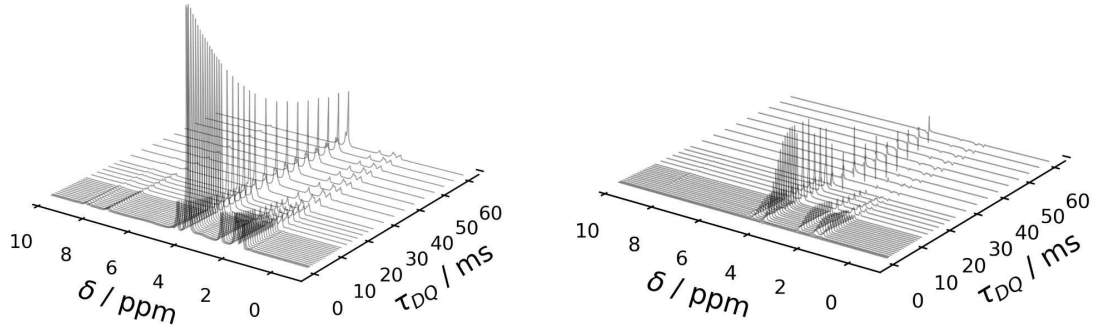


Figure 3.7: Exemplary experimental of a MAS DQ NMR experiment on a PEG-PCL ACPN swollen in  $d_8$ -Toluene at  $T = 30^\circ \text{C}$  and a spinning speed of  $\nu_{\text{rot}} = 5000 \text{ Hz}$ . Left: Obtained  $I_{\text{ref}}$  spectra from the POST-C7 experiment separated along the indirect ( $\tau_{\text{DQ}}$ ) dimension. Right: Obtained  $I_{\text{DQ}}$  spectra from the POST-C7 experiment separated along the indirect ( $\tau_{\text{DQ}}$ ) dimension. Towards long  $\tau_{\text{DQ}}$ , the  $I_{\text{DQ}}$  data display a nonzero fluctuating value possibly arising from magnetic field inhomogeneities along the radial dimension of the sample.

### 3.6 Pulsed-Field Gradient NMR

Pulsed-field gradient (PFG) NMR is an experimental method for encoding spatial information into the spins by applying pulsed gradients to determine translational self-diffusion coefficients. The groundwork was laid by Hahn [124] and Carr and Purcell [125], assessing changes in the refocusing efficiency of Spin Echoes (SE) in the presence of self-diffusion in inhomogeneous magnetic fields. Later, Stejskal and Tanner [126] expanded on this idea by proposing an experiment based on the variation of the strength  $g(z) = g_0 z$  of a linear external field gradient as a way to spatially encode the spins and interfere with the efficiency of the spin echo based on its relative position change along the axis  $z$ . Although the chosen echo sequence, being the spin echo (SE) [126] or the stimulated echo (STE) [127], comes with certain sets of specific implementations, the overall theory is similar and contains only minor differences. In the following, a brief explanation will be given on the example of the PFG-SE pulse sequence (see Figure 3.8 for a sequence scheme):

The sequence starts with a simple excitation based on a  $90^\circ$  pulse in order to rotate spins to the transverse plane, where they will start to dephase with different Larmor frequencies based on chemical shifts,  $T_2$  relaxation, and magnetic field inhomogeneities. During that time, the pulsed gradient will act for the first time, producing a rectangular<sup>ii</sup> gradient of duration  $\delta$  and strength  $g(z)$ , where  $z$  is the axis parallel to the static magnetic field. Therefore, the spins will experience an additional phase shift  $\Delta\phi$  in addition to the 'regular' evolution, which depends on their position along the  $z$  axis as follows:

$$\Delta\phi_g(z) = \gamma g z \cdot \delta$$

The gradient pulse is followed by a delay of duration  $\Delta$ , in which diffusion is supposed to

<sup>ii</sup>In practice, many different gradient shapes are common. As long as  $\int g(t)dt$  can be mapped upon a single equivalent rectangular gradient, the following calculations will be valid.

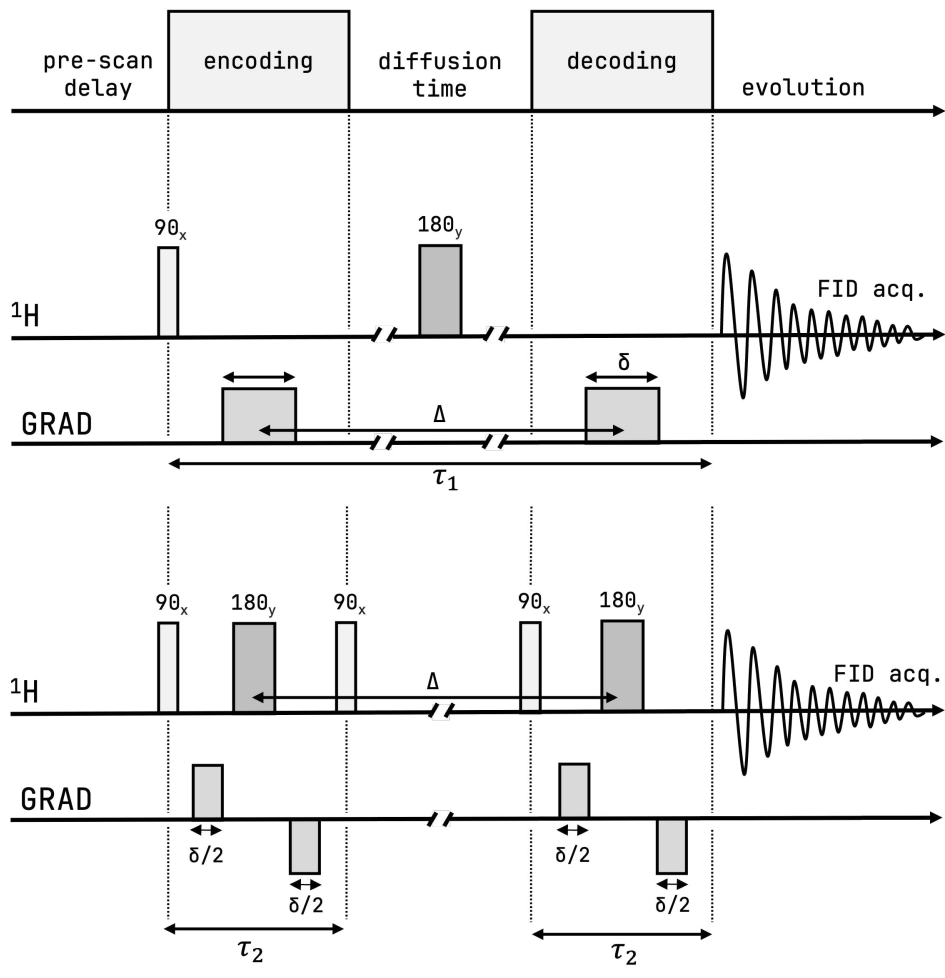


Figure 3.8: Schematic representation of the two NMR sequences used in this work. Top: Spin-Echo (SE) sequence with unipolar gradients. Bottom: Stimulated-Echo Sequence with (optional) bipolar gradients (STEbp).

occur. At  $t = \Delta/2$  a  $180^\circ$  pulse will be applied to refocus the dephasing spins by inverting the accumulated phase shifts. Finally, a second pulsed gradient of equal length and strength is applied, which will cancel out the effects of the first gradient pulse, assuming that the spins have not changed their position along the  $z$ -axis due to translational diffusion. The overall phase shift of a spin  $i$  can be written as [126]:

$$\begin{aligned}\Delta\phi_i(z(t), z(t + \Delta)) &= (\gamma g z(t) \delta + \omega_L \frac{\Delta}{2}) - (\gamma g z(t + \Delta) \delta + \omega_L \frac{\Delta}{2}) \\ &= -\gamma g \delta (z(t) - z(t + \Delta)) \\ &= \begin{cases} 0 & \text{for } z(t) = z(t + \Delta) \\ -\gamma g \delta (\Delta z) & \text{otherwise} \end{cases}\end{aligned}\quad (3.15)$$

From eq. 3.15 it is easily found that the phase mismatch acquired during the PFG-SE sequence is zero when no diffusion along the  $z$ -axis occurs, while it equals a nonzero value in the other case. Here, a nonzero value will translate to a lower efficiency in the spin echo, therefore, a loss in intensity in the spectrum, with the specific amount dependent on the overall distance (which can be mapped onto the mean-square displacement using eq. 2.25). For an analytical expression of  $I(g)$ , several assumptions need to be made, which will be briefly mentioned in the following. For a more comprehensive explanation, the reader is referred to ref. [128].

(1) Gaussian Phase Distribution (GPD): The distribution of phases during dephasing follows a Gaussian distribution that can be characterized by the mean square phase change  $\langle\phi^2\rangle$ . Generally, a phase distribution function  $P(\phi, \Delta)$  is needed to characterize the decay of spectral intensity  $I(g)$ .

(2) Short Gradient Pulse (SGP) Approximation: It is assumed that the samples do not move during the gradient pulse, as the short time in which movement would need to be considered cannot be expressed analytically. The validity of this approximation is vital for the following expression for  $I(g)$  and therefore experimental realization is crucial. In the simplest case, it is realized by keeping  $\delta$  much shorter than  $\Delta$ .

(3) Constant  $T_2$  relaxation: For cancelation of overlapping signal decays due to  $T_2$  relaxation, only the relative change in intensity is evaluated. If the  $T_2$  relaxation is assumed to be constant across all applied gradients, it will cancel out, leaving a relaxation-free signal decay. This assumption is usually fulfilled to a great extent, as the relative changes ( $B_0$  vs.  $g$ ) are small.

Using the assumptions above [126, 128], we arrive at the following equation for the decay of the normalized echo amplitude under varied gradient strength  $g$  and constant diffusion time  $\Delta$ :

$$\frac{I(g)}{I(0)} = \exp(-\gamma^2 g^2 D \delta^2 (\Delta - \delta/3)) \quad (3.16)$$

It is easily seen, that this equation only depends on a single parameter, being the long-term diffusion coefficient  $D$ , whereas all other parameters are either spin-specific properties ( $\gamma$ ) or experimentally defined timescales ( $\delta, \Delta$ ).

Common restrictions of PFG-NMR arise due to very short  $T_2$  relaxation times of the studied samples, which cause the signal to decay significantly during the diffusion time, as

it is not uncommon for proteins, colloids, or other macromolecules to have  $T_2$  relaxation times on the order of 10 – 100 ms. As a workaround, the STE-based sequence [127] (see Figure 3.8 bottom) can be used, which has the advantage of storing the magnetization along the external field  $B_0$  during  $\Delta$ , therefore limiting the signal decay to the usually much larger  $T_1$  relaxation. However, it comes with the disadvantage of recording only 50% of the overall signal due to the nature of the stimulated echo, and the other 50% being dephased during  $\Delta$  (either by waiting a sufficient time or by applying a small spoiler gradient). It should be noted, however, that the  $T_2$  filtering effect of the SE sequence may not always be a disadvantage, as it can be used to clean the spectrum of unwanted background signals, as long as these have  $T_2$  values significantly shorter than the actual diffusing species. This is the case, for example, for the diffusion of probe molecules within a static matrix/porous material. However, if the probe is heterogeneous and displays, for example, a smooth distribution of molecular weights, the same  $T_2$  filtering effect will cause a bias for mobile species, as they will be less affected.

Other restrictions may arise from technical or experimental issues and can include eddy currents that are being induced in the coils due to strong gradients being pulsed over a very short amount of time or artificially short diffusion coefficients due to background gradients arising from discrete susceptibility jumps at the sample surface (most commonly found in ion-containing samples, but also found in e.g., porous samples to an, albeit significantly lesser, extent). For specific examples, orders of magnitude, and possible solutions, the reader is referred to ref. [128], as these problems are not relevant to this work.

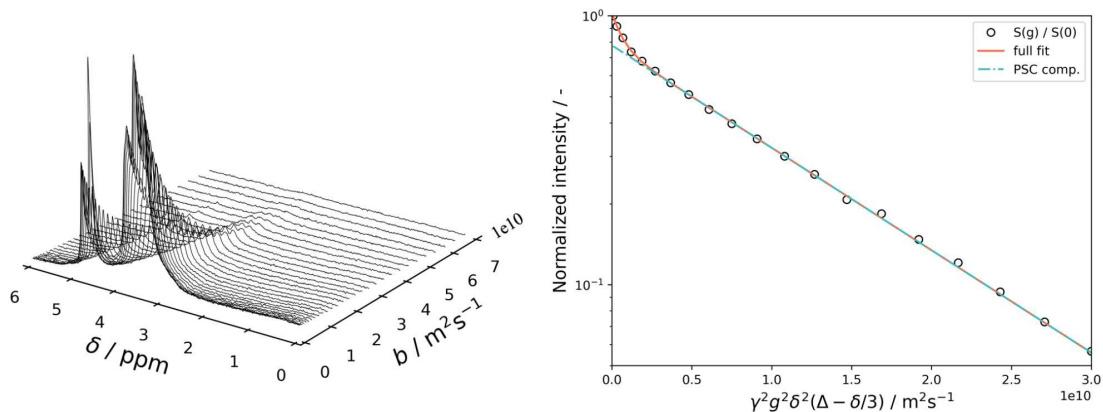


Figure 3.9: Left: Pseudo 2D data as acquired from a PFG-NMR experiment on a 5 wt% solution of Dextran-10 kDa in  $D_2O$  with a variation of the gradient strength (plotted as a reduced quantity according to eq. 3.16). Right: Reduction of the data to a 1D plot by integrating over the full spectral range. As can be seen, two components are necessary for the fit as residual HDO signal results in a two-step decay with the steeper one corresponding to  $D = 1.8 \cdot 10^{-9} \text{ m}^2 \text{ s}^{-1}$  of water, while the long-time decay corresponds to  $D = 9.4 \cdot 10^{-10} \text{ m}^2 \text{ s}^{-1}$  of the investigated Polysaccharide (PSC).

## Chapter 4

# X-Ray Scattering

### 4.1 Basic Concepts of X-Ray Scattering (SAXS)

The central concept of x-ray scattering is based on the interaction between the x-rays, most commonly produced by *Bremsstrahlung* of metallic anodes, and the electrons of the irradiated matter. The incident x-ray waves excite the outer electrons of the atomic shell, which, as a consequence, start to oscillate and show dipole behavior. This leads to an emitted spherical wave of a certain amplitude  $A$ , wave vector  $k$  and wave length  $\lambda$ . Under the assumption of elastic scattering, the wave length  $\lambda$  of the emitted wave is equal to the wave length of the incident wave  $\lambda_0$ . For a single scattering process, which is excited by a monochromatic incident wave with wave vector  $k_0$ , the scattering amplitude  $A(\vec{r})$  can be presented in the following way:

$$A(\vec{r}) = b \exp^{-i\frac{2\pi}{\lambda}(k_0 - \vec{k})\vec{r}} \quad (4.1)$$

Here,  $b$  is used to characterize the scattering cross section and  $\vec{r}$  denotes the positional vector. Extending this to an atom (depicted as a continuous media of electrons characterized by the electron density  $\rho(\vec{r})$ ), one obtains the so-called atomic *Form Factor* amplitude  $F^{\text{atom}}$  as follows:

$$F^{\text{atom}}(\vec{q}) = \int_{\text{atom}} \rho(\vec{r}) \exp^{i\vec{q}\cdot\vec{r}} \, d\vec{r} \quad (4.2)$$

Here, the commonly used scattering vector  $q = k_{\text{out}} - k_{\text{in}}$  is defined as the difference of these two wave vectors, which leads to the well-known relationship of scattering angle and magnitude of the wave vector (see e.g., ref. [129]):

$$|q| = \frac{4\pi}{\lambda} \sin(\theta) \quad (4.3)$$

The scattered intensity  $I(q)$ , or  $I(2\theta)$ , is detected as  $|F|^2$  at a fixed distance  $R$  between the sample and the detector and is commonly calculated as a normalized quantity of scattered photons per time and per solid angle (see Figure 4.1), which is often referred to as the differential scattering cross section  $\frac{d\sigma}{d\Omega}$ . Corrections are usually needed to account for background scattering (which can be subtracted from the measured scattering curve)



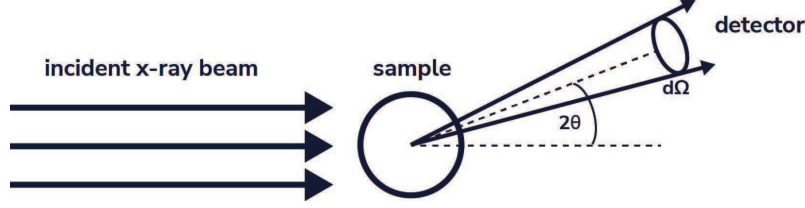


Figure 4.1: A basic sketch showing the geometry of a scattering experiment. An incident x-ray beam is scattered on a sample at an angle  $2\theta$  and the emerging spherical wave is traversing towards the detector. Here,  $d\Omega$  denotes the solid angle.

and additional corrections for sample absorption according to Lambert-Beer's law for a well-defined sample thickness  $d$  are needed if absolute scattering intensities are of concern. To obtain model equations for more complex many-atom systems, one needs to consider the spherical waves arising from the scattering at each scattering center  $N$  and how they interact with each other. One subsequently obtains the molecular form factor amplitude as follows:

$$F^{\text{mol}}(\vec{q}) = \sum_{i=1}^N F_i^{\text{atom}} \exp^{i\Delta\phi} \quad (4.4)$$

Further abstractions of a similar kind can be made for more complex scatterers such as e.g., particles, monomers of a polymer chain or clusters of chains. For given geometries, a variety of form factors have been derived in literature, e.g. for spheres, cylinders, etc. A special case for hard spheres will be discussed in the next sections. In the following, a rough introduction to the modeling of particulate and non-particulate systems will be given, following mainly the books of Roe et al. and Strobl [130, 131].

#### 4.1.1 Modelling of particulate systems

As described in the previous section, the observed scattering intensity  $I(q)$  of a complex material depends both on the structure of a single repetition unit (which can be an atom, a molecule, a monomer, or even clusters of chains) and on the arrangement of the constituents in space (size, distance, composition). The former is represented by the aforementioned form factor, while the latter is called the *Structure Factor* or *Interference Function*, as the underlying mechanism of its functional form can be described by scattering interference of the respective constituents. The overall scattering intensity is therefore commonly written as a product of the isotropic form factor intensity  $P(q)$  - the mean-square average over all orientations of  $F(q)$  - and the structure factor  $S(q)$ .

$$I(q) \propto P(q) \cdot S(q) \quad (4.5)$$

For a given continuous system of scattering constituents with number density  $n_0$ , Zernike and Prins showed [132] that the structure factor can be written in dependence of the radial distribution function  $g(r)$  of these substructures, which describes the probability distribution function to find a second entity of the same type at a given distance  $r$ .

$$S(q) = 1 + n_0 \int_0^\infty 4\pi r^2 g(r) \frac{\sin(qr)}{qr} dr \quad (4.6)$$

The advantage of this equation lies in the reduction of a complex many-body scattering expression to an equation that yields explicit results of  $S(q)$  based on a certain model of distribution  $g(r)$  of scattering entities, which in the case of simple periodic systems can even yield analytical results, while also allowing for any degree of simplification or specification by changing  $g(r)$  to more simple or complex model functions. However, a peculiarity of that equation lies in the fact that both the density of the scatterers  $n_0$ , as well as  $g(r)$  depend on the volume fraction  $\phi$  of the scattering moieties, transforming this rather innocently-looking equation into an integral equation that does not yield a specific solution without having a model of  $g(r)$  (a so-called *closure*) that provides an explicit dependence in the form of  $g(r, \phi)$ , while still satisfying physical motivation. In recent decades, many closures have been shown to provide rather accurate information for certain systems. A more detailed discussion of a certain closure used for a solution of hard spheres is discussed later in subsection 4.2.2. In the special case of dilute particulate systems ( $n_0 \rightarrow 0$ ), the structure factor can be approximated by unity. However, with an increasing fraction of scattering moieties, the increasing influence of  $g(r)$  (reflecting, for example, spatial arrangement) will be visible in the total scattering intensity  $I(q)$ .

#### 4.1.2 Modelling of non-particulate (continuous) systems

For non-particulate systems, one does not consider both form factor and structure factor as separate parts of the scattering intensity, but rather a continuous system of scattering entities with no inherent distinction from each other (same form factor for each sub unit). However, even in these systems, a scattering contribution can be found, as explained, e.g. [129] due to fluctuations of its scattering density  $\rho(r)$  (in real space) that occur within the sample. These fluctuations are commonly characterized by a real-space autocorrelation function  $\gamma(r)$ . Then, we can find the scattering intensity in the q-space by using the following expression analogous to the structure factor described in eq. 4.6, where  $\langle \eta^2 \rangle$  is a measure of the fluctuation of the mean square density, and  $V$  is the volume probed:

$$I(q) = 4\pi V \langle \eta^2 \rangle \int r^2 \gamma(r) \frac{\sin qr}{qr} dr \quad (4.7)$$

While the general form of the given equation 4.7 is universally applicable (compare eq. 4.6), it should be noted that eq. 4.7 refers to the overall observed scattering intensity  $I(q)$ , while 4.6 is only the general formulation for the structure factor. This treatment is consistent in so far that the modeling of non-particulate systems can be treated as a special case of particulate systems with a uniform scattering length density  $\rho(\vec{r})$  and therefore q-independent form factor intensity  $P$ .

The important behavior of non-particulate systems towards small scattering vectors (small  $q$ ) is commonly described by a power law (also called *Porod's Law* [133]), which will be sketched out briefly (following the derivation presented e.g., in ref. [131] and [130]). For its derivation, we consider an ideal two-phase system, which implies that both regions are well defined with sharp borders, while being irregularly mixed on larger length scales (= no long-range order). Therefore, the system is fully characterized by knowing only the respective volume fractions  $\phi_{1/2}$  and the ratio between the interface and the volume  $S/V$ ,

which will be shown to be obtainable from Porod's law. The scattering length density  $\rho(\vec{r})$  within the phases is assumed to be constant ( $= \rho_1$  and  $\rho_2$  respectively); therefore, any contribution from the individual scattering subunits is neglected. Using geometric arguments not covered here (see ref. [130] and the appendix of ref. [131]), it can be shown that the periodic electron density correlation function  $\Gamma(r)$  - which describes the electron density fluctuation with respect to the mean electron density - can be approximated by the initial decrease of its first oscillation (for large  $r$ ), which is assumed to be a decreasing linear function and reads:

$$\Gamma(r) = \begin{cases} V\langle\eta^2\rangle\left(1 - \frac{r}{l_{\text{por}}}\right) & \text{for } 0 \leq r \leq l_{\text{por}} \\ 0 & \text{otherwise} \end{cases} \quad (4.8)$$

Here,  $l_{\text{por}} = 4V\langle\eta^2\rangle S^{-1}(\Delta\rho)^{-2}$  is used as an abbreviation, following the definitions of the variables used above. As the Fourier transform (FT) of the linearly decaying  $\Gamma(r)$  does not exist within the standard Lebesgue integral framework, it is approximated by an exponential function (in the limit of  $r \rightarrow \infty$ ) of the form  $\Gamma(r) = V\langle\eta^2\rangle \exp(-r/l_p)$ , whose FT is a Lorentzian. Again, by considering the aforementioned limit (now as  $q \rightarrow 0$  after FT) and  $q > 0$  (effectively reducing the Lorentzian to a single power-law decay), this leads to the final version of Porod's Law, that takes the following functional form (prefactors neglected):

$$I(q) \propto \frac{1}{\phi_1\phi_2} \frac{S}{V} \frac{1}{q^4} \quad (4.9)$$

Significant deviations from this equation commonly occur due to a number of different reasons that justify a violation of the "ideal two-phase system" condition. One of the most common issues is that the surface/volume ratio  $S/V$  is only defined in terms of a fractal dimension, which leads to an alternative version of Porod's law, where  $I(q) \propto q^{-(6-d)}$ , where  $d$  is the fractal surface dimension [134]. For regular surfaces ( $d = 2$ ) this reduces to the usual dependence  $q^{-4}$ .

## 4.2 SAXS as a Tool for Polymer Network Characterization

SAXS is capable of detecting scattering density fluctuations on length scales of 1 – 60 nm, which - in terms of the structure of the polymer network - covers the realm where spatial concentration fluctuations and its consequences are visible. More specifically, this includes fluctuations arising from chemical or physical chain associations (e.g., the network correlation length  $\xi_c \sim 1 - 10$  nm), as well as moieties arising from undesired concentration fluctuations (e.g., as a result of network defects and mesoscopic crosslinking inhomogeneities  $\sim 10 - 100$  nm). Due to limitations in the range of scattering vectors accessed by SAXS, only the thermal concentration fluctuations are in the regime that can be described quantitatively. While in most cases the large-scale inhomogeneities need to be modelled by a suitable function, the relevant regime is usually not fully accessed, rendering obtained values qualitative. Below, models and challenges for a homogeneous polymer network and a more complex network with clusters emerging from microphase separation are discussed.

### 4.2.1 Homogeneous polymer networks: correlation blob size

For now, we consider a polymer network that is regularly crosslinked with roughly equal solubility for each involved precursor and a comparable scattering contrast density. While the latter assumption is true for most polymer networks, it can be strongly violated in e.g. metal-organic frameworks (MOFs), where a significant amount of clustered heavy atoms is found, leading to a strong increase in scattering contrast. But in most cases, this resembles the situation discussed in section 4.1.2, where no specific contrast within the network is found. Scattering contrast will arise only when a significant difference in scattering density between the polymer and solvent is present. Once this is found, we can distinguish between scattering responses from the low  $q$  region and the high  $q$  region. In the high- $q$  region ( $\sim 1 - 10$  nm) we find scattering arising from thermal osmotic concentration fluctuations [57, 88] that yield information on relevant length scales of correlation  $\xi_c$  of the system [75, 135]. Although originally described for polymer solutions where the graphical picture of a length scale of thermal osmotic concentration fluctuations is valid, it was found [22, 136–139] that the same model is also valid for crosslinked polymer networks to some extent.

$$I(q) = \frac{I_0}{[1 + (q\xi)^2]^{1/(2\nu)}} \quad (4.10)$$

It should be noted, that in cases of small polymer concentrations, a significant portion of that function is usually found at  $q \sim 10^{-2} A^{-1}$  making it very difficult to achieve a proper fit using only SAXS. In many of the aforementioned works in this section, SANS was used to access the relevant length scales. However, for polymer networks with relatively low molecular weights between crosslinks (e.g.,  $\leq 5$  kDa per star) and/or higher relative concentrations upon synthesis (e.g.,  $\geq 2$  c \*), there is a realistic chance of at least qualitative estimates using SAXS.

As mentioned above, the scattering contribution arising from large-scale frozen inhomogeneities dominating the behavior towards small  $q$  is commonly not fully accessed by SAXS. However, its modeling is essential for a successful regression due to the predominant intensity contribution. Due to its inaccessibility, this work will limit itself with a simple characterization using functions with minimal parameters that are still physically motivated such as Porod’s Law (see above) or a functional form suggested by Debye and Bueche [140] that describes the scattering behavior of an inhomogeneous solid with a smooth interface by usage of a real-space correlation function. This function is assumed to be of a simple exponential form  $\gamma(r) \propto \exp(-r/\Xi)$  that describes the loss of scattering signal due to inhomogeneities of a length scale  $\Xi$ . Using eq. 4.6, the functional form in reciprocal space is the following:

$$I_{DB}(q) = \frac{1}{(1 + (q\Xi)^2)^2} \quad (4.11)$$

Using that, the large-scale concentration fluctuations of homogeneous polymer networks can be qualitatively described with limitations arising predominantly from a non-sufficient access to very low  $q$  values.

## 4.2.2 Phase-separated polymer networks: domain length scales

### Bicontinuous microphase separation (Teubner-Strey)

One of the most famous models for the modeling of scattering peaks exhibited by phase separation in polymeric soft matter was proposed by Teubner and Strey [72] in order to explain the origin of a broad scattering peak found in microemulsions of water and oil. At its core, this derivation is based on a Landau expansion of the free energy of interaction in a partially immiscible two-component system, parametrized by an order parameter, which in the end yields a functional form  $I(q)$  that can be used to model the scattering intensity as follows:

$$I(q) = \frac{1}{a_2 + c_1 q^2 + c_2 q^4} \quad (4.12)$$

Here,  $a_2$ ,  $c_1$  and  $c_2$  are arbitrary coefficients without a direct physical meaning that arise from the aforementioned expansion of the Landau free energy. The corresponding correlation function  $g(r)$  takes a shape somewhat similar to the Debye-Bueche model [140] for random two-phase morphologies and describes a similar loss of long-range correlation on a length scale of  $\xi_{TS}$ . The peak in the scattering intensity arises from an additional contribution to the correlation function which is assumed to reflect the phase-separated microphases (which appear at a periodic distance  $d$ ), which are hereby modeled using a sine function with periodicity of  $d/2\pi r$ .

$$\gamma(r) = \exp\left(-\frac{r}{\xi_{TS}}\right) \sin\left(\frac{2\pi r}{d}\right) \quad (4.13)$$

A relationship of the arbitrary modelling parameters of eq. 4.12 and the physically motivated parameters of eq. 4.13 can be found by the Fourier transformation of the correlation function (yielding  $I(q)$ ). A subsequent comparison of parameters and usage of eq. 4.6 yields the following equations for the periodicity  $d$  and the domain decay length  $\xi_{TS}$  of the investigated morphology:

$$d = 2\pi \left[ \frac{1}{2} \left( \frac{a_2}{c_2} \right)^{1/2} - \frac{1}{4} \frac{c_1}{c_2} \right]^{-1/2} \quad (4.14)$$

$$\xi_{TS} = 2\pi \left[ \frac{1}{2} \left( \frac{a_2}{c_2} \right)^{1/2} + \frac{1}{4} \frac{c_1}{c_2} \right]^{-1/2} \quad (4.15)$$

It should be noted, that the actual assessment of the length scales as done in e.g., ref. [141] should be carried out with care, as the definition of both  $d$  and  $\xi_{TS}$  takes place in terms of correlation length scales, rendering the mappings of these values onto real space structures only qualitative. Although empirical arguments for the quantitative nature of  $d$  can be found, for example, by comparisons of the extracted value with values obtained from visual inspection using the simple relation  $d = 2\pi/q$ , the domain decay length  $\xi_{TS}$ , being merely defined as the characteristic value of a decaying exponential function (see eq. 4.13), should be used with care in quantitative evaluations. As a last remark, it is found that for the limit of very large separation of small scatterers ( $d \gg \xi_{TS}$ ), the correlation function  $\gamma(r)$  converges to the functional form used by Debye and Bueche (see eq. 4.11).

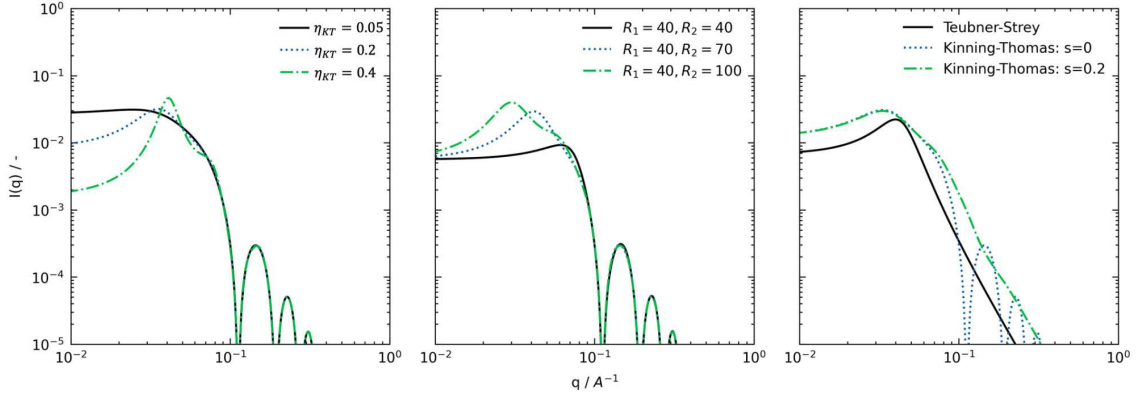


Figure 4.2: Comparison of the (pure) emerging signal  $I(q)$  from the hard-sphere model of Kinning and Thomas in comparison to the Teubner-Strey model. Shown is a variation of the hard-sphere volume fraction  $\eta_{KT}$  (left), a variation of the effective ratio  $R_1 : R_2$  (middle) and a comparison of the Teubner-Strey model and the Kinning-Thomas model (with and without lognormal distribution of size  $s$  with 'physically' matched parameters such that  $\xi_{TS}, d_{TS}$  are equivalent counterparts of  $R_1, R_2$ ).

### Particulate Hard-Sphere Model (Kinning-Thomas)

The Kinning and Thomas model [142] was originally derived for the case of diblock copolymers containing spherical domains. The purpose was to connect the form factor scattering arising from the spherical shape of these domains with the particular interference contribution of their arrangement at higher concentrations, where the simplification  $S(q) \rightarrow 1$  is not valid. In the following paragraph, a short summary of the mathematical and physical construction of this model from eq. 4.5 is given.

For the form factor  $P(q)$  of the spherical domains, one assumes a homogeneous radius sphere  $R_1$ , which immediately leads to an analytical expression in dependence on the volume of the sphere  $v_0$  and the scattering contrast  $\rho_0$  between the sphere and the matrix.

$$P(q) = 9\rho_0^2 v_0^2 (qR_1)^{-6} [\sin(qR_1) - (qR_1) \cos(qR_1)]^2 \quad (4.16)$$

Using the integral equation 4.6 in conjunction with an assumption for the correlation function  $g(r)$  that explicitly assumes the dependence on the particle volume fraction  $\phi$  (known as *Percus-Yervick closure* [143], validated by Wertheim [144] and Thiele [145]), one can now solve the integral equation for the case of hard spheres with an effective radius  $R_2$  and sphere volume fraction  $\eta$ :

$$S(q, R_2, \eta) = \frac{1}{1 + 24\eta(G(A)/A)} \quad (4.17)$$

where  $A = 2qR_2$  and  $G(A)$  is:

$$\begin{aligned} G(A) &= \frac{\alpha}{A^2} (\sin(A) - A \cos(A)) + \dots \\ &\frac{\beta}{A^3} (2A \sin(A) + (2 - A^2) \cos(A) - 2) + \dots \\ &\frac{\gamma}{A^5} (-A^4 \cos(A) + 4[(3A^2 - 6) \cos(A) + (A^3 - 6A) \sin(A) + 6]) \end{aligned} \quad (4.18)$$

Here, the following abbreviations were used:

$$\alpha = (1 + 2\eta)^2 / (1 - \eta)^4 \quad (4.19)$$

$$\beta = -6\eta(1 + \eta/2)^2 / (1 - \eta)^4 \quad (4.20)$$

$$\gamma = 0.5\eta(1 + 2\eta)^2 / (1 - \eta)^4 \quad (4.21)$$

Common applications for the Kinning-Thomas model include block copolymers with aggregation or micelle formation of a small non-miscible additive [146, 147] or in the case of micelle formation due to aggregation of functional groups in polymer matrices [8, 148–150].

# Chapter 5

## Samples and experimental setup

### 5.1 Samples

#### 5.1.1 Benzoxazinone-based tetra-star networks

##### Amphiphilic tPEG-tPCL networks

Functionalized precursors as a basis for tPEG-tPCL networks with a benzoxazinone-based crosslinking agent were synthesized by Carolin Bunk <sup>i</sup> with chemical details published in [47]. The tPEG precursors ( $M_w = 10$  kDa) were end-functionalized with an amino group, whereas the tetra-arm star poly( $\epsilon$ -caprolactone) (tPCL) precursors ( $M_w = 11$  kDa) were end-functionalized with a 2-(4-Nitrophenyl)-benzoxazinone group, resulting in the possibility of a hetero-complementary click reaction between the stars, whereas traditional end-linking processes between stars of the same type are prevented. Subsequently, Carolin Bunk prepared amphiphilic polymer co-networks (ACPNs) by mixing stoichiometric ratios of precursor solutions in different common good solvents ( $d_8$ -Toluene,  $d_4$ -THF,  $d_1$ -Chloroform) at a variety of temperatures ( $T = 25, 40, 60, 80$  °C) at different preparation concentrations between  $c = 0.5 - 7 c^*$  (with  $c^* = 70$  gL<sup>-1</sup>) over a reaction time period of approximately 4 days per sample. Later in the research process, the click reaction was carried out, exclusively using  $d_8$ -toluene as the solvent and maintaining a constant reaction temperature of  $T = 50$  °C for all prepared networks. This was done by myself, following the steps of the initial work done by Carolin Bunk.

However, networks under selective solvent conditions were prepared in a common good solvent and then fully dried using a vacuum oven ( $T = 50 - 70$  °C,  $p = 20 - 30$  mBar) at least once. Samples for diffusion measurements in particular were additionally washed several times in excess solvent before drying in order to remove sol. Subsequently, the samples were swollen in D<sub>2</sub>O for at least 24 h to equilibrium with measured degrees of equilibrium swelling degrees of  $Q = 4 \pm 0.5$ .

---

<sup>i</sup>Carolin Bunk, Leibniz-Institut für Polymerforschung Dresden e. V., Hohe Str. 6, 01069 Dresden, (Germany)



## Conventional tPEG-tPEG networks

The tetra-arm star poly(ethylene glycol) stars were end-functionalized by Carolin Bunk (see ref. [47] for details) with a 2-(4-Nitrophenyl)-benzoxazinone group ( $M_{w,star} = 11, \text{kDa}$ ), thus enabling the possibility of preparing complementary non-amphiphilic co-networks using the same amino-terminated PEG stars in conjunction with the aforementioned strategy. All chemical preparation steps are kept equal to those described above.

## Block-star tPEG-b-PCL networks

Analogously to the ACPNs described above, Carolin Bunk prepared and provided a set of tPEG-b-PCL networks. The networks were synthesized in  $d_6$ -DMSO at different temperatures by heterocomplementary end-linking reaction of pre-structured amphiphilic 2-(4-nitrophenyl)-benzoxazinone- and amino-terminated tetra-arm poly(ethylene glycol)-*block*-poly( $\epsilon$ -caprolactone) (tPEG-*b*-PCL) star block copolymers with a molar mass of  $M_n \approx 10 \text{ kg mol}^{-1}$  and a dispersity of  $D = 1.04$ . Synthetic details and procedures are described in detail in [151]. Networks of this type were investigated at different preparation concentrations, enabling a comparison with the tPEG-tPCL ACPNs in terms of the influence of star architecture and mixing inhomogeneities.

### 5.1.2 Self-reactive tPEG-SH hydrogels

A set of disulfide-crosslinked tPEG hydrogels was prepared by Zhao Meng<sup>ii</sup> using commercially available tetra-poly(ethylene glycol)-SH (Laysan Bio.,  $M_w = 10, \text{kDa}$ ) as described in ref. [71] in more detail. The precursor solutions at the desired concentrations were mixed in a  $D_2O$  phosphate buffer (pH= 7.4), and the networks were formed by facilitating the crosslinking reaction at room temperature by adding an oxidation agent (0.2, vol.%  $H_2O_2$ ). The concentrations of the precursor solutions ranged from  $c = 0.5$  to  $3.5c^*$  with  $c = 60 \text{ gL}^{-1}$ .

### 5.1.3 Metallo-supramolecular hydrogels

#### tPEG-TPy networks with varied functionality

The tPEG-TPy networks described here with varied end functionality (4-arm tPEG and 8-arm tPEG) were synthesized by Paola Nicolella<sup>iii</sup> with chemical details published in ref. [30]. In summary, TPy (terpyridine) functionalized tPEG precursors with a different number of arms and degree of end functionalization  $F_{end}$  (4 arms: [ $M_{w,star} = 20 \text{ kDa}$ ,  $M_{w,arm} = 5 \text{ kDa}$ ,  $F_{end} = 95 \%$ ] and 8 arms: [ $M_{w,star} = 40 \text{ kDa}$ ,  $M_{w,arm} = 5 \text{ kDa}$ ,  $F_{end} = 90 \%$ ]) were synthesized and mixed in different ratios (0:100, 20:80, 50:50, 80:20, 100:0) in  $D_2O$  at  $c = 35 \text{ gL}^{-1} \approx c^*$  in order to obtain transiently end-linked tPEG networks with different fractions of a star with higher functionality compared to the classical *Sakai gel*

<sup>ii</sup>Zhao Meng, Ecole Polytechnique Fédérale de Lausanne (EPFL) Institut des Matériaux, Laboratoire des Polymères, STI - IMX - LP MXD 133 (Batiment MXD), Station 12CH-1015 Lausanne (Switzerland)

<sup>iii</sup>Paola Nicolella, Johannes Gutenberg-Universität Mainz, Department of Chemistry, Duesbergweg 10-14, D-55128 Mainz, (Germany)

[21]. The precursor solutions were rigorously mixed in a vial before the addition of the ion in order to minimize freezing in the mixing inhomogeneities.

### **tPEG-TPy/Phen networks at different self-sorting regimes**

The tPEG-based networks described here were synthesized by Mostafa Ahmadi <sup>iv</sup> with chemical details provided in ref. [152] and references therein. Tetra-arm OH-terminated PEG precursors ( $M_w = 20$  kDa, PD= 1.03) were end-functionalized with two kinds of end functionalization, being Phenantroline (Phen) and Terpyridine (TPy) respectively (see Figure 6.26). Networks are formed from homoleptic and heteroleptic crosslinking at a preparation concentration of  $c = 40 \text{ gL}^{-1} \approx c^*$  upon excess exposure (ligand to ion ratio 1:2) to suitable ions ( $\text{Cu}^+$ ,  $\text{Co}^{2+}$  and  $\text{Fe}^{2+}$ ) to a stoichiometric mixture of tPEG-Phen / tPEG-Phen, as well as tPEG-Phen / tPEG-TPy precursors. Due to the differences in the preferred coordination geometry of the ions and sterical hindrance induced from the crosslinker, subsequent differences in the network structure are expected.

### **tPEG-linPEG-TPy dual-network hydrogels**

The tPEG-linPEG-based networks described here were synthesized by Mostafa Ahmadi <sup>iv</sup> with chemical details published in ref. [55]. Linear PEG precursor ( $M_w = 6$  kDa) were functionalized with terpyridine (TPy) and N-hydroxy succinimide (NHS) ester functionalities at both ends. Tetra-arm PEGs ( $M_w = 10$  kDa) were functionalized with an amine group at each arm. The networks were then prepared in a  $\text{D}_2\text{O}$  phosphate buffer at a concentration of  $c = 100 \text{ gL}^{-1}$  (being a little higher than the overlap concentration for pure 10 kDa tPEG precursors) and then a second set of physical crosslinks is introduced by adding different ions. A set of 4 samples was prepared with a stoichiometric addition of a different ion per sample,  $\text{Mn}^{2+}$ ,  $\text{Zn}^{2+}$ ,  $\text{Co}^{2+}$  and  $\text{Ni}^{2+}$  respectively.

## **5.2 Experimental setup**

### **5.2.1 Low-field $^1\text{H}$ -NMR**

All low-field MQ NMR measurements in this work were performed on a Bruker mq20 device operating at a Larmor frequency of 20 MHz (resulting in  $B_0 = 0.47$  T). Pulse lengths used are in the range of  $1.5 - 3 \mu\text{s}$  for  $p90$  and  $3.0 - 5 \mu\text{s}$  for  $p180$  with significant ranges being caused by the usage of different devices and radio frequency pulse-generating hardware. The temperature of the investigated sample was controlled by Bruker BVT-3000 temperature unit controllers yielding an accuracy of  $\pm 1.0$  K. Most samples in this thesis were investigated using 1.5 mL Agilent vials with a PTFE-insulated screw top, enabling the use of volatile and aggressive solvents as swelling agents (such as *d*-THF) while still controlling the degree of swelling, which would not be possible by using standard 10 mm x 200 mm glass tubes with a huge free volume.

---

<sup>iv</sup>Mostafa Ahmadi, Johannes Gutenberg-Universität Mainz, Department of Chemistry, Duesbergweg 10-14, D-55128 Mainz, (Germany)

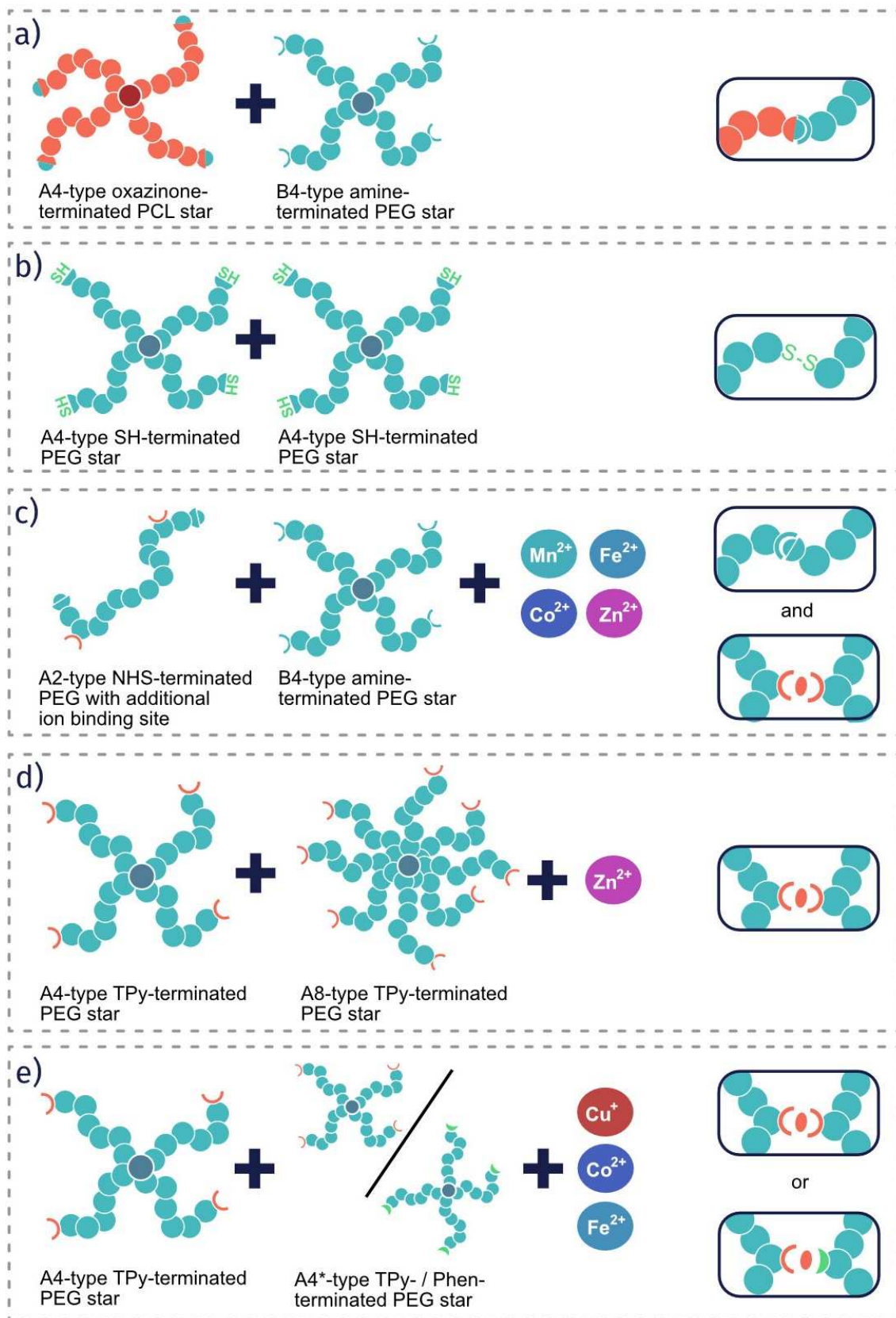


Figure 5.1: Graphical (simplified) overview over all the different star precursors and coupling reactions described in this chapter.

### 5.2.2 High-field $^1\text{H}$ -NMR

$^1\text{H}$  MAS NMR spectra and double-quantum magic-angle spinning NMR experiments were carried out on a Bruker Avance III 400 MHz spectrometer with a 4mm triple-resonance MAS probe at a spinning frequency of  $\nu_{rot} = 5 \pm 0.02$  kHz. As the high frequency spinning of elastic gel pieces results in an unstable rotor spinning frequency (and therefore poses a danger to the equipment), a technique was developed to minimize this effect. A small, round 4 mm x 0.2 mm slice of a swollen polymer network was cut out of the network and tightly packed into a rotor, surrounded by manufactured PTFE cylinders with a tight fit. This results in significant stabilization of the rotor, reducing the spinning instabilities from several hundred Hz to about 20 Hz. A Bruker BVT 3000 was used to keep the temperature stable at  $T = 30 \pm 1^\circ\text{C}$ . As a chemical shift reference for all networks investigated, the values obtained in ref. [47] were used. POST-C7 experiments were carried out using pulse lengths (power) of  $p_{90} = 2.5 - 3\mu\text{s}$  (39 W) and  $p_7 = 3\mu\text{s}$  (6.8 W) respectively, such that the necessary condition of  $\omega_{nut} = 7\nu_{rot}$  is met.

### 5.2.3 PFG-NMR

Measurements of translational diffusion coefficients were conducted on a Bruker Avance II spectrometer with a proton  $^1\text{H}$  resonance frequency of 400 MHz which is used together with a Diff60 probe head. All measurements were performed at a temperature of  $30^\circ\text{C} \pm 1^\circ\text{C}$ . Solutions of probe molecules were studied using a 4mm PTFE gastight rotor insert to avoid solvent evaporation. For convenience in sample handling of the swollen gels, but also to minimize convection effects during longer diffusion times, the investigated pieces of swollen gel were filled into a standard 4mm MAS rotor with a rubber sealing ring. This prevents the evaporation of solvent (which for toluene is relevant even at  $T = 30^\circ\text{C}$ ). Test measurements of a  $\text{D}_2\text{O}/\text{H}_2\text{O}$  mixture with a varied diffusion time  $\Delta$  between 20 and 200 ms revealed no systematic change in diffusion coefficient, confirming that convection effects are successfully minimized.

### 5.2.4 Viscosimetry

Viscosity measurements were performed using a RheoSense *m*-Vroc equipped with a 20  $\mu\text{L}$  sample cell and a 500  $\mu\text{L}$  Hamilton syringe. All investigated solutions were measured at  $T = 30 \pm 0.2^\circ\text{C}$  (being regulated by an external water bath) using 4 different flow rates between 100 – 800  $\mu\text{L}/\text{min}$ , and two measurements per flow rate per sample. The final value was determined using the average of the 8 viscosity values obtained. If the standard deviation of the mean remains below the error given by the manufacturer (2.5 %), the latter number is used.

### 5.2.5 SAXS

SAXS experiments were performed using a Retro-F laboratory setup (SAXSLAB) equipped with a microfocus X-ray source and an ASTIX multilayer X-ray optics as a monochromator for  $\text{Cu K}\alpha$  radiation ( $\lambda = 0.154$  nm). Measurements were recorded in vacuum ( $p < 1$  mBar)

using a PILATUS 3 R 300K detector at two sample-to-detector distances (1 m and 3 m, respectively) to cover both the SAXS and the WAXS regime. All measurements were made at room temperature ( $\sim 20^\circ\text{C}$ ) and in transmission mode, where the transmission factor for all samples was between 20 – 50%. To conduct experiments on swollen gel pieces within the vacuum, all gels were carefully cut into small pieces ( $< 2\text{mm} \times 2\text{mm} \times 2\text{mm}$ ) using a scalpel and placed in a 2-piece screw-top hollow metal cylinder with a circular opening on both ends and a stiff PTFE O-Ring in between for ensuring a gas tight atmosphere between the two screwable parts. The circular openings in the middle were sealed with Mica plates with a thickness of 8-10  $\mu\text{m}$  (purchased at SAXSLAB). The 1 cm opening allows the beam to traverse the sample with minimal influence from the setup itself. Initial measurements of the sample holder with only Mica plates (no gel) have shown no significant contribution in the SAXS regime but only sharp and easily identifiable peaks in the WAXS regime. All 2D data sets were reduced by azimuthal averaging using *SAXSGUI* v2.19.02.

## Chapter 6

# Chain-level investigation of gels using MQ-NMR

This chapter will provide results obtained from applying the outlined MQ NMR methodology to different networks. First, a more refined method for analyzing discrete distributions of residual dipolar coupling values is presented, followed by a short empirical investigation of the influence of pulse settings on the experimental accuracy. Afterward, several types of swollen polymer networks (see Figure 5.1 for a simplified overview) will be investigated, all of which are synthesized using star-shaped precursors to obtain well-defined connectivity motif distributions within the networks. These include chemically-linked networks such as the amphiphilic oxazinone end-linked tPEG-tPCL network and the homocomplementary end-linked disulfide tPEG networks, as well as physically-crosslinked tPEG networks using a terpyridine/ion-based end-linking reaction.

### 6.1 Improvements of the Baum-Pines evaluation procedure

#### 6.1.1 Global optimization strategy

A major part of this work is concerned with the quantification of specific connectivity motifs in well-defined gels synthesized from star-shaped precursors under varying preparation conditions. An integral part of this process is the procedure developed by Lange et al. [23] (see section 3.4.2 for more details); hence it is worthwhile to explore both limitations and possible improvements. The baseline given by Lange et al. is a simultaneous fit using a *Simulated Annealing* strategy [153] for the regression of the measured data to avoid being trapped in local minima. Specific implementations (loss function, residual definition, and estimation of errors) are not specified further in the given work. Therefore, this chapter aims to provide a clearly outlined strategy for answering the following problems.

(1) In ref. [23], no specifications regarding the simultaneous fit itself were given. Typically, these fits are most easily approached by constructing a loss function (or residual function) that is a sum of the individual functions as  $L(\tau_{DQ}) = L_{\Sigma MQ}(\tau_{DQ}) + L_{DQ}(\tau_{DQ})$ . However, as can be seen, for example, in Figure 6.1, the intensity differences in  $I_{\Sigma MQ}$  and  $I_{DQ}$  can lead to a strong underrepresentation of the residuals belonging to  $I_{DQ}$ . Here, simultaneous

regression of both  $I_{DQ}$  and  $I_{\Sigma MQ}$  is carried out by constructing a unifying loss function  $L(\tau_{DQ})$  that tries to incorporate the importance of the regression parameters (SL fraction/RDC + defect fraction > DL fraction > HOC fraction), while also incorporating the physics behind. Therefore, it is constructed so that the residuals of  $I_{DQ}$  (which "encode" the RDC values and are the most limiting factor of the SL fraction) are as significant as the residuals of  $I_{\Sigma MQ}$  despite an overall lower intensity (due to the physics behind the experiment). Therefore, a normalized loss function is used as follows to create the residual vector:

$$L(\tau_{DQ}) = \left| \frac{I_{\Sigma MQ}(\tau_{DQ}) - \hat{I}_{\Sigma MQ}(\tau_{DQ})}{\max(I_{\Sigma MQ})} \right| + \left| \frac{I_{DQ}(\tau_{DQ}) - \hat{I}_{DQ}(\tau_{DQ})}{\max(I_{DQ})} \right| \quad (6.1)$$

A construction of the loss function in that way ensures that both functions are weighted in the same manner, while keeping a respective "internal weighting" according to the point-wise intensities. Therefore, the parts of the curve where the SL fraction is encoded (usually close to the maximum of  $I_{DQ}$ ), as well as the corresponding relaxation part, are effectively weighted the most, while the diminishing intensity of the anyway poorly-defined HOC component does not influence the fit much.

While the given  $L(\tau_{DQ})$  solves the presented problem, it comes with the caveat that the tail fraction (the single exponential decay of  $I_{\Sigma MQ}$  toward long  $\tau_{DQ}$ ), which in nearly all cases is a region of high confidence, is underrepresented due to its low intensity. Therefore, the usage of this loss function comes with an additional trick: a preliminary fit of the data points clearly belonging to the tail is used to determine the tail parameters (without any further model assumption). Then, the corresponding parameters ( $a_{\text{tail}}, T_{2,\text{tail}}$ ) can be initialized with the preliminary values and restricted so that only small variations (e.g., 10%) of the initial parameters are allowed.

(2) The Simulated Annealing algorithm used in ref. [23] is a powerful tool for increasing the chance of not being trapped in a local minimum based on mimicking a physical process following Boltzmann statistics [153]. However, it suffers greatly from the fact that it requires an initialized system state ("starting Boltzmann statistics representing the system") and a custom temperature series to work properly. Once these are not set properly, the algorithm does not always ensure the convergence of the result towards a global minimum. As there exists no secondary method that is able to quantify chain connectivities based on their microscopic anisotropy of motion, there exists no reference system that can be used to test or validate these values and make sure that the found result is indeed the global minimum. Hence, a global optimization strategy, such as simulated annealing, which relies on delicate control parameters, has the inherent disadvantage of not being able to test whether the local minimum is indeed a global minimum. Due to this, an alternative approach was developed.

As described in section 3.4.2 and shown in Figure 3.5, the most interesting parameter is the SL fraction (parameter  $a_1$  in eq. 3.4.2) and its corresponding RDC value ( $D_{res,1}$ ). As it is also the parameter that will be among those having the greatest influence on the overall shape of the fit, a partial brute-force procedure was implemented [154] to ensure a global minimum for the given parameter. Empirically, it was found that fixing  $a_1$  already

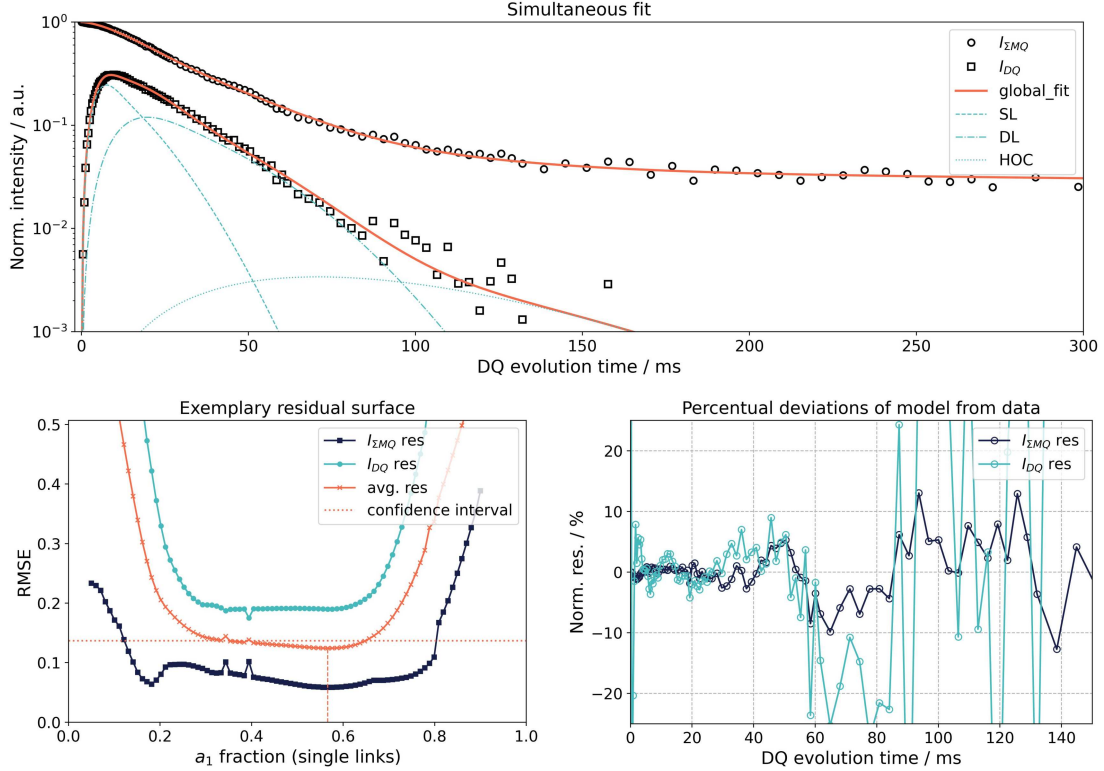


Figure 6.1: Exemplary evaluation according to section 6.1.1 on a tPEG-SH sample at  $c_{\text{prep}} = 2.5 c^*$ . Top: measured data and multi-component fitting procedure. Bottom: Residual surface for the  $a_1$ -variation, as well as the normalized percentual deviation of the regression model from the data for both curves.

strongly reduces the overall uncertainty of the fit and reduces the number of local minima. Therefore, the parameter  $a_1$  was fixed and varied within a given range  $[a_{\min}, a_{\max}] \subset (0, 1)$  with a step size of  $\Delta a_1 = 0.01$ . For each  $a_{1,i}$ , both the individual residuals according to the paragraph above, as well as their average (which is proportional to the sum, but more practical in terms of automated visualization) are analyzed, and the minimum of the average residual is extracted. In addition, a second looping procedure (characterized by a repetition number  $n_r$ ) with a set of random starting parameters (excluding the tail fraction as explained above) is performed. It repeats the same procedure and replaces the values once the obtained residual is smaller. This reduced the bias effect of the starting parameters chosen (see the final exemplary result in Figure 6.1). Although this method is computationally expensive (about 10 min run time on a single core), it is a safe method of obtaining a realistic estimate for the SL fraction.

So far, no reliable procedure has been found to estimate the error of the parameters obtained from the fit. It is evident that the parameter standard deviations from the procedure itself are of no use, as these commonly (strongly) underestimate the actual uncertainties in non-linear multi-component fitting procedures [155]. Using the  $a_1$ -variation approach from above, information is obtained about the residual surface of  $a_1$ . An empirical estimate of the uncertainties of the extracted parameters is found by visual inspection of the fit result for systematic variations of  $a_1$  away from the minimum. It can be immediately seen



from the residual surface that there exists usually a broad plateau in which no distinction can be made, as in many cases the minima for both residual functions are not perfectly overlapping. Regression boundaries are then estimated by tracking the visual difference of the model and data, yielding an empirical value of about 10% deviation in the residual that would correspond to a model fit that can be visually categorized as not sufficient. However, the specific value should be estimated on a per-sample or per-sample series basis. While this is still not optimal, other statistical measures cannot be applied, as it can neither be ensured that the distribution function of the residuals is a Gaussian, which is the most common assumption for statistical measures, nor is the fit linear or/and unrestricted (simplifying the treatment).

### 6.1.2 Pulse length offset influence

As is evident, the Baum-Pines sequence will need properly calibrated pulses such that theoretical assumptions are met, and signal curves without distortions or systematic bias can be obtained. However, during the course of this work, it was observed many times that the calibration experiment (a "nutaton curve") run on the Bruker mq20 machine to estimate the pulse lengths of the  $90^\circ$  and  $180^\circ$  pulses shows a flat maximum. This limits the accuracy of the estimation of the  $90^\circ$  pulse to approximately  $\pm 0.1 - 0.2 \mu\text{s}$ . So far, no publication has been found that investigates the implication of this limitation and the resulting uncertainty arising from the experiment itself. Therefore, a slice of natural rubber of approximately 1mm thickness was taken and heated to  $T = 80^\circ\text{C}$  to fulfill the requirement of being in the rubbery plateau regime as explained in section 3.3. An initial visual inspection of the FID ensured that there is no initial Gaussian-like behavior of the signal (corresponding to a glassy component [156]).

The corresponding nutation experiment revealed an optimal set of pulse durations of  $p_{90} = 1.65 \pm 0.15 \mu\text{s}$  and  $p_{180} = 3.45 \pm 0.05 \mu\text{s}$ , which results in an MQ NMR data set that can be well reproduced with a single component and defect fraction according to eq. 3.4.2 even with a low number of points (see Figure 6.2). The small deviation in  $I_{\text{DQ}}$  is probably due to a very small distribution of RDC values, which will be ignored, as the practical implications for this experiment are negligible.

The Baum-Pines sequence was then adjusted such that it will be nested within two loops that iterate over 14 different values for  $p_{90}$  and  $p_{180}$  centered roughly around the optimum values with a step width of about  $\Delta\tau = 0.05 \mu\text{s}$ . This results in a tight experimental mesh of 196 experiments that sample the space of possible values that are within the uncertainty given by a flat nutation curve, as well as a bit beyond this part. Due to the automated way the experiment is realized, the low number of points, and the low recycle delay of  $d_1 = 1\text{ s}$  needed for the recovery of most of the rubber signal, the whole experiment can be efficiently run within 2 days of run-time, while providing an accurate and practical way to determine the implications of a pulse offset caused by experimental limitations.

A Python script was developed such that the evaluation of the 196 experiments is carried out in an automatized fashion. As a result, one obtains a set of 14x14 matrices with the entries being the respective RDC values, tail fractions, and  $R^2$  values (as a rough measure of the goodness of fit). As can be seen in Figure 6.2, there exists a clear maximum region

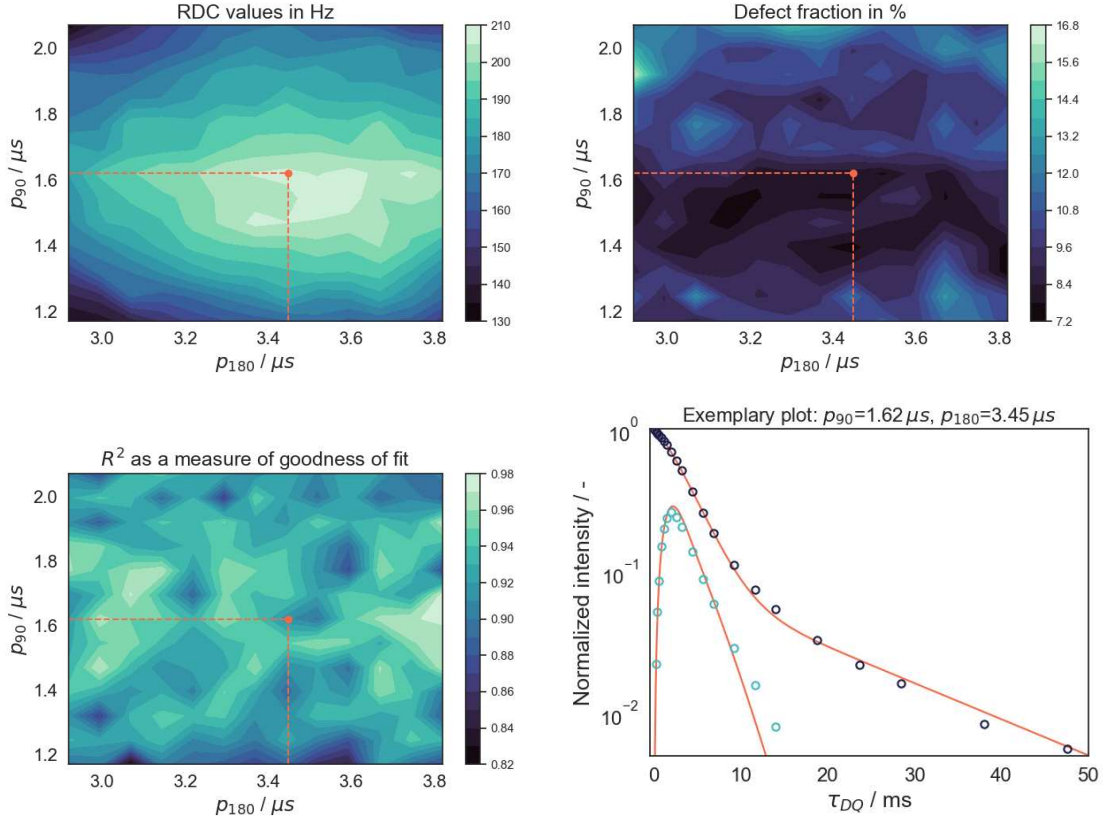


Figure 6.2: Surface visualization of the parameter obtained from the automated evaluation of the rubber experiment for different pairs of pulse lengths, as well as an exemplary fit for the supposed optimal settings. Optimal settings according to the visual inspection of the nutation curve are marked by dotted red lines in each of the surface plots.

for the RDC value with pulse deviations that result in a reduction of the observed RDC value. Within the pulse length error discussed above ( $\Delta\tau \approx 0.1 \mu\text{s}$ ), the resulting deviation in the RDC values is in the range of 5% ( $210 \pm 10 \text{ Hz}$ ) with the error mainly caused by the offset of  $p_{90}$ . The corresponding defect fraction ranges from 7.2 – 9.6% with only a rough trend visible that is overshadowed by noise. However, the range of values obtained is still very precise and is on par with the precision of commonly used methods such as sol extraction upon swelling. Lastly, inspection of the  $R^2$  surface ensures that the automated fitting procedure does not bias the results due to systematic distortions of the expected A.l.-function line shape. Within the relevant region, no systematic decrease in fit quality is observed.

## 6.2 Model tPEG-tPEG and amphiphilic tPEG-tPCL co-networks

One of the main objectives of this thesis is the microstructure investigation of amphiphilic co-networks (ACPNS) made from amino-functionalized tPEG and 2-(4-Nitrophenyl)-benzoxazinone-functionalized tPCL precursors (see Figure 6.3 for a graphical representation of the system) that mimics the famous heterocomplementary end-linked tPEG system of

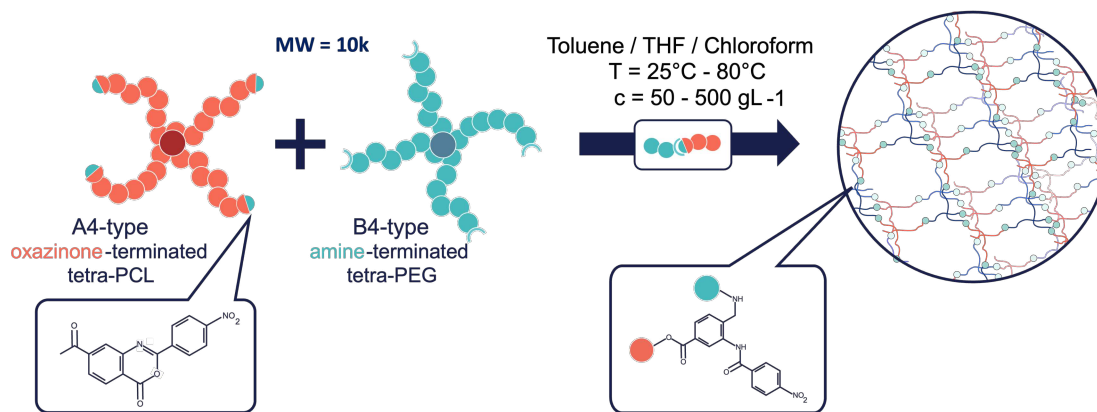


Figure 6.3: Overview of the system described in section 5.1.1. 10 kDa tPEG stars and 11 kDa PCL stars are heterocomplementary crosslinked by a benzoxazinone-based coupling agent under different temperatures, solvents and concentrations.

Sakai et al. [21]. Chemical specifications on the investigated systems are found, e.g., in ref. [47] and section 5.1.1. The gels were prepared using different preparation concentrations ( $c_{\text{prep}}$ ), temperatures before ( $T_1$ ) and after reaching the gel point ( $T_2$ ), solvents and monomer architecture (e.g., switching the tPCL precursor with a similarly functionalized tPEG precursor or using a tPCL-b-PEG block-star precursor). As will be shown, switching the coupling chemistry will produce a microstructure that is different from that of the well-known Sakai-type tPEG gels. Additionally, a peculiarity of the PEG-water system and post-curing effects are highlighted with conclusions based on the connectivity motif distribution (single links (SL), double links (DL), higher-order connectivity motifs (HOCS) and isotropic defect fraction (defs)) identified by MQ-NMR. The specific reaction conditions and the general results used are displayed in Table 6.1 (samples synthesized by Carolin Bunk and published in [47]) or presented where needed in text and figures. Generally, all samples presented here are investigated using the experimental conditions described in section 5.2 in conjunction with the Baum-Pines sequence and the evaluation procedure discussed in section 3.4.2 and at regulated temperatures between  $25 - 30 \pm 1^\circ\text{C}$ . Specifications and more details can be found in reg. [47] and [151].

First, a set of three samples consisting of a resynthesized "Sakai-type" tPEG gel at  $c = 3c^*$  (details described in ref. [21]), as well as two different networks (sample references PEG1-3 and CN5-3 according to Table 6.1) synthesized using the chemistry of Bunk are measured, evaluated, and compared (see Figure 6.4). The aim of this initial comparison is to establish a baseline by comparing the connectivity motif distributions of these samples and to optimize the synthesis on the basis of the SL fraction and the number of defects. Recalling again (see section 6.1) that the error bars given in Figure 6.4 are of systematic nature, it becomes immediately evident that the networks that use oxazinone-based chemistry are worse in terms of fraction of regular single link connectivities (Sakai: 54%, PEG-1: 41% CN5-3: 35%). Although one may speculate that CN5-3 (the tPEG-tPCL network) displays a slightly lower apparent SL fraction due to small differences in the residual dipolar coupling values of the respective PEG and PCL network chains (resulting in a slight broad-

Table 6.1: This Table presents all amphiphilic PEG-PCL co-network samples investigated by MQ-NMR. <sup>d</sup> denotes samples that were dried before and reswollen to preparation condition before measurements were performed.  $f_i$  denotes the respective fraction of connectivity motifs (SL - single link, DL - double link, HOC - higher order connectivity motifs, defs - isotropic defect fraction). Solvents used for the synthesis, as well as applied temperatures pre- ( $T_1$ ) and post-gel point ( $T_2$ ) are shown in their respective columns. Sample notation follows the pattern CN*a*-*b* where *a* is the index for a certain sample set of comparable reaction conditions and *b* indicates the preparation concentration in multiples of  $c^*$ . It matches the notation as published in ref. [47]. Adapted with permission from ref. [47]. Copyright 2023 American Chemical Society.

sample	$c_{\text{prep}}/c^*$	$f_{\text{SL}}/\%$	$f_{\text{DL}}/\%$	$f_{\text{HOC}}/\%$	$f_{\text{defs}}/\%$	solvent	$T_1/^\circ\text{C}$	$T_2/^\circ\text{C}$
CN3-1 <sup>d</sup>	1	24	65	10	0.1	d <sub>4</sub> -THF	25	60
CN1-3 <sup>d</sup>	3	39	51	9	1	d <sub>4</sub> -THF	25	25
CN2-3 <sup>d</sup>	3	39	49	11	1	d <sub>4</sub> -THF	25	40
CN3-3 <sup>d</sup>	3	36	52	10	2	d <sub>4</sub> -THF	25	60
CN3-5 <sup>d</sup>	5	52	39	8	1	d <sub>4</sub> -THF	25	60
CN4-1	1	22	32	38	9	d <sub>4</sub> -THF	40	80
CN5-1	1	26	34	35	5	d <sub>4</sub> -THF	60	60
CN4-3	3	32	47	19	2	d <sub>4</sub> -THF	40	80
CN5-3	3	35	51	13	1	d <sub>4</sub> -THF	60	60
CN6-1	1	23	33	41	3	d <sub>8</sub> -toluene	40	80
CN7-1	1	26	32	39	3	d <sub>8</sub> -toluene	60	60
CN6-3	3	35	51	13	1	d <sub>8</sub> -toluene	40	80
CN7-3	3	34	50	15	1	d <sub>8</sub> -toluene	60	60
CN8-1	1	24	31	17	28	d-chloroform	40	80
CN8-3	3	38	46	15	0	d-chloroform	40	80
CN9-3	3	31	52	17	0	d-chloroform	60	60
PEG1-3	3	54	16	20	10	D <sub>2</sub> O	25	25
PEG2-3	3	41	46	12	1	d-chloroform	25	25

ening of the first maximum of the  $I_{\text{DQ}}$  curve), the difference of  $\Delta \text{SL} = 13 - 19\%$  is beyond experimental peculiarities. Compared to an older study [23], this difference is even more pronounced. Furthermore, a surprising and systematic difference is observed in the RDC values of the SL and DL connectivity motif, which is approximately a factor 2 – 3 in the average RDC value (34 Hz vs. 70 – 90 Hz) that is also reflected in the individual RDC values. Although a small portion may be attributed to the significant difference in the primary defect fraction (10% vs. 1%), the overall shift observed is attributed to conformational differences in the crosslink, which will be discussed later. As shown in ref. [47], the decrease in the overall fraction of the SL motif does not significantly influence the mechanic stability (plateau moduli) compared to the Sakai-type gel, since the higher conversion and the overall different microstructure compensate for this disadvantage. Nevertheless, further experiments will try to optimize the SL fraction, as a higher SL fraction will result in a more model-like network and the dependence of these topological changes on the reaction conditions is a topic not yet sufficiently explored.

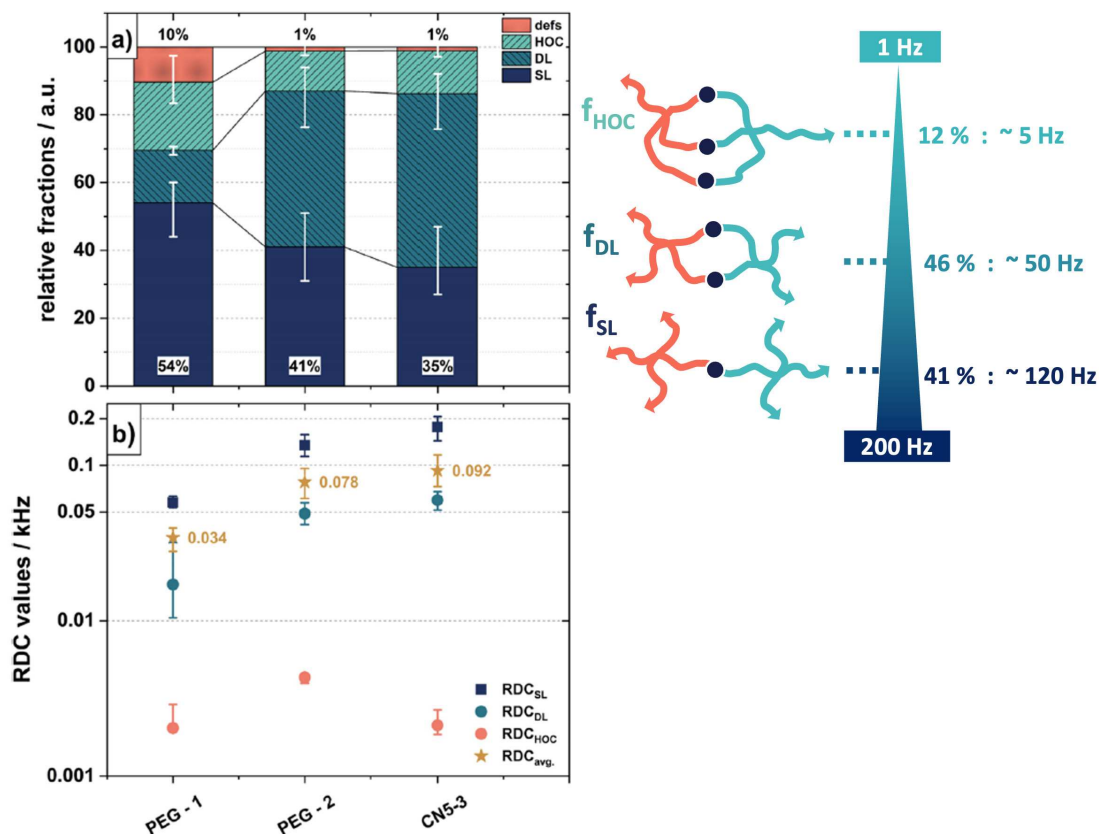


Figure 6.4: Left panel: fractions of connectivities and corresponding residual dipolar couplings for a set of three gels, being a classical 'Sakai' tPEG-tPEG gel (PEG-1), as well as a tPEG-PEG gel (PEG-2) and a tPEG-tPCL gel (CN5-3). Sample details can be found in Table 6.1. Reprinted with permission from ref. [47]. Copyright 2023 American Chemical Society. Right panel: assignment scheme used for the extraction of the parameters shown in the left panel.

### 6.2.1 Influence of reaction conditions

In a next step, the influence of the solvents used is investigated by studying the connectivity motif distribution for three different solvents ( $d_4$ -THF,  $d_8$ -toluene and  $CDCl_3$ ) each of which has a slightly different polarity. It should be noted that using  $D_2O$  for matching the synthesis conditions of Sakai et al. is not feasible (even for the tPEG-tPEG networks), as the coupling agent constituting the crosslink is not soluble in  $D_2O$ . Surprisingly, no differences were found in either the connectivity distribution or the RDC values in the three solvents used (see Figure 6.5). Although this implies that the SL fraction is below the expectations for all solvents, the gained flexibility in the choice of solvent also allows for a more in-depth characterization of our networks (applying e.g., dynamic light scattering in  $d_4$ -THF as done in ref. [47]). Furthermore, the solvent comparison also indicates that minor differences in hydrodynamic radii ( $R_{h,PEG}$  is assumed to be different from  $R_{h,PCL}$  for at least  $d_8$ -toluene) and overlap concentrations ( $c_{PEG}^* = 55.2 \text{ gL}^{-1}$  and  $c_{PCL}^* = 76.2 \text{ gL}^{-1}$  according to ref. [47] at  $T = 25^\circ\text{C}$ ) do not significantly influence the distribution of the connectivity motif obtained, which was not clear before, as both the original experiments by Lange et al. [23], as well as simulations [48] use only one type / size of precursor.

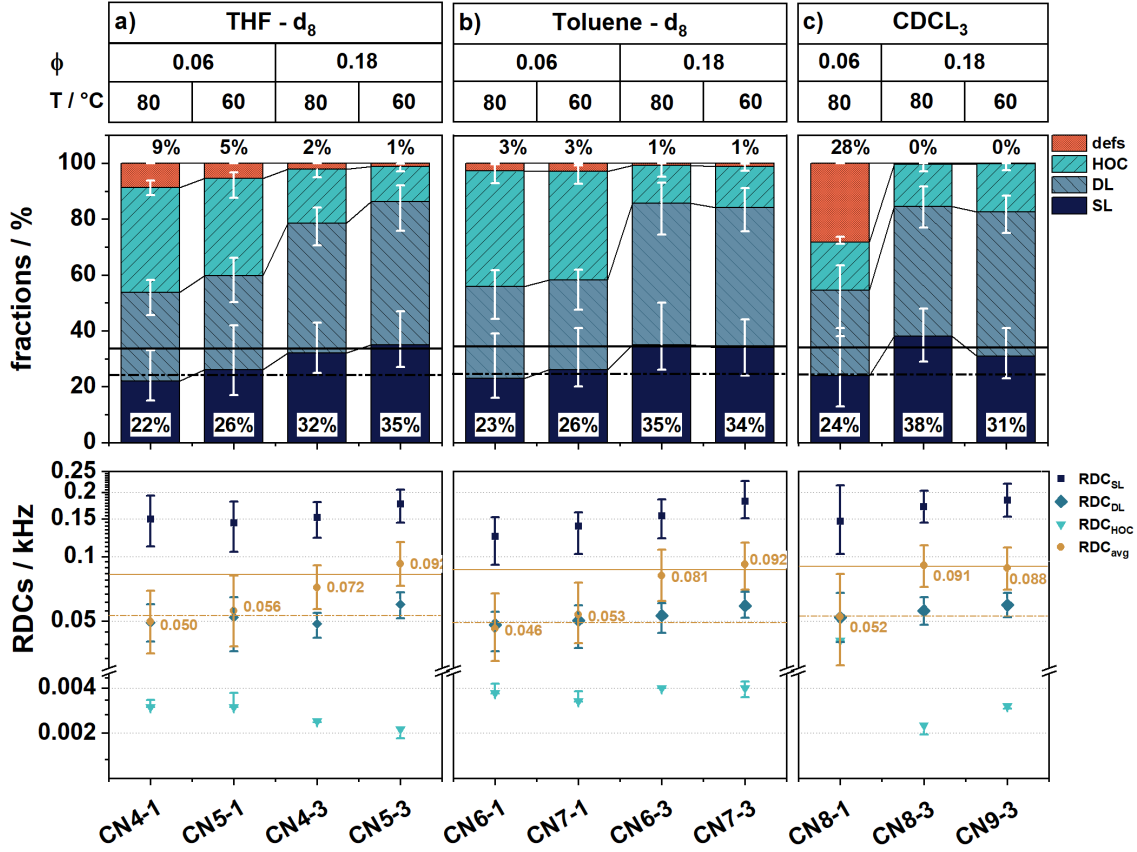


Figure 6.5: A comparison of fractions of connectivities and residual dipolar coupling values of different tPEG-tPCL gels (details found in Table 6.1) at different polymer volume fractions  $\phi$  during synthesis, temperature programs and solvents used. Reprinted with permission from ref. [47]. Copyright 2023 American Chemical Society.

To check the response of the connectivity motifs to the reaction speed (controlled by the reaction temperature), the experiments mentioned above were repeated at a different temperature, resulting in two experiments per solvent, per concentration at  $T=40^\circ\text{C}$  pre- and  $T=80^\circ\text{C}$  post- gel point, as well as  $T=60^\circ\text{C}$  for both, pre- and post-gel point. As shown in ref. [47],  $T=40^\circ\text{C}$  corresponds to a gelation time of  $t = 46$  min (determined by NMR), whereas  $T=60^\circ\text{C}$  corresponds to  $t = 36$  min. Theoretically, it is expected that the synthesis performed at a lower temperature results in gels with higher homogeneity (less defects and a higher SL fraction), as a result of the lowered reaction rate. It is expected that the lowered reaction rate allows for a relaxation of the formed network chains in comparison to the formation of new crosslinks. Practically, no differences are found (see Figure 6.5) for all temperatures and solvents, indicating that the reaction rate is already within the limit where the network relaxes faster than crosslinks are formed for both temperature protocols used, or alternatively, the lower temperature can lead to an increased difference in the  $c^*$  values, which negatively impacts homogeneity. However, since different solvents have previously been investigated and no influence of  $c^*$  mismatches was found, the former

hypothesis may be more probable.

Therefore, it can be summarized that the synthesis used is highly stable against changes in solvent, temperatures, reaction rate, and differences in  $c^*$  values, while only resulting in sub-optimal connectivity motif distributions with a lowered SL fraction. Nevertheless, all obtained networks show very little content of dangling chain ends and unreacted precursors, which still allows them to compete with the classical tPEG-gel in terms of mechanical properties and large-scale structural homogeneity (which is mostly driven by primary defects).

### 6.2.2 Solvent-dependent conformational changes in the PEG backbone

As discussed in the previous section, the investigated networks show RDC values that are unusually high (about  $\approx 110 - 150$  Hz for the SL motif at  $c = c^*$ ) in comparison to the Sakai-type tPEG gel (about  $\approx 60$  Hz for the SL motif at  $c = c^*$ ). Possible causes have previously been discussed and empirically checked only in terms of synthesis-related reasons (such as solvents used during synthesis). However, none of these could explain the observed differences so far. Therefore, it was speculated that solvent-induced intrinsic changes in the chain conformation could be a reason, such as PEG having a different conformation in polar and unpolar solvents. In fact, a set of Raman spectra of PEG in the melt, aqueous solution, as well as in an unpolar solvent (chloroform) was analyzed by Koenig et al. [157], revealing that the repeat unit of PEG in the aqueous solution is more likely to retain the typical TGT structural motif (trans-gauche-trans) found in the crystalline state. However, measurements in the molten state and diluted in an unpolar solvent seem to indicate a more disordered structure. This observation was also confirmed by simulations (see, e.g., ref. [158]) and by measuring the temperature-dependent CH-vector order parameters [159] of the ethylene glycol repetition unit in water. As it is not clear whether this could influence the RDC values of the overall backbone, a tPEG-tPEG gel was synthesized at  $c = 2c^*$  and  $T = 50^\circ\text{C}$  in  $d_8$ -Toluene. Subsequently, it was dried and split into two equal pieces. Each of the two pieces was swollen in a different solvent (being  $d_8$ -Toluene and  $\text{D}_2\text{O}$ ) to a swelling degree of  $Q = 5$ . As the hypothesis of the PEG chain conformation in water that changes the observed RDC values cannot be tested by using  $\text{D}_2\text{O}$  as a solvent during synthesis (because the coupling agent is not soluble in  $\text{D}_2\text{O}$ ), it will be tested after a drying step and swelling of the already cross-linked gel in water.

The results of this experiment are shown in Figure 6.6. While both gels show nearly identical connectivity motif distributions (within  $\pm 2\%$ ), the respective RDC values differ significantly. Therefore, it is immediately found that the RDC values of the tPEG-tPEG gel revert back to the known values of ref. [23] once swollen in water, while the same gel in  $d_8$ -toluene shows significantly increased RDC values. Toluene is known to be a good solvent for PEG (see ref. [47], where  $\chi = 0.38$  is found), whereas water is a near  $\theta$ -solvent for PEG ( $\chi = 0.485$  at  $T = 20^\circ$  according to [22]). However, these differences do not explain the observed effect, which is why the idea of conformational changes (discussed above) is deemed plausible, whereas any relation between the increase in the RDC values and the quality of the synthesis is not excluded. Finally, this result is confirmed by the rheological experiments of Fribicz et al. in ref. [160], where the plateau modulus  $G^*$



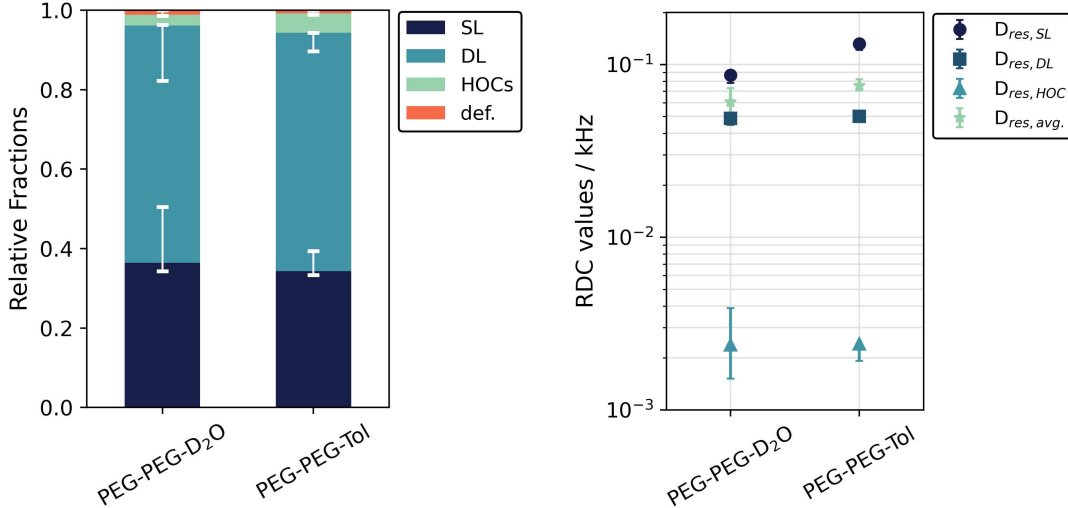


Figure 6.6: Connectivity motif fractions (left panel) and corresponding RDC values (right panel) for a tPEG-tPEG gel synthesized at  $c_{\text{prep}} = 2c^*$  in d<sub>8</sub>-toluene, cut into two pieces and reswollen in d<sub>8</sub>-toluene and D<sub>2</sub>O to  $Q = 5$  respectively.

of the same system was investigated in both solvents. It is found that the RDC values quantitatively follow the expected behavior ( $D_{\text{res}} \propto G^*$ ) as the plateau moduli obtained in ref. [160] ( $G_{\text{tol}}^*/G_{\text{water}}^* \approx 1.6 - 2.2$ ).

On a last note, it should be mentioned that the high relative precision of the hereby used MQ NMR experiment (and the evaluation procedure) is proved again by this experiment. While both systems show changes in the RDC value up to a factor of nearly 2, the extracted connectivity motifs are perfectly overlaying. Although the systematic error for the tPEG-toluene system is significantly smaller (because of an increase in the "effective contrast" as the RDC values are more spread apart), even the tPEG-water system, where the RDC values are relatively close to each other, allows for quantification of all motifs.

### 6.2.3 Additional crosslinking after drying

During the course of the investigation of the ACPNs, the peculiarity of a decreasing equilibrium degree of swelling with an increasing number of swelling + drying cycles has been observed. As shown by Bunk et al. [47], it decreases from  $Q_{\text{eq}} \approx 20$  ( $c_{\text{prep}} = c^*$ ) to about  $Q_{\text{eq}} = 10$  for all solvents and temperatures investigated. As  $Q \propto \rho_c^{-1}$  in an ideal rubber with  $\rho_c$  being the crosslink density, this decrease would imply an increase of  $\rho_c$  by a factor of two, which strongly contradicts both the <sup>1</sup>H-NMR spectra (revealing a conversion of at least 95%) and the MQ NMR results presented above (revealing an upper limit of 9% for dangling chain ends + sol + protonated solvent). Therefore, the following hypothesis seems more likely: It is assumed that open chain ends are much closer to each other while in the dried state (as  $c^* \propto \phi^{1/(6\nu-2)}$  with  $\nu=0.588$ ), therefore resulting in the formation of crosslinks spanning parts of the sample that would be far apart from each other in the swollen state. Therefore, a small number of additional crosslinks may influence the macroscopic degree of swelling by a significant margin.



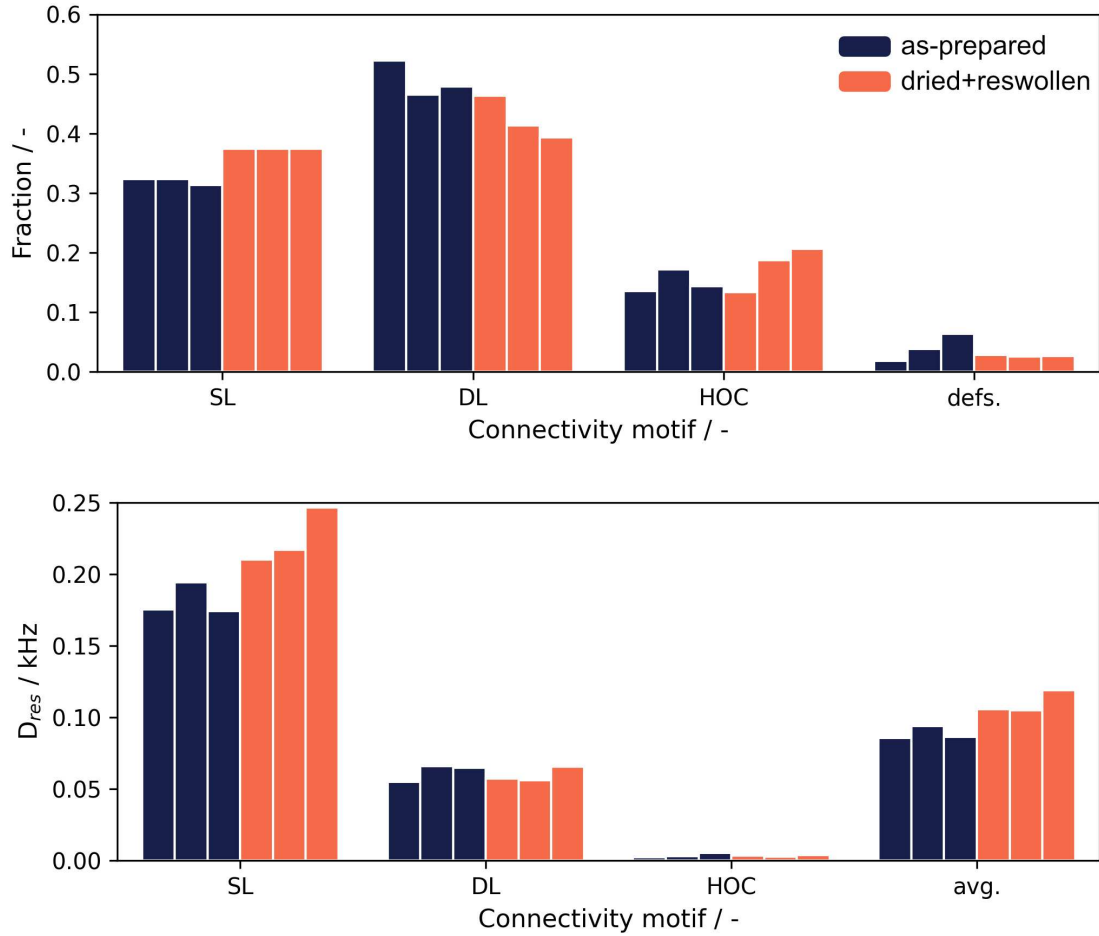


Figure 6.7: Comparison of fraction of connectivities (top) and RDC values (bottom) the three samples with stoichiometric ratios (tPEG:PCL)  $r$  as-prepared (blue bars) and after a single drying-reswelling to  $Q_{\text{prep}}$  cycle (red bars). Stoichiometric ratios ( $r = 1.0; 1.1; 1.2$ ) correspond to the respective bars ordered from left to right.

This postcured state has been investigated using both MQ NMR and small-angle x-ray scattering (SAXS). For the SAXS results, which comprise a study of the change in the correlation length  $\xi_c$ , the reader is referred to section 7.1.1. For the MQ NMR investigation, a set of three samples with slightly different stoichiometry ( $r=1$ ,  $r=1.1$ ,  $r=1.2$ ) synthesized at  $c = c^*$  and  $T = 80^\circ\text{C}$  are investigated both "as-prepared", as well as after drying + reswelling to  $c = c_{\text{prep}}$  step. The results for both the connectivity fractions and the RDC values are shown in Figure 6.7. In the as-prepared state, no changes in the microstructure in terms of a distorted connectivity distribution for  $r = 1 - 1.2$ . The only noticeable difference is an expected increase in the isotropic defect fraction with an increasing deviation from  $r = 1$ . The post-cured samples, however, show a noticeable trend compared to the as-prepared samples, including a lower defect fraction (1% for the three samples) and an apparent increase in the RDC value of the single link fraction (about 50 Hz). On top, the SL fraction shows a small but systematic increase (about 5 – 10%), which suggests that additional (strongly stretched) crosslinks may be included in that fraction (since fitting an additional component is not feasible due to the number of parameters). This

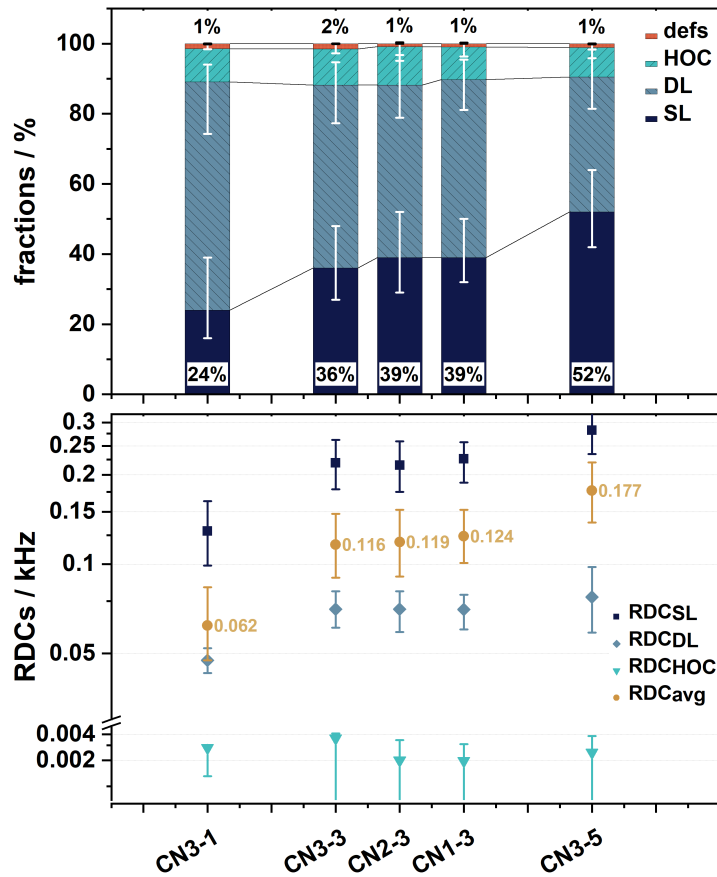


Figure 6.8: Fraction of connectivities and residual dipolar couplings for a set of tPEG-tPCL gels (see Table 6.1) after drying and reswelling to synthesis degree of swelling. Reprinted with permission from ref. [47]. Copyright 2023 American Chemical Society.

may also explain the observed increase in the corresponding RDC fraction. For the other connectivity motifs (DL, HOC) no systematic changes are found.

Finally, a concentration variation ( $1c^*$ ,  $3c^*$ ,  $5c^*$ ) of tPEG-tPCL-ACPNs after drying and reswelling to  $c_{\text{prep}}$  is investigated in Figure 6.8. Due to the additional crosslinking in the dried state no significant defect contribution is found across all concentrations, while the typical connectivity motif distribution is preserved. At high concentrations ( $c = 5c^*$ ), the SL motif eventually dominates the overall structure of the network. However, comparing the average RDC value with the as-prepared networks explained in the previous section, even at  $c = 3c^*$ , where the defect contribution was already very low in the as-prepared state ( $\approx 1-2\%$ ), a significant increase in the average RDC value is observed (from 70–90 Hz to about 120 Hz). This strengthens the assumption that a minority component of additional crosslinks of only 1–2% is able to significantly influence the whole network chain mobility due to the superposition of a small fraction of highly-stretched chains.

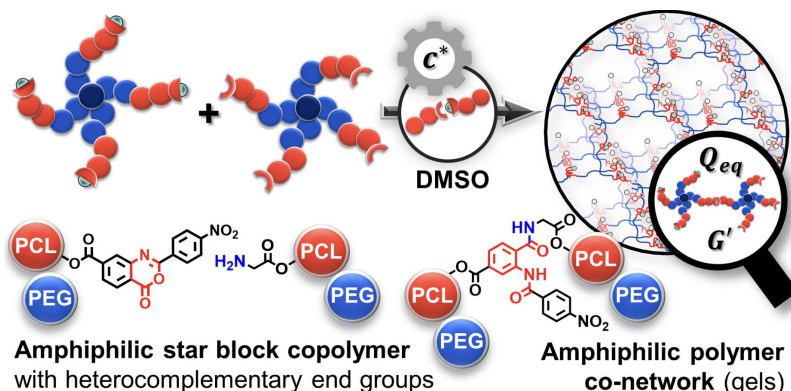


Figure 6.9: Scheme depicting the reaction strategy for the tPEG-b-PCL block star networks. Image reprinted from ref. [151].

#### 6.2.4 Pure precursors vs. block-star precursors

Another aspect of the investigation was the comparison of microstructural differences between networks synthesized by end-linking of purely hydrophilic (tPEG) and hydrophobic (tPCL) components and networks synthesized using a similar chemistry but block-star precursors where both components are included in each precursor (see Figure 6.9). As described in 5.1.1, precursors of a similar molecular weight and end group functionalization were prepared by Carolin Bunk (see Table 6.2 for specifications), with the difference being that each star is comprised of an inner PCL core with PEG wings attached instead of the separated tPEG and tPCL precursors. All results presented in this section are published in [151].

A set of 4 networks with preparation conditions (and results that will be discussed in this section) noted in Table 6.2 was prepared at preparation concentrations ranging from from  $c_{\text{prep}} = 0.5 - 2.5 c^*$  (with  $c^* = 76 \text{ g L}^{-1}$  [151]) and investigated using  $^1\text{H}$  static low-field MQ NMR and a setup comparable to the one used in section 6.2. Due to the overall low defect fraction found in all samples, a subtraction procedure for protonated solvent was not feasible because the error is on par with the obtained values.

A strong concentration dependence is observed for the networks synthesized at  $c = 0.5c^*$  and  $c = 1c^*$ , indicating an increase in the overall SL fraction from 4% to 33% that is accompanied by an increase in the corresponding RDC value from 90 Hz to 123 Hz. For networks above  $c^*$ , the observed increase in these values is present but less steep, aligning well with theoretical expectations [48] and experimental observations for the previously discussed tPEG-tPCL ACPNs. It is found that the absolute RDC value of the SL motif is significantly lower than the corresponding value observed in the ACPNs discussed before. One reason may be the usage of a different solvent ( $d_6$ -DMSO instead of e.g.,  $d_8$ -toluene) and a connected change in the microstructure of the PEG chain, as already observed for the case of  $\text{D}_2\text{O}$  vs.  $d_8$ -toluene (see section 6.2.2). The observed defect fractions are in alignment with the conversion rate obtained from high-resolution  $^1\text{H}$ -NMR spectra displayed in Table 6.2 and follow the overall expected concentration dependence dictated by the available number of reaction partners. For all gels synthesized above  $c^*$ , MQ NMR finds a network structure that is nearly free of elastically inactive structures occurring in

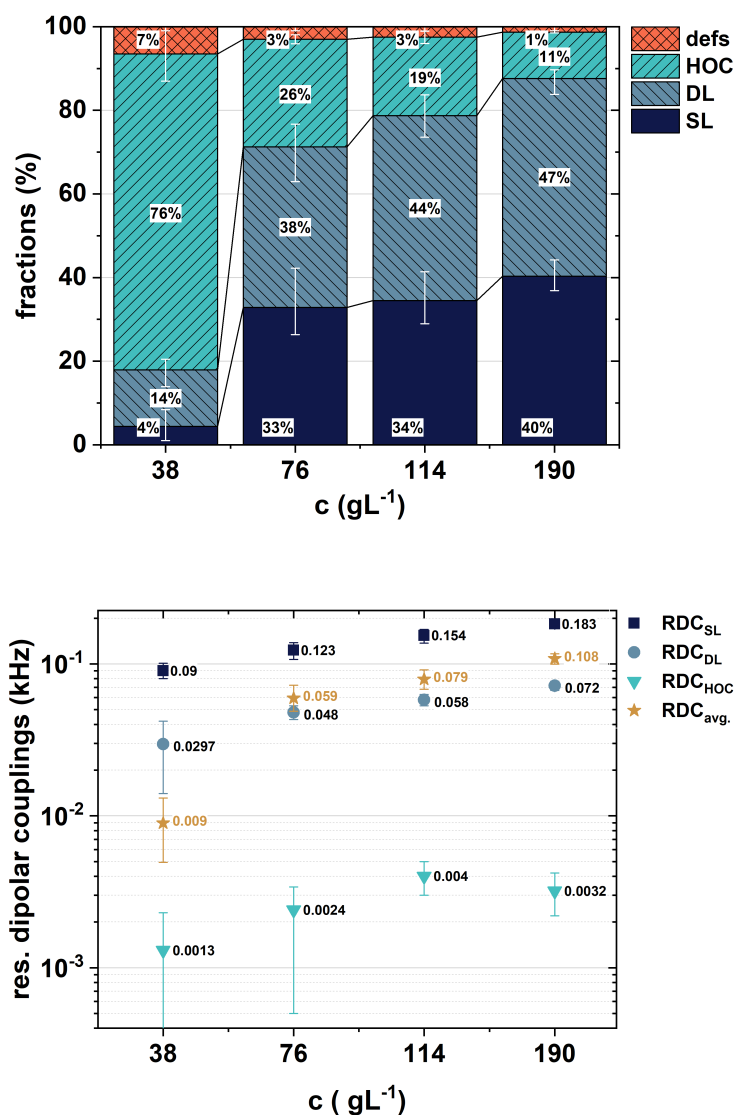


Figure 6.10: Fractions of connectivities and corresponding residual dipolar couplings for a set of tPEG-b-tPCL gels (see Table 6.2 for details). Reprinted with permission from ref. [151]. Copyright 2023 American Chemical Society.

heterocomplementary end-linked networks (dangling chain ends and unbound precursors) and a structure that can be analyzed in terms of a discrete connectivity motif distribution, indicating a model-like network structure.

However, it should be noted that a more in-depth comparison of the differences in network topology arising from the usage of pure or block-star precursors is not possible, as the overall accuracy is overshadowed by experimental issues related to the usage of DMSO as a co-solvent. Not only exists a possibility that it changes the RDC values of the network strands by inducing conformational changes in the PEG chain (which was noticed after this data was acquired) but on top it complicates the overall synthesis procedure because of its hygroscopic properties. In ref. [151] extensive monitoring of the reaction kinetics was realized by usage of e.g., rheology, which shows a two-step reaction process that significantly deviates from the similar data observed for ACPNs in ref. [47]. It is assumed that the

hygroscopic properties of DMSO lead to a surface layer of water that easily influences the overall synthesis conditions, as both the coupling agent and the PCL core are insoluble in water. As a result, a complicated and strongly temperature-dependent reaction kinetics is observed, thus disabling the possibility of generating physically-motivated conclusions based on a comparison of the tPEG-tPCL and tPEG-b-PCL systems. Future experiments will require a change in solvent to e.g.,  $d_8$ -toluene to quantitatively explore changes in the network topology based on the precursor type used.

### 6.3 Hydrogels from homocomplementary tPEG precursors

In contrast to the A4-B4-type networks investigated before, here a homocomplementary equivalent of similar molecular weights and concentrations is studied. By changing the type of reaction, odd-numbered cyclic defects (see section 2.3.2) such as primary loops are no longer suppressed and are expected in significant numbers. However, so far no experimental analysis of the connectivity motif distribution of end-linked homocomplementary networks has been performed, which motivated this study. As explained in more detail in section 5.1.2, tPEG stars were end-functionalized with a disulfide group by Zhao Meng to allow for S-S bonds as an end-linking reaction. While other systems discussed later on (such as the TPY-Zn system) allow for non-selective crosslinking as well, the hereby-used chemistry consists only of a comparably small end-linking group, which neither has the possibility to cluster nor does it need the addition of ions as coordination centers, both of which induce another layer of complexity.

Again, static time-domain MQ NMR is applied to characterize networks in terms of connectivity motifs and directly compare them to existing data [23, 69] and theoretical predictions [48]. Therefore, a set of 5 gels at different preparation concentrations was measured as prepared at  $T = 30\text{ C}$  using the low-field NMR setup described in section 5.2 with the samples stored in gas-tight vials to prevent solvent evaporation during the course of the experiment. All measured MQ NMR curves display a well-defined shape that can be reproduced by using the 3-component model for extraction of SL, DL and HOC fraction, as well as the isotropic defect contribution. It can be immediately seen from the raw data, that the samples show a very strong concentration dependence with a "narrowing shape" towards higher preparation concentrations (see Figure 6.11). This indicates both a con-

Table 6.2: Overview over the tPEG-b-PCL samples measured using MQ-NMR. The Table displays preparation concentration ( $c$ ), connectivity motif fractions extracted from MQ NMR ( $f_i$ ), reaction conversion measured by Carolin Bunk using  $^1\text{H}$ -NMR ( $p$ ), solvent and gelation temperature ( $T$ ).

$c/\text{g L}^{-1}$	$f_{\text{SL}}/\%$	$f_{\text{DL}}/\%$	$f_{\text{HOC}}/\%$	$f_{\text{defs}}/\%$	$p$	solvent	$T/^\circ\text{C}$
38	4	14	75	7	$\geq 0.90$	$d_6$ -DMSO	30
76	33	38	26	3	$\geq 0.95$	$d_6$ -DMSO	30
114	34	44	19	3	$\geq 0.95$	$d_6$ -DMSO	30
190	40	47	11	1	$\geq 0.95$	$d_6$ -DMSO	30

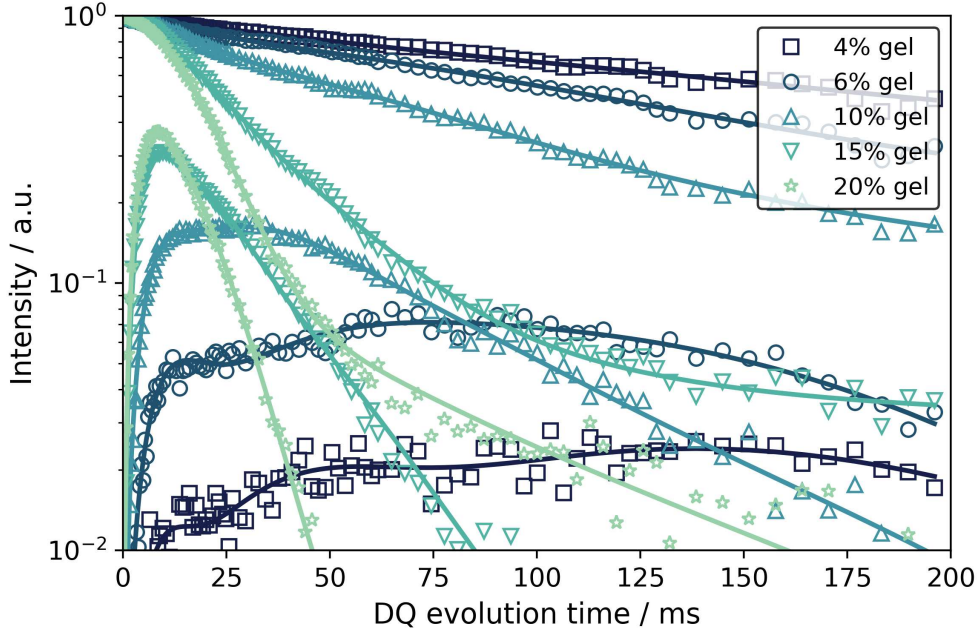


Figure 6.11: Experimental curves ( $I_{\Sigma MQ}$  and  $I_{DQ}$ ) as measured by MQ NMR are shown for various preparation concentrations ( $c_{\text{prep}}$ , at which they are also measured).

tinuous increase in the regular linking fraction, as well as the corresponding RDC value towards higher values, respectively. Additionally, there is a nearly continuous downward shift of the long tail of the  $I_{\Sigma MQ}$  data (with an exception being the highest concentration), resulting in the expected strongly concentration-dependent fraction of isotropic defects. Quantitative results of the data deconvolution can be found in Figure 6.12.

Generally speaking, the observed behavior is expected for any kind of gel (see e.g., [5, 47, 48, 52, 69, 88]). However, the very steep changes observed are rather exceptional, indicating a unique feature of systems that do not use a heterocomplementary coupling reaction and, therefore, do not suppress the formation of odd-order loops (most dominantly primary loops). From a theoretical point of view, Schwenke et al. [48] predicted the frequency of occurrence of primary loop defects in these kind of systems by using bond-fluctuation model simulations. For the lowest concentration used here ( $c = 0.5c^*$ ), a primary loop fraction of stars with a single intra-star loop  $f_1 \approx 0.2$  is predicted, plus an additional fraction of stars with two intra-star loops (therefore a completely unbound precursor) of  $f_2 \approx 0.01$  is found. Comparisons from the experimental side can only be made on heterocomplementary reactions with  $A_4$ - $B_2$  systems, which are able to form inter-star primary loops. For that, Zhou et al. claims a primary loop fraction of about 0.3 as a turn-over point at which their  $A_2$ - $B_3$  gels will fall apart into a solution of macromers, while in the  $A_4$ - $B_2$  gels of Ahmadi et al. (see section 6.4 and ref. [55]) an overall defect fraction (including sol) of 40 – 50 % is found. However, in this work most of this is attributed to dangling ends and primary loops. Therefore, a high fraction of defects is expected a priori, due to the fact that a non-heterocomplementary reaction is used.

As seen in Figure 6.13, the overall conversion rate from the precursors to the gel is above

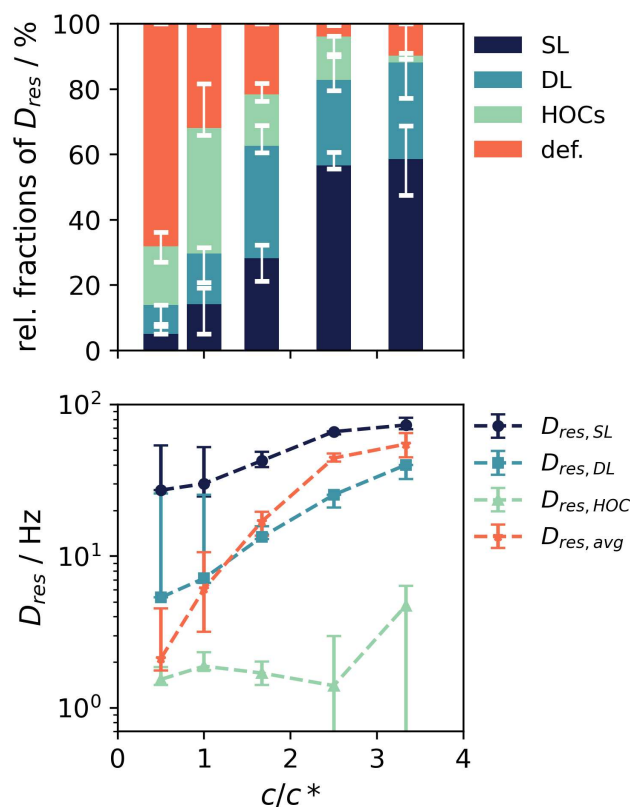


Figure 6.12: Extracted values of relative fractions of connectivity motifs (top), as well as corresponding RDC values (bottom) are plotted against the  $c_{\text{prep}}$ . All plots reveal a strong and clear dependence of the fraction of regular crosslinks (single links) and the primary defect fraction on  $c_{\text{prep}}$ .

95% for all gels synthesized at or above the overlap concentration. The one sample below the overlap concentration at  $c = 0.5c^*$  shows a strong drop in the conversion (61%) which is accompanied by an equally sudden drop in the non-defect fraction obtained by NMR (1 - defect fraction). As the conversion only tracks the sol content, the difference in these two values can be taken as a measure for the primary loop content and dangling chain ends. In addition, shown in 6.13 is a visual comparison of the simulation data of [48] and the primary loop + dangling chain fraction obtained by MQ-NMR. It is found that the values obtained here are consistently higher (with one outlier as an exception) than the simulation data. One reason may be the prevalence of nonfunctionalized tPEG precursors, which results in an overall increase in the defect fraction, as both the sol and the dangling chain content increases. Another reason may be unfavored (fast) reaction kinetics, which results in a surplus of large-scale frozen inhomogeneities, which in turn results in an increase in dangling chains as well.

Concerning the distribution of connectivity motifs, a strong dependency of the SL fraction on the overlap concentration is found. Below the overlap concentration, a nearly vanishing number of single links of only 3 – 5% is found, while the fraction of isotropic material (75%) is dominating. While this generally indicates a poorly crosslinked network, it may be that the SL fraction is underestimated due to the overall destabilizing influence of



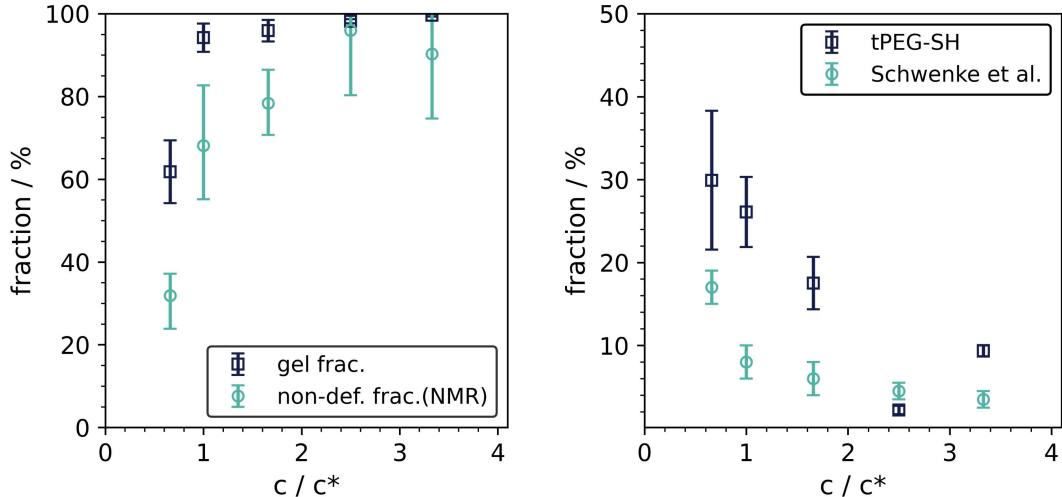


Figure 6.13: Left: Comparison of non-defect fraction from MQ NMR with measurements of the sol after synthesis. The difference in these two values can be attributed to mostly dangling chain ends and first order primary loops, as MQ NMR detects the sum of sol and dangling chain ends, whereas [100% - gel fraction] is only a measure of the sol. Right: Reprint of data from ref. [48], as well as the difference between the gel fraction and the non-defect fraction from MQ-NMR. Error bars for the data of Schwenke et al. are increased in comparison to ref., as the data needed to be extracted by eye from the given graphs.

the defect fraction. As this strongly violates the base assumption of a set of well-defined connectivity motifs, fractions cannot be estimated with certainty. With increasing concentration, the probability of intra- vs. inter-star connections is shifted towards elastically active crosslinks simply due to the stochastic argument of an increased chance of finding another precursor within a certain radius due to a decreasing spatial distance. At these concentrations, distinct components are easily identified in the experimental data, resulting in the identification of fractions with relatively high certainty.

The residual dipolar couplings obtained here are generally in agreement with the data expected for a tPEG network with a precursor molecular weight of  $M_c = 10$  kDa. The RDC values of the regular links are found between  $\approx 25 - 70$  Hz with the variation arising from the dominating presence of the defects. The corresponding RDC values of the double link motif are found between  $\approx 1 - 20$  Hz and roughly correspond to the postulated factor of 3–4 with the exception of the sample with  $c < c^*$ . For  $c < 2.5 c^*$  there are distinct deviations from the original tPEG system, whereas above no distinctions are found regarding not only the average RDC value, but also the fraction of single links (see Figure 6.14).

Lastly, the results from MQ NMR are compared to results obtained from rheology (measured by Zhao Meng, see section 5.1.2). Both datasets show a near perfect agreement (see Figure 6.15) when comparing the average RDC value with the plateau modulus. For low concentrations, both the modulus and average RDC values reflect the dilution effect from the signification fraction of defects, while at higher concentrations the overall connectivity distribution dominates the behavior. As no deviations are to be found, it is concluded that the gels do not tend to form structures that may affect rheology but not MQ NMR (such as, e.g., clusters) due to differences in microscopic and macroscopic elastic responses.



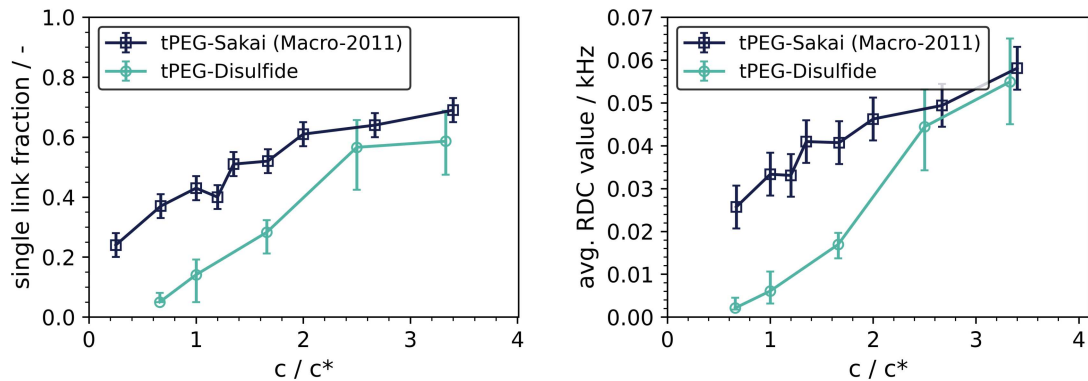


Figure 6.14: The Figure shows characteristic values (fraction of single links [top] and average RDC value [bottom]) obtained from the MQ NMR analysis. Plotted reference values for the typical tPEG + D2O system from Sakai et al. are taken from ref. [23] with increased error bars.

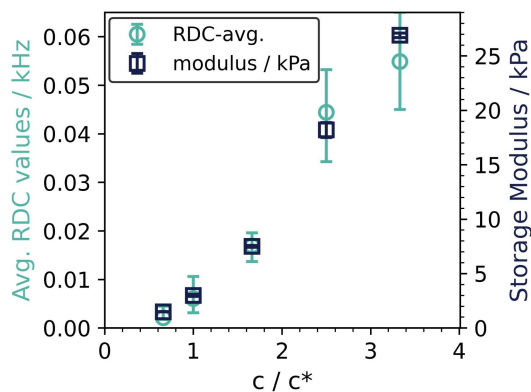


Figure 6.15: Shown are the weighted average of the measured RDC as obtained from MQ NMR (left axis), as well as the plateau storage modulus (right axis) as obtained from rheological measurements. In order to show the expected proportionality between these values, the RDC axis was scaled accordingly by definition of the upper limit value.

The results presented here are a snapshot of an A4-type gel, which is rarely studied in the literature due to the advantages of the A4-B4 architecture in preventing odd-numbered loop structures (with the primary self-loop being the most dominant one). However, this study shows that at higher concentrations the performance of these gels in terms of rheological behavior and microscopic network structure is comparable to that of gels obtained by hetero-complementary reactions, while simultaneously allowing for a more simple chemistry.

## 6.4 Quantification of ion-mediated structures in metal dual-networks

A special subset of PEG-based hydrogels are dual-network hydrogels, where the network crosslink is not only facilitated by a chemical end group reaction but additionally, a second

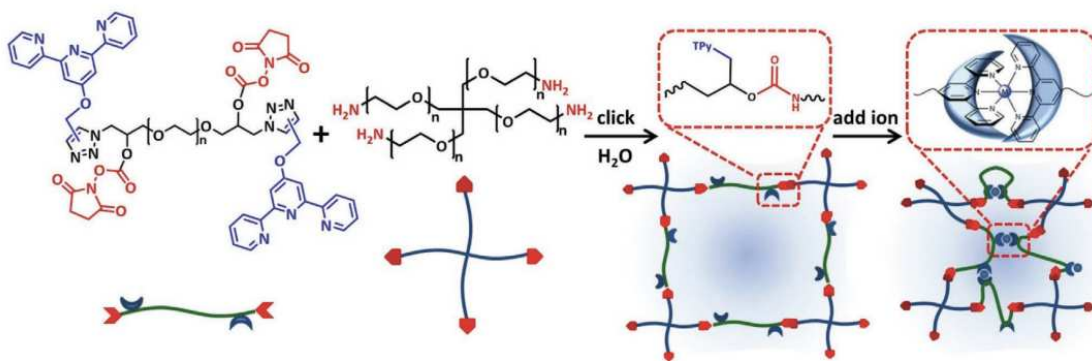


Figure 6.16: Overview of the system described in section 5.1.3. Linear 6 kDa PEG chains and 10 kDa tPEG stars are heterocomplementary crosslinked by both conventional chemical (NHS-amine group crosslink) reactions, as well as by an additional physical metal ion-mediated bond. Reprinted from [55] under the Creative Commons Attribution License.

set of crosslinks of either chemical or physical origin is present. General reinforcements due to the second set of crosslinks can lead to improved mechanical properties, such as a higher dynamic modulus or mechanical extensibility [161]. Here, a set of metallo-supramolecular dual-network hydrogels is investigated (with all presented results published in [55]), where ion-mediated physical bonds are present throughout the network, reinforcing the overall structure and leading to a set of unique topological features that can be detected by MQ-NMR. A graphical representation of the investigated system can be found in Figure 6.16. All networks (with chemical structures and details given in section 5.1.3) were measured as-prepared using the experimental setup described in section 5.2 at  $T = 40^\circ \text{C}$ . All samples were subjected to a simple time-domain FID measurement, as well as a saturation recovery experiment and the Baum-Pines sequence (see section 3.4). The longitudinal  $T_1$  relaxation times of all samples were measured not only to optimize the recycle delay for all measurements, but also to separate the fraction of isotropic defects ('tail') from the Baum-Pines sequence into a solvent contribution (long  $T_1$ ) and the actual content of sol + dangling chains (short  $T_1$ ). Therefore, a regression of the normalized relaxation curves is performed using a multi-component extension of the well-known equation for the saturation recovery build-up curve [162].

$$I_{\text{SatRec}}(t) = a_{\text{poly}}(1 - \exp(-t/T_{\text{poly}}^1)) + (1 - a_{\text{poly}})(1 - \exp(-t/T_{\text{solv}}^1)) \quad (6.2)$$

Once the fractions  $a_{\text{poly}}$  and  $a_{\text{solv}}$  and corresponding  $T_1$  values are estimated, we can identify the fraction of sol and dangling chains by using the following equation [23]:

$$f_{\text{sol+dang}} = \frac{B - A_{\text{solv}}[1 - \exp(-\tau_{\text{rd}}/T_{\text{solv}}^1)]/I_{\text{satrec}}(\tau_{\text{rd}})}{A_{\text{poly}}} \quad (6.3)$$

Then, the Baum-Pines MQ NMR sequence is used to identify local inhomogeneities and the distribution of topological connectivity motifs which are induced by the addition of the ions. Therefore, a reference network (DN-0) without the addition of metal ions is measured

Table 6.3: Results from the saturation recovery experiments depicted in Figure 6.17. Here,  $a_i$  denote the respective normalized fractions of solvent and polymer, whereas  $T_i^1$  are the corresponding longitudinal values.  $\tau_{\text{diss}}$  denotes relative values of the bond dissociation times that are further discussed in the text.\*While not applicable to the chemical network, an arbitrary value of 1 was assigned for the sake of data visualization.

Sample	$\tau_{\text{diss}}$ / -	$a_{\text{poly}}$	$T_{\text{poly}}^1$ / s	$a_{\text{solv}}$	$T_{\text{solv}}^1$ / s
DN-0	1*	$76\% \pm 1\%$	0.61	$24\% \pm 1\%$	$13 \pm 1.5$
DN-Zn	13	$60\% \pm 10\%$	0.52	$40\% \pm 10\%$	$12 \pm 2$
DN-Co	274	$40\% \pm 2\%$	0.9	$60\% \pm 2\%$	$3.5 \pm 0.2$
DN-Ni	218888	$41\% \pm 5\%$	0.2	$59\% \pm 5\%$	$0.9 \pm 0.1$

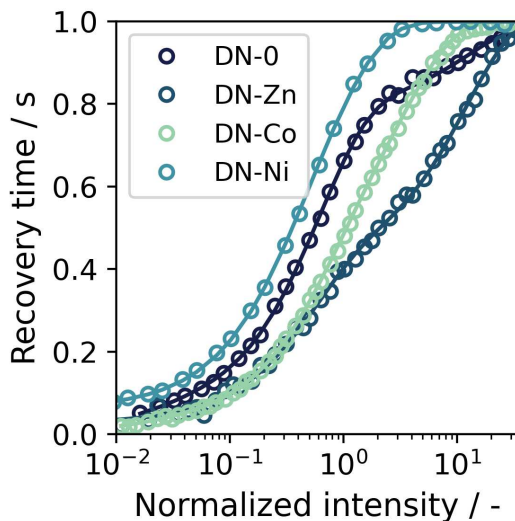


Figure 6.17: Measured normalized saturation recovery buildup curves for the dual-network metallo-gels investigated in this section. Adapted from [55] under the Creative Commons Attribution License.

and evaluated. Surprisingly, the multi-component fitting procedure explained in section 3.4.2 was not necessary, as the data only consisted of a single broad peak, which was evaluated using the point-by-point normalization explained in section 3.4.1 and fitted with the log-normal-distributed A.l.-function (see eq. 3.9) with results shown in Figure 6.18. From this, one can obtain the proton-weighted fraction of isotropic defects ( $f_{\text{def}} = 48\%$ ) by correcting the extrapolated tail fraction shown in Figure 6.18 and correcting the value obtained by the solvent contribution as described above. Furthermore, the monomodal (but strongly distributed) local amplitude of motion of the crosslink is obtained in terms of a residual dipolar coupling (RDC) value, which amounts to  $D_{\text{res}} = 2$  Hz, as well as a distribution parameter of  $\sigma = 0.5$ . The values obtained here are notable when compared with the tPEG-tPEG water reference system of Sakai et al. [23], where a much lower defect fraction of  $f_{\text{def}} = 7\%$  and a significantly higher  $D_{\text{res}}$  value of  $D_{\text{res}} \approx 70$  Hz at a preparation concentration of  $c = c^*$  are reported. The reason for the highly increased fraction of primary loops is speculated to be the influence of the linear 6 kDa crosslinker used in the synthesis, which, in contradiction to the  $A_4$ - $B_4$  chemistry of Sakai et al., does

not suppress the formation of primary loops (see Figure 6.21 for a sketch of the expected general topology). Furthermore, with the strong increase in primary loops being explained, the strongly lowered  $D_{\text{res}}$  value can be put into context. From the overall difference in the molecular weight of the crosslink (11 kDa here vs. 5 kDa in the Sakai et al. tPEG system) we find an expected difference of a factor of 2.2 according to eq. 3.7. An additional factor is found as a result of the incorporation of a significant portion of primary loops into the network. Given a high number, one can assume that, on average, each tetra-star will contain at least one primary loop, which consequently turns the star-shaped precursor into a linear extender. The results of Lang [25] mention a factor roughly equal to 2 in this case. Although this is not in precise agreement with the mobilization effect of the crosslink observed by the MQ NMR data, it provides a rough direction of the effects that strongly contribute to the observations. However, it can be speculated that the presence of a significant number of primary loops additionally fosters the presence of more complex connectivity motifs, such as adjacent structures that will be weakened due to the overall maintained force balance across the network.

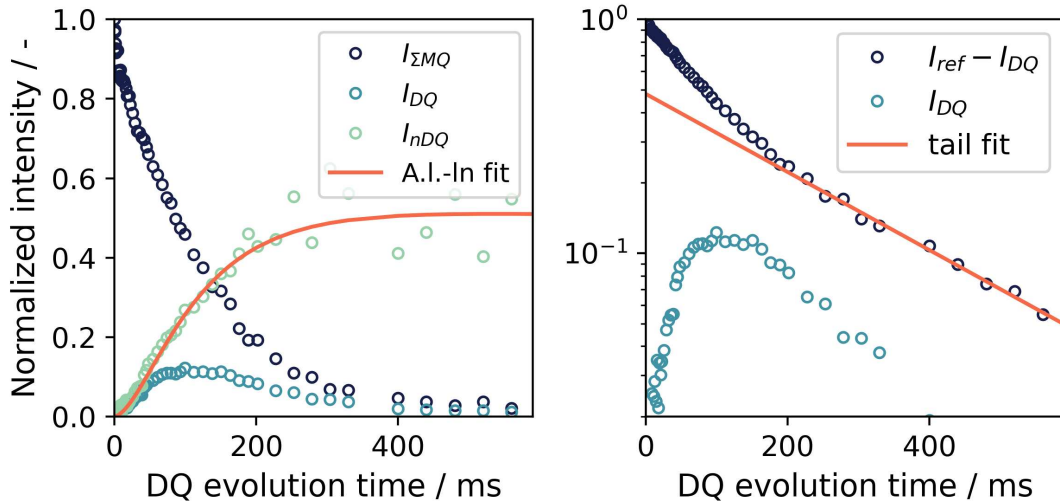


Figure 6.18: Experimental data obtained from the Baum-Pines experiment on DN-0. Left: Normalized DQ buildup curve with a lognormal A.I.-function fit. The extracted values are  $D_{\text{res}} = 2$  Hz and  $\sigma = 0.5$ . Right: Exemplary plot showing the tail subtraction procedure. Here,  $I_{\text{ref}} - I_{DQ}$  was used to ensure that no contribution of  $I_{DQ}$  is fitted accidentally. The extracted tail fraction is  $f = 48\%$ . Adapted from [55] under the Creative Commons Attribution License.

With a baseline now established, three gels of the same structure but with a different ion were investigated. More precisely, the ions used and their respective relative bond dissociation times were zinc (Zn;  $\tau_{\text{diss}} \approx 10^1$ ), cobalt (Co;  $\tau_{\text{diss}} \approx 2.5 \cdot 10^3$ ) and nickel (Ni;  $\tau_{\text{diss}} \approx 2 \cdot 10^5$ ), covering a broad range of physical bonds with different kinetic stability ( $\text{Zn} < \text{Co} < \text{Ni}$ ). Compared to DN-0, dual-network gels with added ions (DN-Zn, DN-Ni, DN-Co) show a distinctively different MQ NMR response as shown in Figure 6.19:

(1) A single tail fraction does not result in an appropriate reduction of the data with a second relaxing component visible. Therefore, a second single exponential function with a

significantly reduced  $T_2$  relaxation time (indicating a slightly more immobilized structure) was used to properly model the experimental data. The results of the respective tail fractions are given in Figure 6.19.

(2) A point-by-point normalization as used for DN-0 was not possible and results in an oscillating curve that does not reach the plateau with  $I_{nDQ} = 0.5$  as required by the underlying physics. Therefore, a regression was performed using the multi-component fitting approach after subtraction of the first tail fraction. The second tail fraction was incorporated into the fit to ensure a more smooth overall fit.

As a result of the general evaluation procedure, two sets of values with distinct meaning, the two tail fractions, as well as the three connectivity fractions with respective RDC values and their proton-weighted fraction (see Figure 6.20), were obtained. In the measured RDC values, the same dipolar coupling already found in DN-0 can be recognized. Therefore, it is assumed that it corresponds to a simple chemical network structure. Two additional RDC values, roughly 6 – 10 Hz and 60 – 70 Hz respectively, are found. The latter value is surprisingly high, being much higher than anything that can be reasonably expected from the network structure (even considering a non-significant effective reduction of the crosslink molecular weight due to the ionic bonds). Additionally, the observed fraction of high RDC directly correlates with the relative bond dissociation times of the respective TPY-ion complexes, whose values are used as a measure to characterize the time scale of bond dissociation and related bond stability [163]. Relative bond dissociation times for these complexes are derived from rheological measurements presented in ref. [33]. The observed correlation between cluster fraction and bond dissociation times (and therefore bond stability) suggests the hypothesis of the existence of a competing gel-forming mechanism that may be related to the introduced ions. Under the assumption of static clusters, the bond dissociation times may follow the trend (while not necessarily connected in a causal way) of the overall reactivity in forming the ionic bonds; hence, an effective imprinting of the ion-related inhomogeneities during gel formation can be reasonably assumed. Emerging cluster-like structures would explain the topologically distinct fraction observed. Alternatively, the clusters may be of dynamic nature and the MQ NMR experiment measures the equilibrium partition between ions participating in clusters and network structure, respectively. The partitioning could depend on the bond dissociation times, which leads to a higher observed cluster fraction for more stable bonds.

The remaining fraction with RDC values around 6 – 10 Hz is not too far from the chemical structure and therefore can reasonably be assumed to be related to the shortened crosslinks arising from the overall reinforcement of the weak chemical structure by the additional ion-related bonds. Neither its value nor its fraction shows any dependency on the overall bond dissociation time, which is assumed to be reasonable considering that MQ NMR will measure a quasi-static (therefore constant) property once the critical timescale of milliseconds is surpassed.

The remaining question of the interpretation of the additional fraction of defects can be easily explained in a pictorial way by using Figure 6.21, which shows possible types of loop defects that can arise from the chemical structure and the ions. It can be seen that a smaller (and therefore slightly more immobilized) loop structure is formed during the

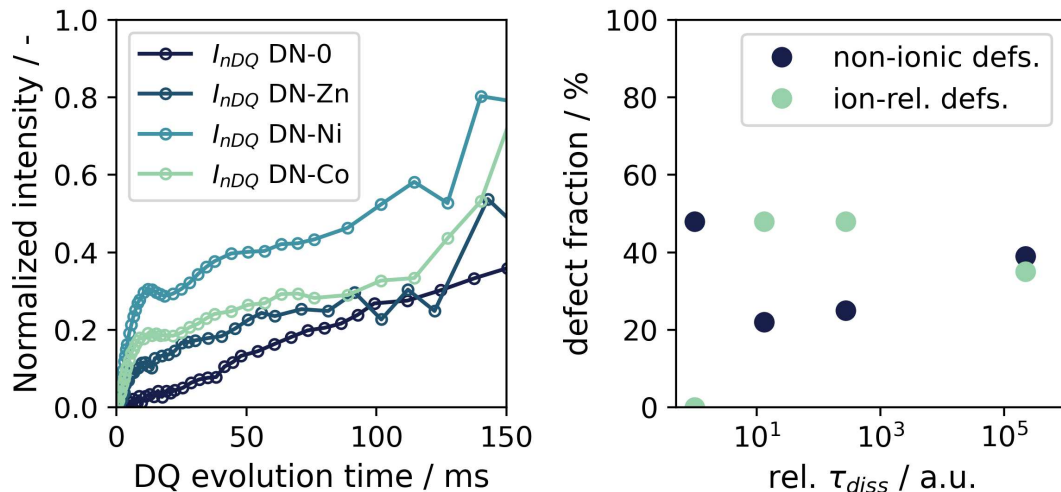


Figure 6.19: Left: Normalized  $I_{nDQ}$  curves for all networks investigated in this section. It can be clearly seen that the normalization procedure fails and the resulting signal shows oscillations arising from the respective RDC fractions. Right: Corresponding fractions for all networks in dependence on their relative bond dissociation time. Here, the chemical network is artificially set to  $\tau_{diss} = 1$ . Although no specific trend is found, it should be noted that the overall defect fraction is surprisingly high. Adapted from [55] under the Creative Commons Attribution License.

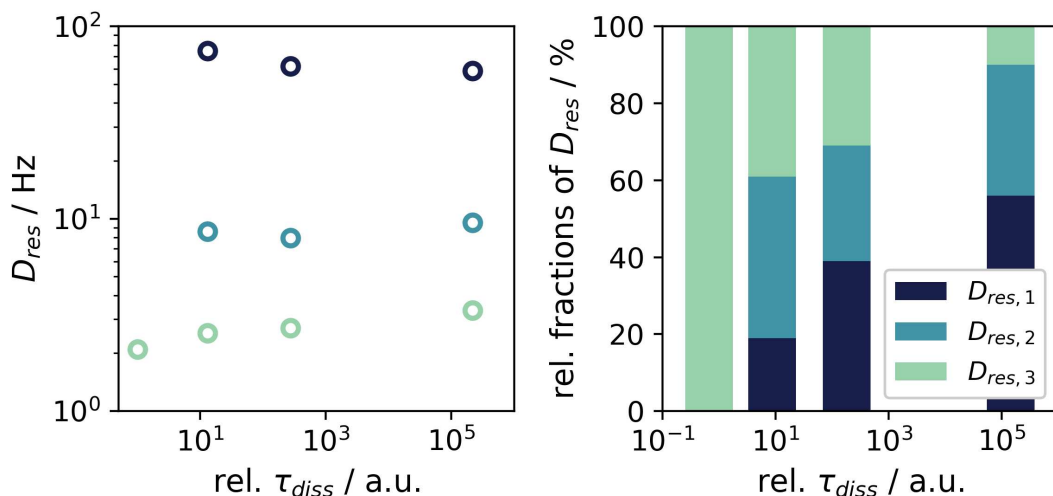


Figure 6.20: Values (left) and corresponding proton fractions (right) of the extracted residual dipolar coupling values. The proton fractions are normalized after subtraction of the tail components. It can be seen that  $D_{res,1}$  has a direct correlation to the kinetic bond stability. Adapted from [55] under the Creative Commons Attribution License.

reinforcement of the network comprising 2 arms of the tPEG precursor, as well as a short piece of the linear PEG crosslinker up to the functional terpyridine group.

Lastly, the obtained  $D_{res}$  values are compared with the correlation length obtained from static light scattering. The correlation length scale obtained from static light scattering

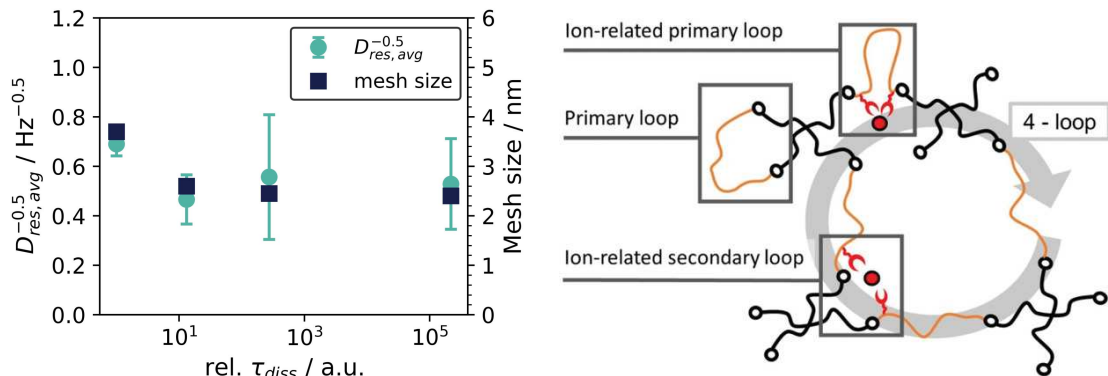


Figure 6.21: Left: Correlation of the inverse square-root proton-weighted average of the dipolar coupling after tail subtraction and the observed correlation length in static light scattering experiments measured by Mostafa Ahmadi. While the error bars of  $D_{res,avg}^{-0.5}$  are large, there is still a clear proportionality found between both measurements. Adapted from [55] under the Creative Commons Attribution License. Right: Tentative sketch of the most common cyclic defect structures that are expected in the investigated system. Reprinted from [55] under the Creative Commons Attribution License

can be expressed as follows:

$$\Xi \propto lN^\nu$$

where  $N$  is the effective number of Kuhn segments of the PEG chain. Meanwhile, the MQ NMR experiment accesses the effective number of monomers constituting a crosslink  $N$  via

$$D_{res} \propto N^{-2\nu}$$

In both cases,  $\nu$  is the excluded volume exponent and is assumed to be  $\nu = 0.6$  for a good solvent. Using the inverse square root of the average  $D_{res}$  value, we project both quantities on the same dependence of  $\propto N$  and can therefore check the expected correlation independently of  $\nu$ . As shown in Figure 6.21, both quantities of values have a nearly perfect overlap, indicating the expected correlation and fortifying the assumption that the values obtained  $D_{res}$  accurately reflect the overall network crosslink topology despite the complex local inhomogeneities.

## 6.5 Defect-controlled transient tPEG networks

In this section, another aspect of the tPEG-TPy-ZN<sup>2+</sup> system is characterized in more detail. To this end, mixtures of homocomplementary tPEG precursors of different functionality  $f$  (with  $f = 4$  and  $f = 8$ ) (see section 5.1.3 for details) are studied by MQ NMR and changes in the overall chain-level microstructure are investigated. As derived from the phantom model (see eq. 2.31), the functionality  $f$  is supposed to influence the emerging properties of a gel by increasing the storage modulus with increasing functionality [5], thus predicting mechanically superior gels with increasing number of crosslinks per arm. However, due to an experimental shortcoming (being an effective decrease in the degree



of functionalization of the 8-arm tPEG stars to about 90% in comparison to the degree of functionalization of the 4-arm stars of  $< 95\%$ ), this effect is found to be negligible. However, it will be shown that the gels emerging from these inferior precursors can be used for defect engineering (see Figure 6.22 for a tentative sketch), while still yielding an MQ NMR signal that predicts a rather well-defined connectivity motif distribution. The data presented in this chapter is published in ref. [30].

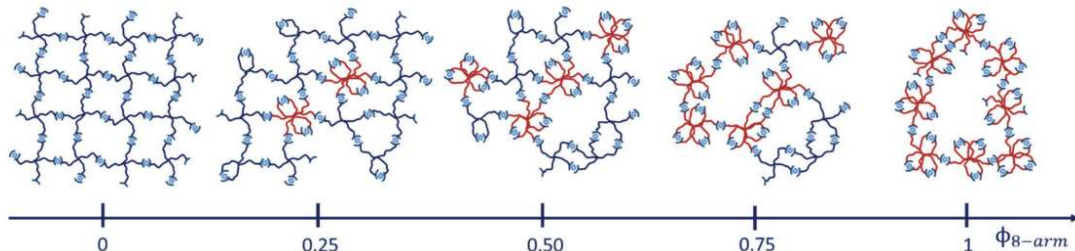


Figure 6.22: Overview of the system described in section 5.1.3. Different mixtures of PEG stars with a molecular weight of 5 kDa per arm and functionalities of 4 and 8 were crosslinked using the TPy-metal ion complex, yielding different extents of inhomogeneities depending on the volume fraction of 8-arm stars. For  $\phi_{8\text{-arm}} = 0$ , a model-like network structure was found despite the expected shortcomings of a homocomplementary reaction (see text for more information). Reprinted from ref. [30] under the Creative Commons Attribution License with permission from the Royal Society of Chemistry (RSC).

As seen in Figure 6.23, the signal curves obtained from the MQ NMR experiment show a consistent behavior for both the  $I_{\Sigma MQ}$ , as well as the  $I_{DQ}$  curve. The former shows a consistent increase of the mono-exponential tail fraction (starting at about  $\tau_{DQ} = 250$  ms) with increasing polymer volume fraction  $\phi_{40k}$  of 8-arm tPEG stars, revealing a strong dependency. Simultaneously, the  $I_{DQ}$  curves show a consistent decrease of a well-defined "bump" that is found for  $\phi_{40k} = 0$  with increasing  $\phi_{40k}$ . As the data presented show clear signs of different connectivity motifs, it is evaluated using the 3-component fitting approach described in section 3.4.2. As a result, 3 modes with different respective dipolar couplings are extracted and shown in Figure 6.24. The associated chain-level structure of the highest measured RDC value is either the regular crosslink (single link; SL) or a cluster of TPy-functionalized end groups, as previously discussed (see Section 6.4). With the regular crosslink structure having an expected molecular weight of about  $M_c = 2 \cdot M_{\text{star}} / f = 10$  kDa and the well-known corresponding RDC value of  $D_{\text{res,SL}} \approx 40 - 80$  Hz from Lange et al. [23] for  $M_c = 5$  kDa, the expected value in this case will (according to eq. 3.5) equal to roughly  $D \approx 20 - 40$  Hz, whereas clusters of TPy-functionalised end groups were found to show RDC values being orders of magnitude higher than the regular crosslink structure. As the values measured here vary between 30 and 50 Hz, it indicates that the SL fraction is measured.

In addition, the secondary fraction extracted from the fitting procedure is of a dipolar coupling that is lower by a factor of 4, suggesting that secondary loop structures are measured, which are known to have RDC values lower by a factor of 2 – 4 [23]. Lastly, a surprisingly high fraction of a very mobile structure with RDC values between 0.7 and 2 Hz is found, which in this work is associated with higher-order connectivity defects (HOCs).



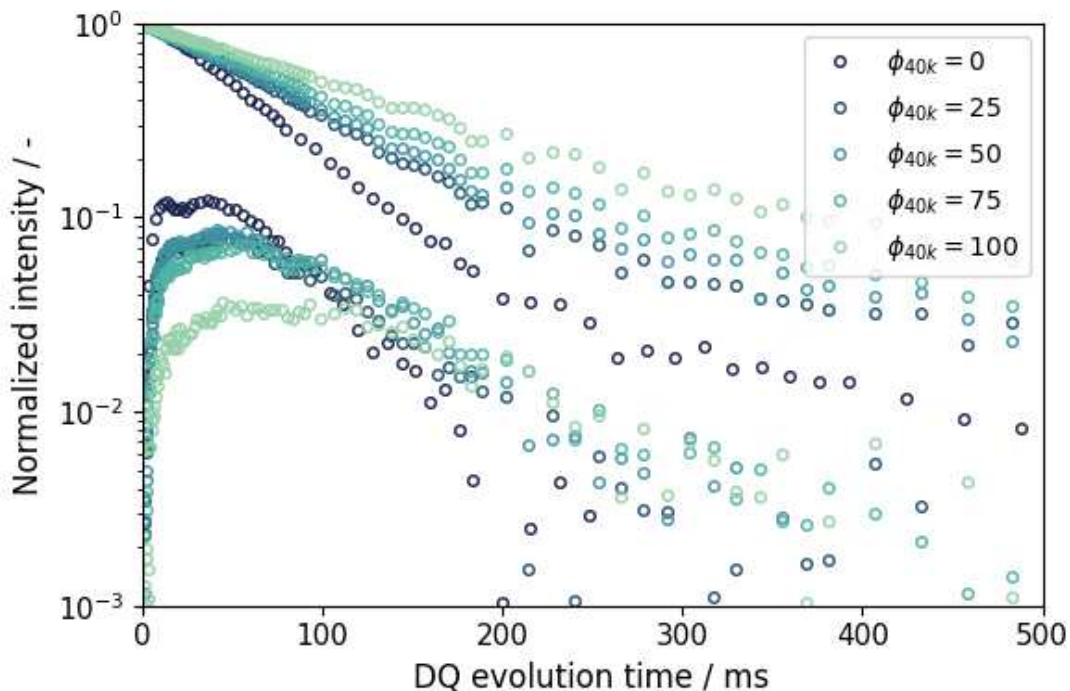


Figure 6.23: Measured data from the MQ NMR experiment for networks made from different fractions of 8-arm PEG stars ( $\phi_{40k}$ ). Shown are both the  $I_{\Sigma MQ}$  data (top curves) and the  $I_{DQ}$  data (bottom curves). Adapted from ref. [30] under the Creative Commons Attribution License with permission from the Royal Society of Chemistry (RSC).

Evaluating the fractions of connectivities and isotropic defects, the most striking feature of this sample series is the strongly increasing number of isotropic material from an unexpectedly low defect fraction of about 1% towards up to 51%. Although protonated water from H-D exchange may contribute to this fraction, it is assumed that it is negligible, as all samples are prepared in the same way, using the same solvent and concentration. Therefore, since one sample shows a total isotropic fraction of only 1%, this assumption seems justified. Given the fact that the tPEG-TPy-Zn system is able to perform primary intra-star loops, the measured (low) defect fraction is highly surprising. As the TPy-Zn complex is a transient one (average lifetime about 800 ms [164]), one could assume that a distance equilibration of star centers took place, which may result in a strong reduction of primary loops. However, it should be noted that this phenomenon (or type of network) was not studied before using MQ NMR or similar methods that quantify the primary defect fraction, thus no proof or reference can be provided. For the strong dependence of the overall increasing defect fraction on  $\phi_{40k}$ , two reasons can be provided: 1) 8-arm tPEG stars have a known lower overall degree of functionality (90%), which compared to the 4-arm stars (> 95%) will inevitably lead to an increase in the fraction of dangling chain ends not bound to the overall network. However, an upper boundary can be formulated as twice the fraction of nonfunctionalized material, assuming that each dangling end will cause at maximum a single other dangling end as a consequence. Even using this overestimated value, there is an increase in defects of at least 30% being unexplained. Therefore,

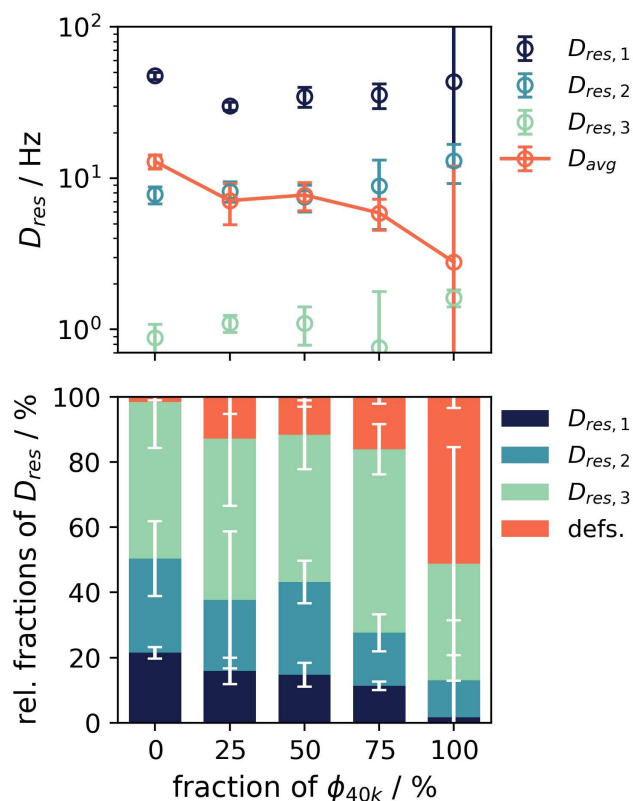


Figure 6.24: Residual dipolar coupling values (top) and corresponding proton fractions of connectivity motifs (bottom) that were extracted from the data shown in Figure 6.23. A clear decrease of the overall proton-weighted average RDC value (red line), as well as a clear increase in the primary defect fraction (red bar) is observed. Adapted from ref. [30] under the Creative Commons Attribution License with permission from the Royal Society of Chemistry (RSC).

it is concluded that the addition of 8-arm tPEG stars to the 4-arm tPEG star system will result in the formation of a significant number of primary loop defects. Although this is not a priori expected from theoretical considerations (which predict an increase in the plateau modulus obtained from rheological experiments with increasing number of arms and therefore exclude a significant increase in the primary loop fraction), one can speculate that this observation is tied to the fact that homocomplementary coupling chemistry was used. Once an 8-arm tPEG star is bound to the emerging network structure and the gel point already surpassed, the probability of intra-star crosslinks (primary loops) may be comparable to the probability of inter-star crosslinks (regular crosslinks or other connectivity defects). While, generally speaking, this line of argumentation is valid for any f-arm star precursors, the increase in the number of arms may cause additional sterical challenges tipping the scale, while the increased fraction of nonfunctionalized arms may also slow down the overall reaction, leaving more time for intra-star crosslinks to occur. Overall, it can be concluded that the expected relationship of modulus and RDC values vs. functionality is not only not reproduced, but a contrary behavior was measured ( $G^* \approx 12.5 \text{ kPa}$  for  $\phi_{40k} = 0$  vs.  $G^* \approx 3 \text{ kPa}$  for  $\phi_{40k} = 1$ ) as shown in Figure 6.25. Nevertheless,

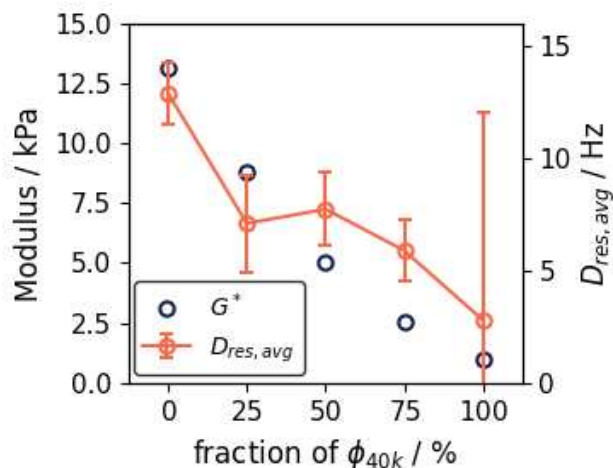


Figure 6.25: Proton-weighted average of the residual dipolar coupling values shown in Figure 6.24 are plotted and the axis rescaled to overlap with the storage moduli measured on the same networks by Paola Nicolella. It can be seen that the moduli show a stronger response to the change in  $\phi_{40k}$  than the  $D_{res,avg}$  values. However, a qualitative trend is preserved. Adapted from ref. [30] under the Creative Commons Attribution License with permission from the Royal Society of Chemistry (RSC).

the results of these experiments are valuable, as fortunately an interesting set of defect-engineered gels with a rather well-defined set of connectivities was found. Interestingly, a recent work of Darby et al. [31] investigates a similar system of tPEG stars with a molecular weight of crosslinking of  $M_c = 5.0$  kDa (being half the  $M_c$  used here) and a similar non-selective metal-ion chemistry. However, they arrive at a different result, showing that the plateau modulus  $G^*$  increases from  $\approx 18$  kPa (10 wt% 10 kDa 4-arm PEG) to  $\approx 32$  kPa (10 wt% 20 kDa 8-arm PEG), as expected, with increasing functionality. So far, the reason for this discrepancy is not fully explained, as the only observable differences are the differing molecular weight, as well as the difference in end group conversion (being 98 % for Darby et al.). For now, this independent set of experiments is interpreted as a confirmation of the hypothesis posed above, which states that the strong difference in conversion may be the driving factor of the observations given here. While it can now be corrected that the homocomplementary coupling chemistry itself is not enough of a deciding factor, it may dominate the overall behavior in conjunction with the relatively low end group functionalization and the distorted kinetics of forming intra- vs. inter-star crosslinks.

## 6.6 Connectivity motifs of transient networks at different self-sorting regimes

So far, the investigated networks using metal ion-based crosslinking chemistry have shown a significant influence of primary loops because of the nonselective nature of the coupling chemistry. Here, a set of metallo-supramolecular tPEG-based gels is synthesized by Mostafa Ahmadi, by using a metal-ion-facilitated reaction (see Figure 6.26) of tPEG pre-

cursors functionalized with a sterically demanding 2,9-bis(mesitylene)-1,10-phenanthroline (DMPhen) and tPEG precursors functionalized with a slim phenanthroline (Phen) or terpyridine end group (TPy). Due to the transient nature of the bond, these networks are supposed to facilitate a certain degree of self-healing and structure equilibration, with the extent (related to the bond dissociation time) depending on the overall degree of self-sorting. When ions that prefer certain coordination geometries and two different end-linking groups are used, the kinetic bond stability can be varied systematically. This mechanism is assumed to be capable of overcoming the inherent disadvantage of frozen permanent defects and is therefore assumed to yield networks with a reduced content of primary loops. All results presented in this section are published in ref. [152].

A set of six networks was analyzed using three different ions ( $\text{Cu}^+$ ,  $\text{Zn}^{2+}$ ,  $\text{Co}^{2+}$ ) and two different combinations of end-linking (DMPhen-TPy and DMPhen-Phen). Baum-Pines MQ NMR measurements were performed on a Bruker MiniSpec mq20 at  $T = 25^\circ\text{C}$  with the samples kept in glass tubes with a diameter of 10 mm and a height of 8 mm to exclude sample evaporation (see section 5.2). The experiment is used to quantify the distribution of connectivity motifs and the primary defect fraction.

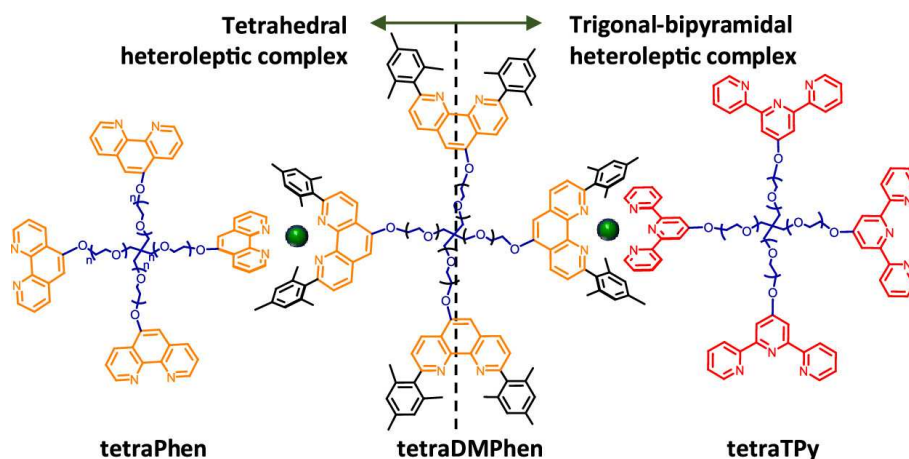


Figure 6.26: Reprinted from ref. [152] with permission. Copyright 2023 American Chemical Society.

As the primary loop fraction (or rather its absence) is of particular interest in this set of experiments, it is mandatory to deconvolute the isotropic sample fraction obtained from MQ NMR into the primary loop fraction and the solvent contribution, respectively. Therefore, a saturation recovery experiment is recorded on top to quantify the proton fraction of solvent and consequently extract the proton fraction of the primary loops using the procedure and equations mentioned in section 6.4. With the results shown in Table 6.4, it is evident that, depending on the ion, highly different values of the longitudinal relaxation times of the solvent  $T_{\text{solv}}$  are found, while being consistent within a comparison of two samples containing the same ion. This intermediary result strongly undermines the need for an additional saturation recovery experiment when paramagnetic ions (significantly shortening the  $T_1$  relaxation times) are used and even more when cross-sample comparisons are made.

The obtained data sets were evaluated using the multicomponent fitting approach (see

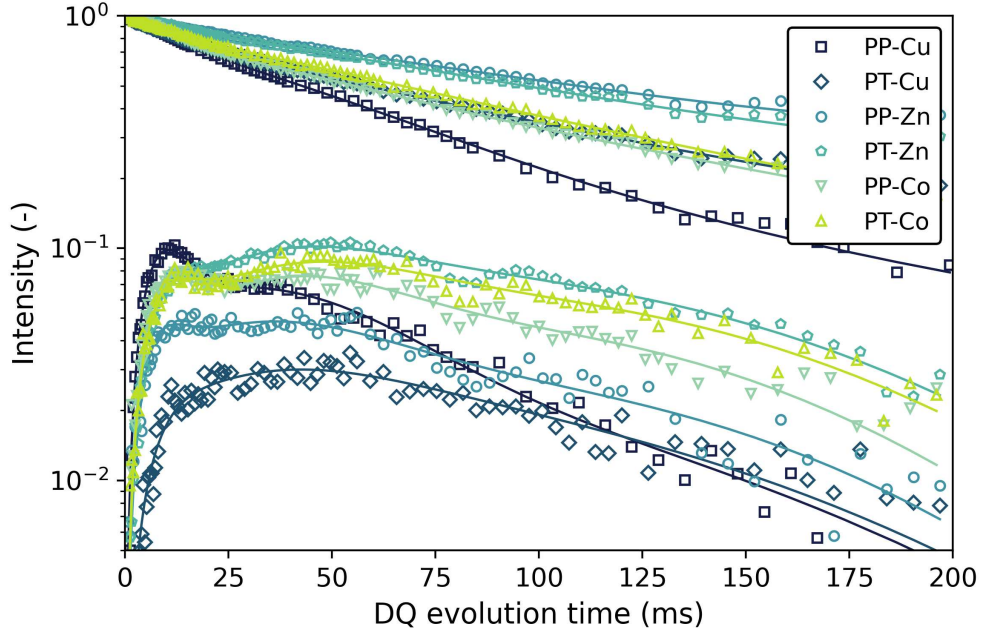


Figure 6.27: Experimental data sets of all samples obtained from the MQ NMR experiment. The upper set of curves is the  $I_{\Sigma MQ}$  data, whereas the bottom set of curves is the  $I_{DQ}$  data. Used sample abbreviations are: "PP: DMPHEN/Phen" ; "PT: DMPHEN/TPy".

section 3.4.2) under the already previously justified assumption of 3 distinct connectivity motifs, being single links (SL), double links (DL) and higher order connectivity motifs (HOC) with all data sets shown in Figure 6.27. As can be seen from the exponential tail of  $I_{\Sigma MQ}$  toward long  $\tau_{DQ}$ , all samples show a significant contribution of protons attached to the isotropic material prior to correction using the saturation recovery data. However, after correction, a rather clear pattern is visible, as shown in Figure 6.28. Both samples containing  $\text{Cu}^+$  as a coordination center essentially show no primary loop defect fraction, and the final result even shows signs of slight overcompensation due to the relatively large error bars arising from the saturation recovery decomposition. This shows that  $\text{Cu}^+$  tends to mainly form heteroleptic crosslinks between DMPHEN-functionalized tPEG pre-

Table 6.4: Experimental results obtained from the saturation recovery experiment. Here,  $f_{\text{poly}}$  denotes the polymer fraction,  $T_{1,\text{poly}}$  is the longitudinal relaxation time of the polymer,  $f_{\text{solv}}$  is the fraction of the solvent, and  $T_{\text{solv}}$  is the longitudinal value for solvent.

Sample	$f_{\text{poly}}$	$T_{1,\text{poly}}$ (s)	$f_{\text{solv}}$	$T_{\text{solv}}$ (s)
DMPHEN/Phen/ $\text{Cu}^+$	$0.80 \pm 0.07$	$289 \pm 33$	$0.20 \pm 0.07$	$1500 \pm 527$
DMPHEN/TPy/ $\text{Cu}^+$	$0.69 \pm 0.06$	$174 \pm 23$	$0.31 \pm 0.06$	$1808 \pm 608$
DMPHEN/Phen/ $\text{Zn}^{2+}$	$0.33 \pm 0.03$	$533 \pm 61$	$0.67 \pm 0.03$	$5860 \pm 472$
DMPHEN/TPy/ $\text{Zn}^{2+}$	$0.50 \pm 0.02$	$432 \pm 30$	$0.50 \pm 0.02$	$6109 \pm 528$
DMPHEN/Phen/ $\text{Co}^{2+}$	$0.88 \pm 0.07$	$461 \pm 45$	$0.12 \pm 0.07$	$2709 \pm 2410$
DMPHEN/TPy/ $\text{Co}^{2+}$	$0.89 \pm 0.04$	$475 \pm 27$	$0.11 \pm 0.04$	$3878 \pm 2034$

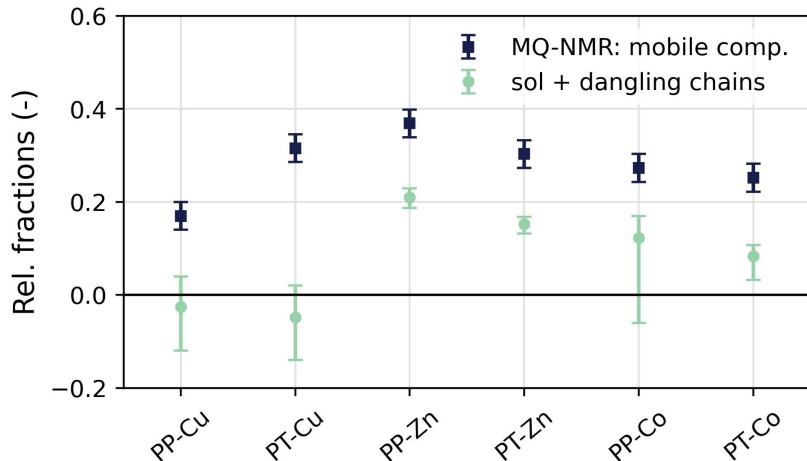


Figure 6.28: Shown are both the mobile/isotropic component estimated from the MQ NMR experiment, as well as the extracted fraction of sol, dangling chains and primary loop defects after data reduction using the saturation recovery data. Used sample abbreviations are: "PP: DMPHEN/Phen" ; "PT: DMPHEN/TPy".

cursors and tetraPhen/tetraTPy-functionalized tPEG precursors by achieving the required tetrahedral or trigonal-bipyramidal coordination geometry. For both  $\text{Co}^{2+}$  and  $\text{Zn}^{2+}$  a significant amount of primary loops was found even after data reduction, indicating that they do not prefer the formation of heteroleptic complexes, as both prefer a higher coordination number. Therefore, it is hypothesized that the partial formation of heteroleptic complexes is driven by a (weaker)  $\pi$ -stabilisation incentive rather than a preference for the coordination geometry. The final MQ NMR data shows a slight but systematic difference ( $f_{\text{def,Zn}^{2+}} > f_{\text{def,Co}^{2+}}$ ) in the overall primary defect fraction, which, however, is not reproduced by a simultaneous increase in the plateau modulus measured by Mostafa Ahmadi (see ref. [152], where  $G_{\text{Zn}^{2+}}^* \approx 2.8 \text{ kPa}$  and  $G_{\text{Co}^{2+}}^* \approx 2.3 \text{ kPa}$ ). It is assumed that the overall measurement error is underestimated (leading to larger error bars) or that the basic assumption of a well-defined order plateau of the OACF (see section 3.3) - detectable by a plateau in the rheological data - is not fulfilled. As shown in ref. [152], the  $\text{Zn}^{2+}$ -system shows a rubbery plateau value only up to about 100 ms, while the MQ NMR data is acquired for a slightly longer timescale of about 400 ms. Therefore, for the  $\text{Zn}^{2+}$  system, a necessary assumption is not satisfied for the extraction of RDC values from the MQ NMR experiment, rendering the corresponding parameters questionable.

Concerning the estimated RDC values, as well as the corresponding proton fractions, the following statements can be made: the highest RDC value that can be observed is within 20 – 40 Hz, which is in perfect agreement with the values obtained from Lange et al. [23] on the 10 kDa tPEG-NH2 'Sakai' system (40 – 70 Hz), considering the difference in molecular weight. Therefore, the existence of ion-mediated clusters found in a rather similar system discussed in section 6.4, can be excluded and the correspondence of this extracted component with the SL fraction can be confirmed. The second component extracted spans RDC values from 6 – 10 Hz, which is a factor of 3-4 lower than the RDC values of the SL fraction. Again, this is in agreement with the expectations, confirming that indeed the second-order



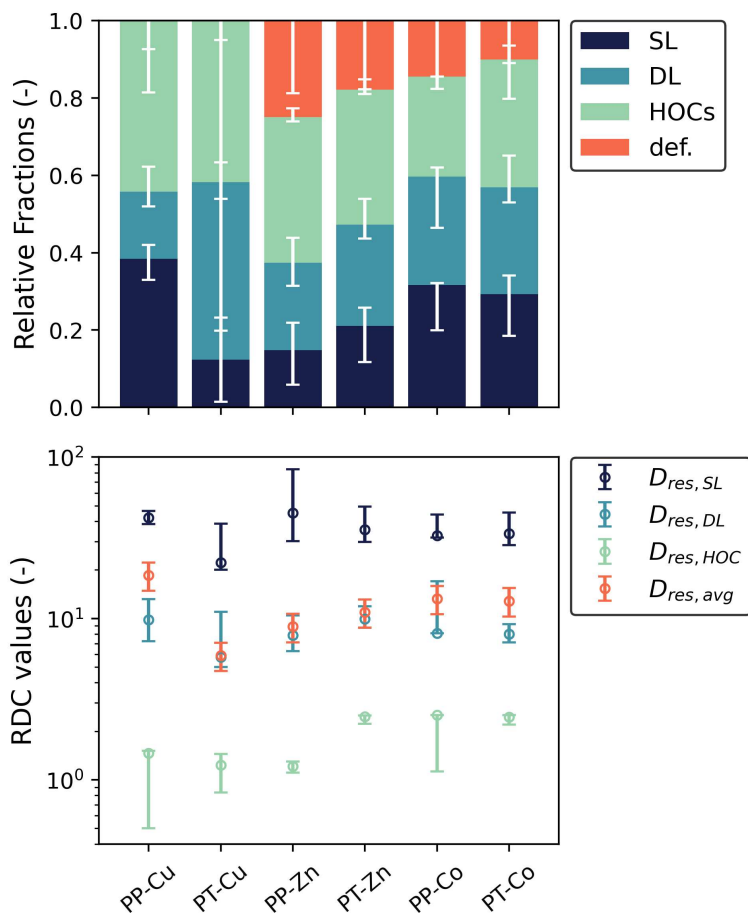


Figure 6.29: Residual dipolar coupling values (top) and corresponding proton fractions of connectivity motifs (bottom) that were extracted from the data shown in Figure 6.27. Used sample abbreviations are: "PP: DMPHEN/Phen" ; "PT: DMPHEN/TPy".

loop structure (DL) or structures with similar orientational mobility are measured. Finally, a third barely distinguishable component is extracted with RDC values spanning the range of 1 – 3 Hz. Due to its uncertain nature, as well as the increasing complexity of connectivity motifs towards higher-order defect structures, it is not further discussed. A comparison of the RDC values with the rheologic moduli (see [152] for details) reveals that the difference in plateau moduli ( $G = 5$  kPa for DMPHEN/Phen/ $\text{Cu}^+$  and  $G = 2.3$  kPa for DMPHEN/TPy/ $\text{Cu}^+$ ) is consistent with the ratio of nearly 3 that is found in the proton fraction-weighted average RDC values, which confirms the well-known proportionality of  $G \propto D_{res,avg}$ . The reduced capacity of the  $\text{Co}^{2+}/\text{Zn}^{2+}$  ions to form heteroleptic complexes is found not only in MQ-NMR but also verified by rheological measurements, which yields another agreement. However, the difference in the average RDC values of the  $\text{Co}^{2+}/\text{Zn}^{2+}$  samples itself is not consistent with rheological experiments and expectations, with the only explanation being the relatively large error bars of the MQ NMR measurements. Interestingly, despite the differences in the number of primary loop defects, nearly no systematic differences were found in the distribution of connectivity motifs. While it is expected that the preferences in certain coordination geometries do not directly influence

the SL/DL ratio, it is a rather surprising conclusion that the (non-)existence of primary loop defects does not significantly influence the overall connectivity distribution. Therefore, the hereby presented system allows for an interesting tuning mechanism of the fraction of primary loop defects by simply changing the coordination center ion of the used end-linking chemistry while leaving the rest of the network architecture untouched. In terms of defect engineering of the rheological properties, the resulting effective mesh sizes, and permeability properties, this system provides an interesting option because of the separation of concerns driven by the used chemistry.



## Chapter 7

# Structural investigation of ACPNs

So far, all gels presented in this thesis were investigated only by MQ NMR which studies the local chain anisotropy. Thus, it does not allow for direct conclusions on scales larger than the crosslink and only (limited) indirect conclusions by predicting changes in the macroscopic structure based on the RDC value as a microscopic observable. While it was shown that e.g., the proton fraction of small-scale clusters embedded in a polymer matrix (see section 6.4) can be quantified, information on length scales and aggregation numbers cannot be obtained. Therefore, two methods, being small-angle x-ray scattering (SAXS) and Pulsed-Field gradient NMR (PFG-NMR) that are able to quantify length scales determining macroscopic properties such as permeability are used to characterize the amphiphilic tPEG-tPCL system described before. For a description of the system, the reader is referred to section 5.1.1, while for an investigation of the chain-level connectivity motif distribution in good and theta solvent the reader is referred to section 6.2. It should be noted that most of the content of this chapter has been published in ref. [74].

### 7.1 SAXS on swollen polymer networks

#### 7.1.1 Estimation of correlation blob size in PEG-PCL networks in good solvent conditions

Most of the applications that make use of diffusion of probe molecules inside a polymer matrix rely on a controlled diffusion coefficient. In some publications (see e.g., refs [141, 165, 166]) the corresponding polymer length scale is expressed in terms of a so-called mesh size, whose definition is rather ambiguous and may relate to length scales spanning the whole range from the chain correlation blob  $\xi_c$  up to the geometrical mesh expressed as the average center-center distance of two neighboring precursors. Here, the investigated ACPNs will be characterized in terms of the correlation blob size  $\xi_c$ . For that, a set of tPEG-tPEG co-networks and a set of amphiphilic tPEG-tPCL co-networks were synthesized at different preparation concentrations  $c_{\text{prep}}$  in  $d_8$ -toluene (using precursors provided by Carolin Bunk, see section 5.1.1) and measured as-prepared using the experimental setup described in section 5.2.

Generally, the curves obtained by SAXS consist of a characteristic superposition of functions arising from the scattering of different moieties on different length scales. In a common

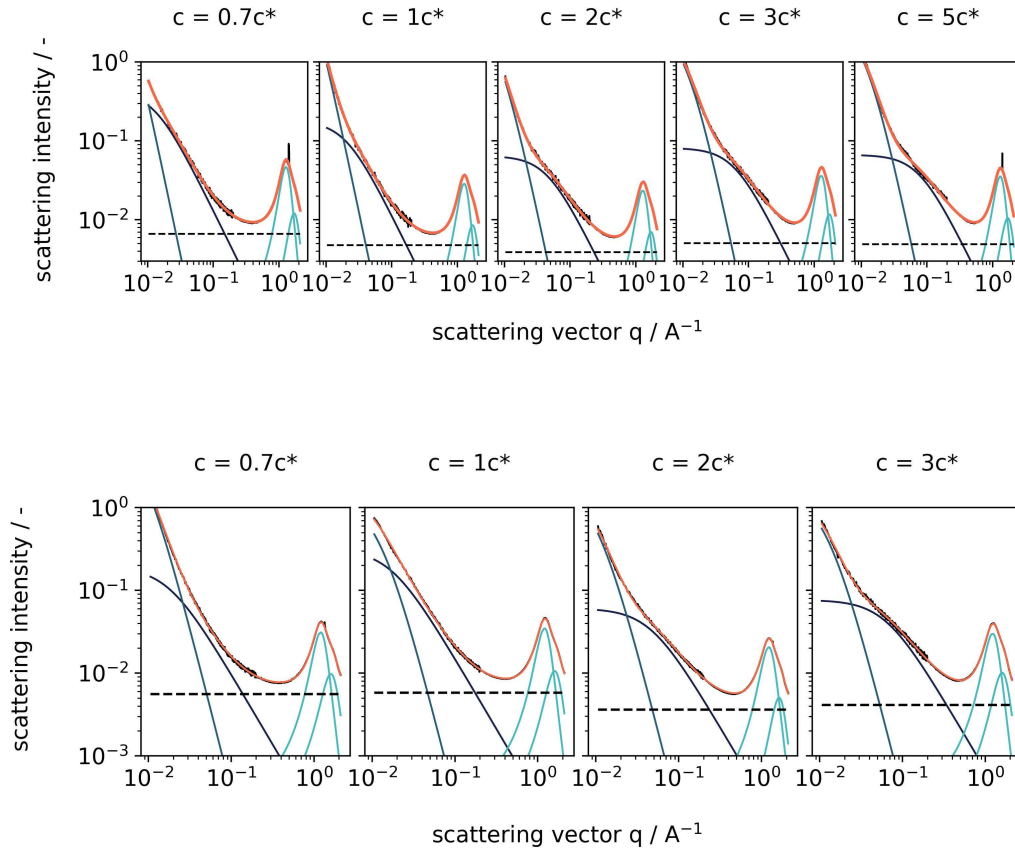


Figure 7.1: Scattering curves (combined SAXS+WAXS) were obtained for various ACPNs (top row) and PEG-PEG networks (bottom row) in a good solvent ( $d_8$ -toluene) at various concentrations. The solid lines represent the complete fit in accordance with Equation 7.1, along with the corresponding components. Reprinted with permission from ref. [74]. Copyright 2023 American Chemical Society

good solvent, the following model function is used:

$$I(q) = I_{bg} + I_{DB} + I_{OZ} \quad (7.1)$$

For more details on the specific functions, the reader is referred to section 4.2.1. Here, the length scale  $\Xi$  of frozen fluctuations is described by a Debye-Bueche function  $I_{DB}$  [140] following eq. 4.11. It should be noted that the relevant length scale is not fully accessed by SAXS and only the "tail" of  $I_{DB}$  can be fitted. Therefore, the length scale  $\Xi$  obtained is only qualitative in nature and a lower estimate. However, due to the strong contribution to the overall signal, it is still needed. The thermal fluctuations (or the correlation blob) is characterized by  $\xi_c$  and is modeled by a generalized Ornstein-Zernike function [57] with the good solvent exponent  $\nu = 0.588$  (leading to an overall dependence of  $q^{-1.7}$ , see eq. 4.10). Lastly, the incoherent background scattering is modeled by a constant function  $I_{bg} = \text{const.}$

As shown in Figure 7.1, the characteristic length scale of interest ( $\xi_c$ ) is clearly identifiable for most samples and can be deconvoluted using eq. 7.1. However, for the PEG-PEG

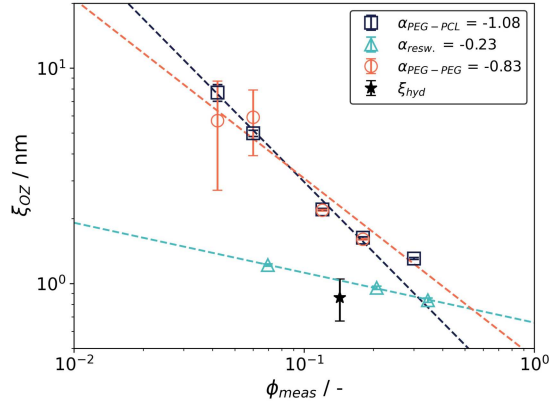


Figure 7.2: The correlation length  $\xi$  was determined through the evaluation of different networks measured in a good solvent and as-prepared (or reswollen to preparation condition) in dependence on the preparation condition and fits with power laws  $\phi^\alpha$ . The value for  $\xi_h$  displayed in this Figure will be discussed later on in section 7.2.2. Reprinted with permission from ref. [74]. Copyright 2023 American Chemical Society

networks at  $c = 0.7c^*$ , the distinction between  $I_{OZ}$  and  $I_{DB}$  is ambiguous, leading to a larger error bar. Figure 7.2 shows the result of the fitting procedure, revealing a surprisingly low scatter among the data obtained. The data is fitted using a power-law model  $\xi_c(\phi) = a \cdot \phi^\beta$  (with  $\phi$  being the polymer fraction) as is expected for polymers in solution (see ref. [88] and eq. 2.23). For the PEG-PEG networks, a scaling exponent of  $\beta = -0.83 \pm 0.2$  is found and for the PEG-PCL networks a scaling exponent of  $\beta = -1.08 \pm 0.05$  is found. Although the scaling exponents may differ by 20%, the values of  $\xi_c$  at high  $\phi$  are perfectly overlaying, while differences at low  $\phi$  are within the given error bars, suggesting that both networks probably show no significant difference in their  $\xi_c$  values. Therefore, mixing inhomogeneities based on the existence of two different precursors (tPEG and tPCL) are very unlikely.

According to ref. [88], for a semi-dilute solution of polymer chains in a solvent, an exponent of  $\beta = -0.75$  is expected. Although  $\beta_{\text{PEG-PEG}}$  is still within that range, the value of  $\beta_{\text{PEG-PCL}}$  is considerably larger, possibly indicating an additional concentration dependence whose origins have yet to be found. Comparing the values obtained for  $\xi_c$  with the same length scale extracted by Matsunaga et al. [22] on the tPEG-water system ( $\theta$ -solvent,  $M_w = 10$  kDa), a significant discrepancy is found. Here, at a preparation concentration of  $c = c^*$  ( $\phi^* = 0.06$ ) values of  $\xi_c = 4.9 \pm 0.2$  nm and  $\xi_c = 4.7 \pm 2.0$  nm are found for the PEG-PCL and PEG-PEG networks, respectively, whereas from Matsunaga et al. an interpolated value of  $\xi_c \approx 2.2$  nm and a value of  $\beta = -1.23$  can be obtained. Although these two values are not directly comparable (owing, e.g., to the different solvent qualities;  $\chi = 0.485$ ), they may serve as a rough guideline that indicates a significant increase for our systems. Reasons for this may include an increase in the overall amount of inhomogeneities present in our system. A more detailed study of the reasons is not possible due to several factors; e.g., the length scale accessible with SAXS is not enough to model the frozen fluctuations. For a more direct comparison, small-angle neutron scattering (SANS) would be needed to access the length scale, while also allowing for a contrast

variation to extract the geometrical mesh size (defined as the center-center distance between neighboring star precursors).

Lastly, a set of SAXS experiments was conducted to follow up on the results obtained in section 6.2.3, which implied a post-curing effect, observed in the equilibrium degree of swelling and RDC values, in bulk due to the spatial proximity of a small amount of open chain ends. Here, a set of PEG-PCL networks was prepared in  $d_8$ -toluene at 3 different concentrations, being  $c_{\text{prep}} = [1c^*, 3c^*, 5c^*]$  and subjected to a drying+reswelling cycle. It was observed that the original degree of swelling was not exactly reached for all three networks (because  $Q_{\text{eq}}$  being lower after drying), however, the values reached are at least close (as observed in the small shift of  $\phi$  for these three networks in Figure 7.2). It is observed that the correlation blob strongly decreases by a factor of 4 – 5 at  $c = c^*$  and a factor of 2 at  $c = 3c^*$ , resulting in a strong shift of the exponent  $\nu$  to lower values ( $\nu = -0.23$ ). However, it is not clear whether this shift really indicates a strong decrease in  $\xi_c$ , or is a result of the strongly stretched chains possibly having a different Ornstein-Zernike exponent  $\nu = \nu_{\text{stretch}}$ , resulting in a second contribution to  $I_{\text{OZ}}$ . As measurements do not allow a quantification of  $\nu_{\text{stretch}}$  (since the overall signal can be fitted using only a single  $I_{\text{OZ}}$ ), it must be assumed that  $\nu = 0.588$  for all chain species. Therefore, the values of  $\xi_c$  found in that evaluation serve only as an apparent measure with an underlying systematic error. Again, contrast-matched SANS is needed for more detailed statements on  $\nu$ .

### 7.1.2 Characterisation of the phase-separated structures under selective solvent conditions

Additional SAXS measurements were performed on a set of PEG-PCL ACPNs that were dried and reswollen in a poor solvent ( $\text{D}_2\text{O}$ ) to equilibrium to study the microphase separation (MPS) behavior of these gels. A priori, it is not clear what kind of phase-separated structure will emerge due to the topological constraints imposed by the network. Although PCL precursors will undergo macroscopic phase separation in  $\text{D}_2\text{O}$ , the crosslinked PCL precursors have a decreased range of motion and therefore phase separation may be inhibited or only occur on a local scale (MPS, leading to a decreased degree of swelling  $Q > 1$ ).

Comparing the SAXS curves observed in  $\text{D}_2\text{O}$  (poor solvent) with the curves obtained in  $d_8$ -toluene (good solvent), which were discussed in the previous section, a significant difference is found in the form of a strong peak at about  $\approx 0.1 \text{ \AA}$  at all concentrations (see Figure 7.3 for an example). The observed curve is again supposed to be a superposition of different contributions and reads as follows:

$$I(q) = I_{\text{bg}} + I_{\text{DB}} + I_{\text{OZ}} + I_{\text{MPS}} \quad (7.2)$$

This equation is similar to eq. 7.1 and uses the same function. The only, however dominant, difference is found in  $I_{\text{MPS}}$ , which is used to describe the peak arising from the MPS of the PCL chains. In this work, two different models, the Teubner-Strey model for MPS in emulsions (TS) and the hard-sphere model of Kinning and Thomas (KT), will be used

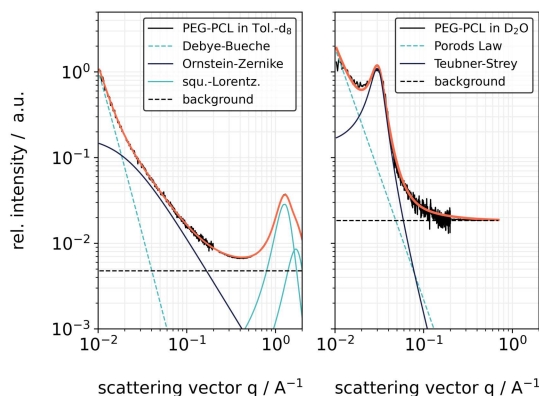


Figure 7.3: Exemplary scattering curves, along with their corresponding evaluation, for the investigated PEG-PCL ACPN in a non-selective solvent (left; merged SAXS+WAXS) and a selective solvent (right; SAXS). Reprinted with permission from ref. [74]. Copyright 2023 American Chemical Society

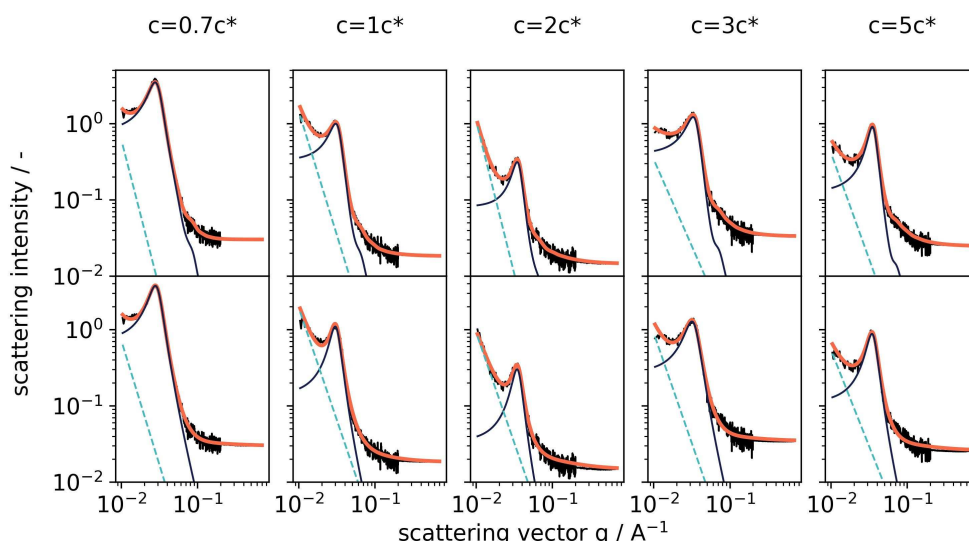


Figure 7.4: Scattering curves (only SAXS) of ACPN at various preparation concentrations, swollen in water, with fitting results displayed as lines. In the top row, fits of the structural peak are shown as a black solid line using the KT model, and in the bottom row, the same data is fitted to the TS model. Reprinted with permission from ref. [74]. Copyright 2023 American Chemical Society

and the results will be compared. For the theoretical foundation used in both models, the reader is referred to section 4.2 and references therein. A visual comparison of the fits and the data obtained for all concentrations is found in Figure 7.4. Lastly, it should be noted that while  $I_{OZ}$  is necessary for the evaluation, its overall value is poorly defined and is therefore not subject to any evaluation. Reasons for this are on the one hand the fact that the network chains belonging to the PCL are not expected to participate in the regular network structure, while on the other hand no singular  $\xi_c$  value is expected, as the MPS may lead to a radial dependence  $\xi_c(r)$  with  $r$  being the distance from the PEG chain to the cluster.

Application of the TS model yields two different length scales reflecting the distance be-

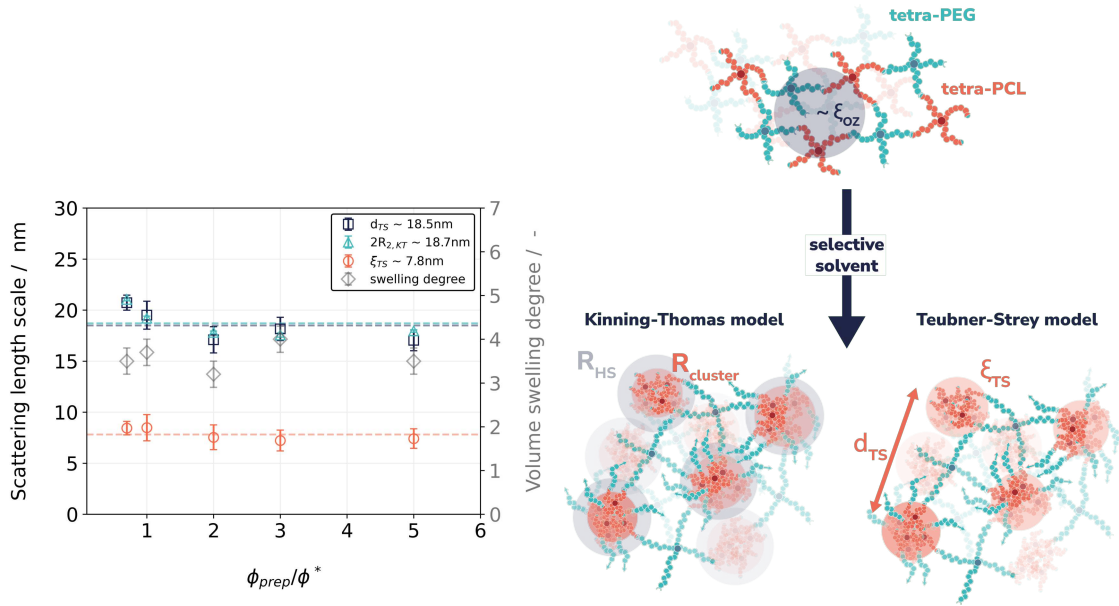


Figure 7.5: Left panel: Overview of the length scales obtained, including domain distances (denoted  $d$ ) and the domain-associated correlation length scale ( $\xi$ ), calculated using equations 4.14 and 4.15 for the Teubner-Strey (TS) and  $d = 2R_1$  for the Kinning-Thomas (KT) model. Right panel: Tentative model representation of the MPS (Microphase Separation) of the tPEG-tPCL ACNP under investigation, as viewed through the two models employed for SAXS data analysis. Please note that, for the sake of simplicity, some chain ends are either not depicted or are represented with arrows. Reprinted with permission from ref. [74]. Copyright 2023 American Chemical Society

tween the scattering centers ( $d_{TS}$ ) and an associated decay length  $\xi_{TS}$  (see eq. 4.14 and 4.15). While the distance  $d_{TS}$  can be interpreted rather straightforwardly as an average distance between the scattering moieties, the interpretation of the decay length  $\xi_{TS}$  is rather ambiguous. It yields a length scale associated with the range of constructive interference of the radial oscillations  $g(r)$  belonging to the scatterers, which in some works is compared with the size of the scatterer [141]. As, however, both length scales are determined in terms of correlations functions that do not show a Heaviside-like jump but a continuous decay, the extent of accuracy of these extracted length scales is not clear. It is observed that both values do not change significantly across the whole range of preparation concentrations and yield values of  $d_{TS} \approx 18.5$  nm and  $\xi_{TS} \approx 7.8$  nm respectively (see Figure 7.5 for results). Here, a simplistic model of bulk-like PCL clusters ( $Q_{PCL} = 1$ ) interconnected by PEG chains ( $Q_{PEG} = 2Q_{eq} - 1$  due to the PCL phase accommodating hardly any solvent, thus  $Q_{PCL} = 1$ ) is chosen to assess the distances obtained. In this model, the maximum distance allowed should equal the length of a stretched PEG chain plus a collapsed PCL chain that will be found within the spherical cluster. With an equilibrium degree of swelling observed of approximately  $Q_{eq} \approx 4$  (and therefore  $Q_{PEG} \approx 7$ ) and the characteristic properties of the PEG chain ( $b = 0.38$  nm,  $C_\infty = 4$ ,  $N=113$  for  $M_w = 10$  kDa) [167, 168], one can calculate the mean-squared end-to-end distance  $R_{ee}$  of a PEG chain in bulk using eq. 2.4 and extrapolate it to a swelling degree of  $Q = 7$  as follows:

$$R_Q = Q^{1/3} \cdot R_{ee} = 15.8 \text{ nm}$$

For the fully stretched PEG chain ( $R = l_K$ ) a similar calculation using  $l_K = bN$  yields  $l_K = 40.6 \text{ nm}$ , which easily accommodates the observed distance of  $d_{\text{TS}} = 18.5 \text{ nm}$ . Therefore, it can be assumed that the PEG chains will be slightly stretched, but are not close to their contour length. As discussed above,  $\xi_{\text{TS}}$  cannot be used as an accurate estimate of the size of the domain, which is why the distance and the degree of swelling measured will be used. By assuming a certain spatial distribution of the clusters and the corresponding packing density  $\rho$ , e.g., simple cubic lattice (scc,  $\rho = 0.5236$ ) or a close-packing of spheres (fcc,  $\rho = 0.7506$ ), one immediately finds that both do not reflect the packing density as determined by the equilibrium degree of swelling ( $\rho = 1/8 = 0.125$ ). Hence, it is concluded that, under the assumed distribution, the spheres will not be in direct contact as a result of their smaller size. The respective shrinking factors can be calculated as  $k_{\text{scc}} = (0.125/0.5236)^{1/3}$  and  $k_{\text{fcc}} = (0.125/0.7406)^{1/3}$ , which immediately results in a quantitative relation of cluster distance ( $d_{\text{TS}}$ ) and the desired cluster radius  $r_{\text{cluster}}$ . For both models, the following values are found:

$$r_{\text{cluster}} = \begin{cases} 0.31 d_{\text{TS}} = 5.73 \text{ nm} & \text{for scc arrangement} \\ 0.28 d_{\text{TS}} = 5.18 \text{ nm} & \text{for fcc arrangement} \end{cases}$$

With  $r_{\text{cluster}}$  being estimated, one can calculate the respective aggregation numbers  $AN$  (number of PCL stars in a cluster) as

$$AN = \frac{\frac{4}{3}\pi r_{\text{cluster}}^3}{M_{\text{star}}/(\rho_{\text{star}} \cdot N_A)} \quad (7.3)$$

$$\approx \frac{r_{\text{cluster}}[\text{nm}]^3}{3.81 \text{ nm}^3}$$

For the PCL stars, a molecular weight of  $M_{\text{star}} \approx 11\,000 \text{ g mol}^{-1}$  as well as a density of  $\rho_{\text{star}} = 1.145 \text{ g cm}^{-3}$  are assumed. Using this, the aggregation numbers for both cases can be calculated as  $AN_{\text{scc}} = 49$  and  $AN_{\text{fcc}} = 36$ . Therefore, the TS model alone is not suitable for determining aggregation numbers, as specific assumptions on the spatial configuration need to be made, whose small differences in  $r_{\text{cluster}}$  amplify due to the fact that  $AN \propto r_{\text{cluster}}^3$ . To aid the estimation, BFM simulations on this specific system were performed by Reinhard Scholz and Michael Lang<sup>i</sup>, yielding an independent estimate for  $r_{\text{cluster}}$  and  $AN$ . As shown in Table 7.1, both values show a slight dependence in preparation concentration that is not captured by the experiments. So far, it is not clear whether experimental issues (such as post-curing during drying) or simulation issues (e.g., no reliable literature values for  $\chi_{\text{PCL-H}_2\text{O}}$  are found, but the cluster size has a dependence on  $\chi_{\text{PCL-H}_2\text{O}}$ ) are the cause of this slight deviation. However, the obtained radii of gyration (with a slight polydispersity) of the PCL clusters (4.7 – 6.3 nm) are in agreement with both calculated values, while the aggregation numbers are too small by a factor of  $\approx 2$ . Reasons for this may

<sup>i</sup>Reinhard Scholz, Michael Lang - Leibniz-Institut für Polymerforschung Dresden e. V., Hohe Str. 6, 01069 Dresden, (Germany)



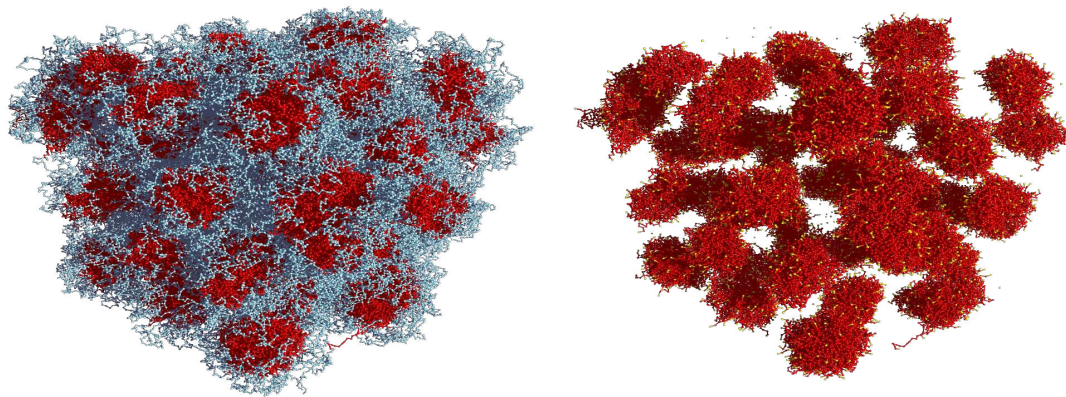


Figure 7.6: Snapshot of the simulated microphase-separated PEG-PCL system in a poor solvent, investigated using BFM simulations for  $\phi = 3\phi^*$ . In the left panel, all simulated monomers are visible, with PEG chains in light blue and PCL chains in red. In the right panel, PEG chains are made invisible, revealing the ellipsoidal shape of the PCL domains. The crosslinking groups (outermost monomer of the PEG star branches) are highlighted in yellow, indicating their predominant location at the outer shell of the PCL cluster. Reprinted with permission from ref. [74]. Copyright 2023 American Chemical Society

be the anisotropic shape of the clusters that is easily detected by the BFM simulations but cannot be extracted from the scattering data without assuming more complicated models, which in turn may lead to overfitting issues. Nevertheless, a snapshot of the simulation (see Figure 7.6) confirms the general assumptions made for the calculations ( $Q_{\text{PCL}} = 1$  and isolated spheres/ellipsoids with a PEG matrix in-between).

Table 7.1: Selected real-space simulation results for different preparation concentrations  $\phi_0$  normalized by  $\phi^*$ .  $\langle N \rangle$ : average number of stars in the clusters;  $\sigma$ : distribution width (polydispersity) given by  $\langle N^2 \rangle / \langle N \rangle^2$ ;  $R_g$ : cluster radius of gyration;  $l_{xyz}$ : relative axis length after projection onto an ellipsoid, quantifying the cluster anisotropy. Reprinted with permission from ref. [74]. Copyright 2023 American Chemical Society

$\phi_0/\phi^*$	$\langle N \rangle$	$\sigma$	$R_g$ (nm)	$l_x : l_y : l_z$
1	17.39	1.15	4.69	1.42 : 1.17 : 1
2	20.52	1.16	5.16	1.66 : 1.20 : 1
3	24.49	1.17	5.70	1.86 : 1.24 : 1
4	24.70	1.26	6.32	2.02 : 1.22 : 1

An alternative evaluation of the same scattering data can be performed using the model of Kinning and Thomas (KT), which assumes a hard-sphere form factor of radius  $R_1$  for the PCL clusters and a soft repulsive corona of radius  $R_2$  from a PEG phase of higher concentration that surrounds the clusters. Although it is assumed that  $R_2$  does not participate in the scattering (no contrast), it provides the distance between the spheres needed for the Percus-Yevick hard-sphere structure factor. Evaluation using the KT model yields nonphysical values of  $R_1 = 9$  nm and  $R_2 = 9$  nm (with a log-normal distribution parameter of  $\sigma = 0.3 - 0.4$ ), because both values seem to converge towards each other ( $R_1 \approx R_2$ ) suggesting that the radius of the repulsive sphere and the inner PCL cluster converge towards



each other.

Reasons for this peculiarity may be related to the fact that the "invisible" PEG corona may, in fact, have a scattering contrast with a radial dependence, as the PEG chains emerging from the PCL clusters could be interpreted as a brush structure with decreasing density with increasing distance from the core. This may lead to an overestimate of the  $R_1$  radius, thus leaving no possibility to determine the cluster size directly. Assuming the opposite ( $R_1$  as the correct radius of the PCL spheres and a vanishing  $R_2$ ) results in a strong contradiction, as the observed swelling degree of  $Q_{\text{eq}} \approx 4$  indicates a (semi-)diluted system of PCL clusters (volume fraction of  $f = 0.125$ ), while the above-mentioned assumption indicates spheres in close or direct contact with each other. Therefore, it is more reasonable to assume an overestimated  $R_1$  and continue using  $R_2$  as the repulsive sphere radius, resulting in a distance between the clusters of  $d_{\text{KT}} = 2R_2$ . Taking into account that  $d_{\text{KT}} \approx d_{\text{TS}}$ , this assumption would be in accordance with the results obtained from the TS model.

Additionally, it should be noted that the Percus-Yevick structure factor assumes a continuous spatial distribution of clusters starting from a (minimal) critical distance  $R^*$ , which may not be fulfilled due to the topological constraints imposed by the interconnected PEG chains. Lastly, the aforementioned BFM simulation results indicate a non-spherical structure of the PCL clusters that for high concentrations even becomes highly ellipsoidal (see Table 7.1), which cannot be fitted using more elaborate models due to limitations in the data quality. Given these limitations, it is surprising that both models are able to yield a reasonable overlap (under the aforementioned strong assumptions) despite being fundamentally different.

## 7.2 Diffusion of probe molecules inside a polymer matrix

In this section, the PEG-PCL networks will be characterized using pulsed-field gradient NMR (PFG-NMR, see section 3.6 for a theoretical background) in order to understand its transport capacities for probe molecules of different sizes and the effect of microphase separation (MPS) on it. Therefore, two sets of probe molecules, being linear polystyrenes (PS) and linear dextrans/polysaccharides (PSC), will be characterized in their respective solvents ( $d_8$ -toluene and  $D_2O$ ) and after swelling the network in the solution. Results will be analyzed using a simple colloidal diffusion model (neglecting effects of polymer dynamics on the probe molecule chain) and a more realistic scaling law model developed by Michael Lang. Most results of this chapter, with the exception of the colloidal model, are published in [74].

### 7.2.1 Viscometric and PFG-NMR measurements of probe molecules in solution

Initially, probe molecules were studied in 5wt% solutions (which will be equivalent to the concentrations used later on) using PFG-NMR without the surrounding polymer network to obtain reference values for diffusion coefficients at the given concentrations, while additionally confirming that the concentrations used do not yet influence diffusivity through

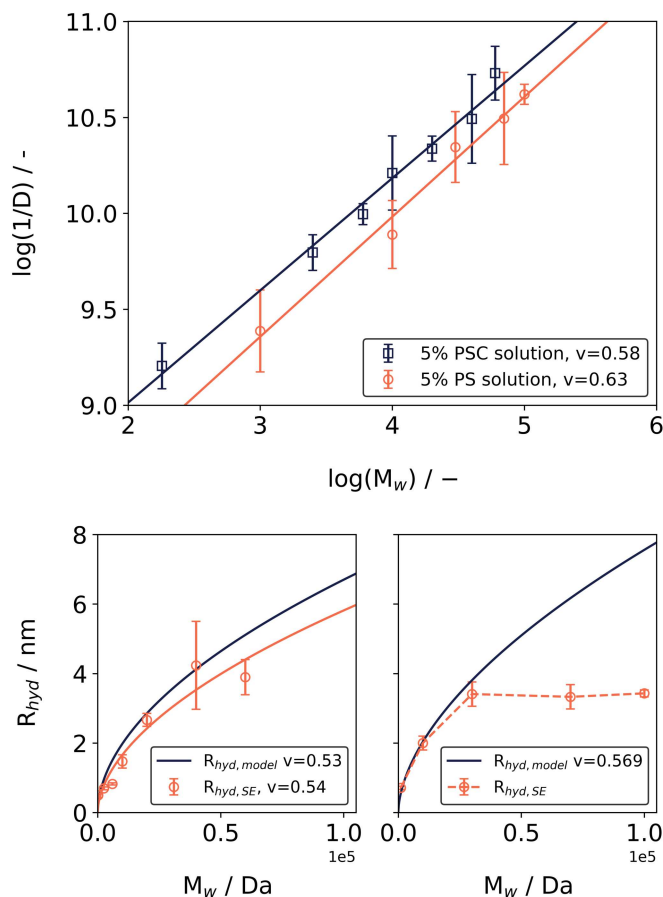


Figure 7.7: Top: In this log-log plot, the relationship between the inverse diffusion coefficient  $D$  in  $\text{m}^2\text{s}^{-1}$  and the molecular weight  $M_w$  in 5 wt% solutions of PSCs and PSs is presented. The data is fitted using equation 2.28, resulting in exponents of  $\alpha = 0.58 \pm 0.03$  for PSCs in  $\text{D}_2\text{O}$  and  $\alpha = 0.63 \pm 0.04$  for polystyrenes in  $d_8$ -toluene. Reprinted with permission from ref. [74]. Copyright 2023 American Chemical Society

polymer-polymer interactions. Therefore, 5wt% solutions of PSCs in  $\text{D}_2\text{O}$  and PS in  $d_8$ -toluene were prepared and diffusion coefficients obtained at  $T = 30^\circ\text{C}$  using the STE sequence (see section 5.2 for technical details on the spectrometer used).

Inverse logarithmic diffusion coefficients were plotted over the logarithmic molecular weight  $M_w$  (as provided by the supplier) in the top panel of Figure 7.7. The data was fitted to a simple power law model  $D \propto M_w^{-\alpha}$  (see eq. 2.28). For the PSCs an exponent of  $\alpha = 0.58 \pm 0.03$  is found and for the PS probe molecules an exponent of  $\alpha = 0.63 \pm 0.04$  is found. While  $\alpha_{\text{PS}}$  overlaps with other works (using PFG-NMR among other things) [169, 170], a slight deviation for  $\alpha_{\text{PSC}}$  in comparison to Wallace et al. is found [171] (again, using PFG-NMR to measure the diffusion coefficients). Nevertheless, the hereby-obtained values of  $\alpha$  match the scaling law expected from theoretical models of self-diffusion in good solvent and dilute solution [88].

An additional factor that has to be studied are polymer-polymer interactions due to the relatively high concentrations used for the solutions. As more dilute solutions are not feasible for PFG-NMR, they are instead studied by viscosimetry and comparing the hydrodynamic radii obtained in conjunction with PFG-NMR to predictions that were validated on dilute

solutions. For the PSCs, other works report overlap concentrations of e.g., 80 g/L and 120 g/L for a  $\approx 2000$  kDa dextran [172, 173]. As this is significantly larger in both, concentration and molecular weight, a concentration dependence of the diffusion coefficient due to surpassing  $c^*$  is not expected. However, for the PS probes an overlap concentration of  $c \approx 4.5$  wt% is reported in ref. [174] for a linear PS with a molecular weight of  $M_w = 48.8$  kDa. Therefore, a significant deviation from the Stokes-Einstein equation (see eq. 2.26) may be expected at least for the PS probes.

According to Braeckmann [175], the following relationship between the hydrodynamic radius  $R_h$  and the molecular weight  $M_w$  for PSC in water is expected:

$$R_h[\text{nm}] = 0.015(M_w[\text{kg mol}^{-1}])^{0.53 \pm 0.02} \quad (7.4)$$

This relationship was checked in the bottom left panel of Figure 7.7 using the measured viscosity  $\eta$  and the diffusion coefficient  $D$ , of the solutions and converting them to  $R_h$  using the Stokes-Einstein equation. It is found that the hydrodynamic radii are consistently smaller than predicted by eq. 7.4 which is in accordance with ref. [171]. Although Wallace et al. attribute this systematic difference to the presence of PSCs with lower molecular weight, the diffusion experiments conducted in this work (see Figure 7.8) show a straight slope, indicating a mostly monomodal distribution according to eq. 3.16. Additionally, Wallace et al. find a significantly lower exponent of  $\alpha$  supporting their argument, while here the expected exponent is retained. This observation would indicate a consistently smaller size of PSCs across all molecular weights or, alternatively, hint a significant amount of intramolecular branches that reduce  $R_h$ .

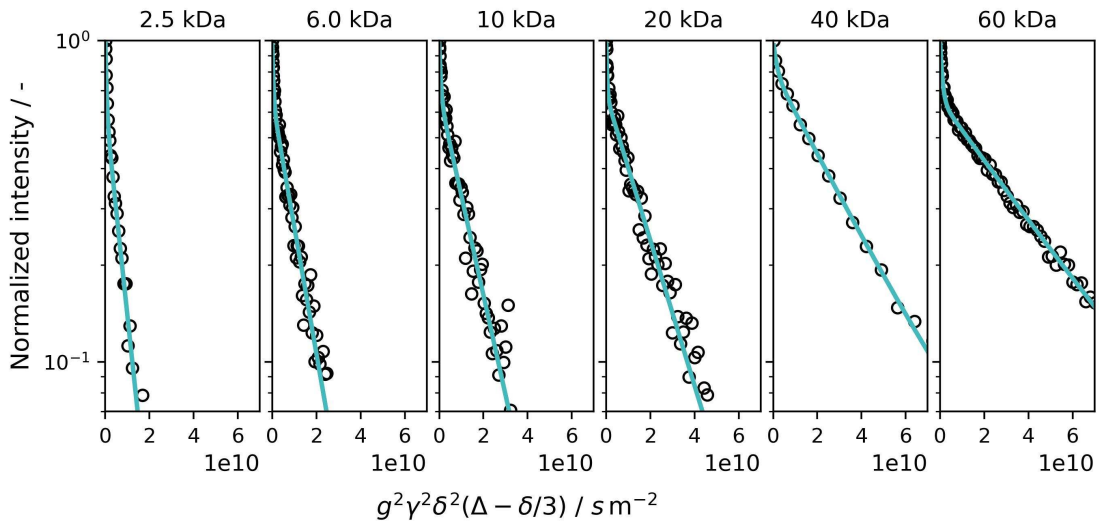


Figure 7.8: Diffusion decays obtained for PSC of different molecular weights (see plot titles). The bimodal diffusion decay arises from the overlap of the PSC resonances with the water resonance, thus the non-changing fast decay corresponds to water, whereas the more shallow slope is proportional to the diffusion coefficient of the respective PSC.

For the PS probes, a similar relationship  $R_h(M_w)$  was reported by Fetters et. al [176], which summarizes existing literature on hydrodynamic properties of PS in toluene, arriving at a

unified regression model for a variety of methods:

$$R_h[\text{nm}] = 0.0108(M_w[\text{kg mol}^{-1}])^{0.569} \quad (7.5)$$

As discussed, the diffusion data of the PS probes alone do not indicate any unusual behaviour with  $\alpha_{\text{PS}}$  matching the expected scaling law. However, the hydrodynamic radii obtained by using the measured viscosities in conjunction with eq. 2.26 shows an agreement with eq. 7.5 only for PS with a molecular weight up to  $M_w = 30$  kDa (see bottom-right panel of Figure 7.7). As discussed previously, for the measured PS molecules above 30 kDa the overlap concentration is exceeded, thus both polymer-polymer interactions as well as chain interpenetration effects are expected. As a result, literature values calculated by eq. 7.5 will be used as a reference for the hydrodynamic radius.

## 7.2.2 Diffusion inside a polymer matrix

With the probe molecules being characterized by PFG-NMR and viscosimetry in the previous section, this part will follow up by applying PFG-NMR to PEG-PCL gels swollen in solutions of probe molecules matching these conditions. Gels studied in selective solvent ( $\text{D}_2\text{O} + 5$  wt% PSC) are swollen to equilibrium, while gels studied in good solvent ( $d_8$ -toluene + 5 wt% PS) are fixed at  $Q = 5$ . While the aim was to have both set of gels at roughly the same degree of swelling, it was neglected that the "effective degree of swelling" for the selective solvent is much higher, as the PEG phase will accommodate as much solvent as possible, whereas the PCL will hardly accommodate any solvent. Hence, the effective degrees of swelling are  $Q = 7$  for the PEG phase in  $\text{D}_2\text{O}$  and  $Q = 5$  for the whole network in  $d_8$ -toluene.

In the following sections, an improved version of the standard evaluation procedure for PFG-NMR is presented and used to quantify the length scales that govern the diffusion processes for probe molecules within the PEG-PCL system using two different models. The first model will be a simplistic hydrodynamic model that assumes a colloidal probe within a network of a defined mesh size  $\xi_{\text{mesh}}$ , while the second model is motivated by polymer dynamics described in section 2.2.3 and defines the length scale of interaction as the hydrodynamic screening length  $\xi_h$ .

## Data evaluation

The common procedure for evaluating PFG-NMR data involves the localization of a suitable peak in the NMR spectrum and quantifying the changes in its height (or integrated area) across all gradient strengths  $g$  applied during the course of this experiment. As described in section 3.6, the resulting normalized decay can be fitted by a single exponential function  $I(b) = \exp(-b \cdot D)$ , with  $b$  being the reduced x-dimension, resulting in the diffusion coefficient  $D$ . In the case of multiple overlapping peaks associated to different species of respective diffusion coefficient  $D_i$ , this function can be modified to a multimodal approach with a proton fraction-weighted superposition. As shown in Figure 7.9, no well-isolated peaks are visible in the PEG-PCL system swollen in a solution of PSCs due to multiple reasons: Most importantly, the network itself behaves like a solid in the sense

of NM, meaning that the  $^1\text{H}$ - $^1\text{H}$  dipolar couplings are not fully averaged to zero as is expected for liquids. Instead, they display a residual value of about  $\approx 100$  Hz (as previously discussed in the DQ NMR section), leading to an additional broadening of the peaks of roughly  $\approx 0.25 - 0.5$  ppm. Additionally, the sample preparation of the gels (especially the drying and reswelling in a selective solvent) does not allow for a homogeneous filling of the sample in e.g., a tube or rotor, but only allows for solid pieces tightly packed inside the container. The additional broadening is empirically estimated to be of the size of  $\approx 0.5 - 1$  nm, resulting in a total broadening of the peaks beyond 1 ppm. Hence, the resulting NMR spectrum does not allow for any quantification of peaks belonging to the network itself, while additionally strongly overlapping any peaks from the 5 wt% of probe molecules. Therefore, the chemical resolution is (nearly) lost, and the simple approach of tracking peaks of a singular probe molecule fails in the case of PSC. However, for PS probes, the strong styrene resonance at 7.3 ppm is fortunately far enough from the network peaks (see [47] for a detailed HR-MAS spectrum and Figure 7.9d for a qualitative MAS spectrum), resulting in a strong enough separation to utilize the standard procedure. Due to the inapplicability of the common evaluation procedure for the PSC probes, a new procedure was developed, which will now be explained. The usual alternative evaluation procedure used for overlapping peaks is integration of the whole spectral region to evaluate the resulting multimodal decay using a regression with multiple exponential decays. However, even this procedure is barely possible in this case, as the overall intensity arising from the probes itself is, due to the concentrations used, very small in comparison to e.g., the network or even the solvent (which, despite being deuterated, usually still has a significant contribution of protons due to exchange processes). The algorithm (see Figure 7.9 for a pictorial representation on an example) starts with assuming that all contributions arise from either solvent, probe or network, therefore justifying the following regression model:

$$I(b) = a_{\text{solv}}I_{\text{solv}}(b, D_{\text{solv}}) + a_{\text{probe}}I_{\text{probe}}(b, D_{\text{probe}}) + a_{\text{net}} \quad (7.6)$$

Here,  $a_i$  are the normalized proton-weighted prefactors with  $a_{\text{solv}} + a_{\text{probe}} + a_{\text{net}} = 1$  and  $I_i = \exp(-bD_i)$  are the single-exponential decays for solvent and probe molecule respectively. As  $D_{\text{net}} \approx 0$  is observed, the network itself can be approximated by a constant offset. In a second step, the 2-dimensional PFG-NMR data set is divided into equal slices (with the width being e.g., 0.5 ppm) along the ppm dimension. Now, for each slice, the integral intensity will be evaluated according to eq. 7.6, yielding a set of parameters ( $a_i, D_i$ ) for each slice. For the procedure to be realized efficiently (as there can be  $> 20$  slices per sample), these steps are automated using Python 3.10 and the LMFIT library [154].

The advantage of this procedure lies in the fact that while the chemical resolution is "nearly" lost (no peaks are visible), there are parts of the overall NMR spectrum that show intensity but most likely do not contain a contribution from the probe molecule. The strong broadening of the peaks will be centered around their original positions (see Figure 7.9d), hence their signal is not distributed equally among the spectral region. By slicing the signal in suitable width (here a trade-off between signal-to-noise to number

of evaluated slices must be made), one can identify regions where the probe signal is still strong enough to be evaluated by a suitable visualization of both, proton-weighted fractions  $a_i$  and corresponding diffusion coefficients  $D_i$  obtained for each slice (see Figure 7.9a and b).

The disadvantages of this method include the possibility of a diverging fit for some slices and the false attribution of diffusion coefficients obtained to either the solvent or the probe fraction. This commonly happens in regions where either fraction is close to zero or the overall constant background, arising from the network, is dominating (see the shaded area of Figure 7.9). Although this is easily identified, it should be kept in mind when evaluating data in this way. Additionally, this evaluation procedure relies on high quality data where each slice has a good enough signal-to-noise ratio such that the slicing itself is not impacting the data quality, while still needing many points in the second dimension to allow the complex deconvolution of two exponentials and a constant background. Finally, it should be noted that the latter deconvolution is only successful if the exponentials themselves are separated enough in their respective diffusion coefficients.

Table 7.2: Free probe diffusion coefficients ( $D_0$ ) in solution and the corresponding reduced diffusion coefficients in the networks ( $D/D_0$ ) for the different probes at  $T = 30^\circ\text{C}$ . Data published in ref. [74]

PSC			PS		
$M_w$ (kDa)	$D_0$ ( $10^{-10}$ m <sup>2</sup> /s)	$D/D_0$	$M_w$ (kDa)	$D_0$ ( $10^{-10}$ m <sup>2</sup> /s)	$D/D_0$
0.18	$6.04 \pm 0.74$	$1.10 \pm 0.18$	1.0	$4.09 \pm 0.87$	$0.78 \pm 0.24$
2.5	$2.66 \pm 0.15$	$0.64 \pm 0.17$	10.0	$1.29 \pm 0.23$	$0.41 \pm 0.07$
6.0	$1.87 \pm 0.06$	$0.73 \pm 0.09$	30.0	$0.45 \pm 0.08$	$0.27 \pm 0.06$
10.0	$0.94 \pm 0.12$	$0.42 \pm 0.22$	70.0	$0.32 \pm 0.08$	$0.13 \pm 0.04$
20.0	$0.46 \pm 0.03$	$0.37 \pm 0.16$	100.0	$0.24 \pm 0.01$	$0.11 \pm 0.02$
40.0	$0.25 \pm 0.07$	$0.29 \pm 0.09$			
60.0	$0.21 \pm 0.03$	$0.24 \pm 0.11$			

Summing up, the procedure presented here allows for an estimate of the probe diffusion coefficients within a complex PEG-PCL matrix under the assumption of the validity of eq. 7.6 by careful evaluation of the sliced data. However, as can be seen in both Figure 7.9 and the error bars of the data (discussed in the following section), the values obtained only serve as a rough guideline and do not allow for an evaluation beyond simple models.

### Network mesh size estimated from a hard-spherical-particle approach

One possibility of estimating the relevant length scale governing the diffusion of a probe molecule through the network is by using, e.g., hydrodynamic or obstruction models that describe the interaction of the probe with the surrounding (well-defined) network "mesh". Therefore, two critical assumptions are commonly made: (i) the probe molecule is a *hard* (no chain dynamics effects) particle of spherical shape, whose diffusion can be described by  $D \propto R_h^{-1}$  and (ii) the surrounding network can be described by a singular average length scale  $\xi$ . As the data quality of the diffusion coefficients obtained is not suitable for

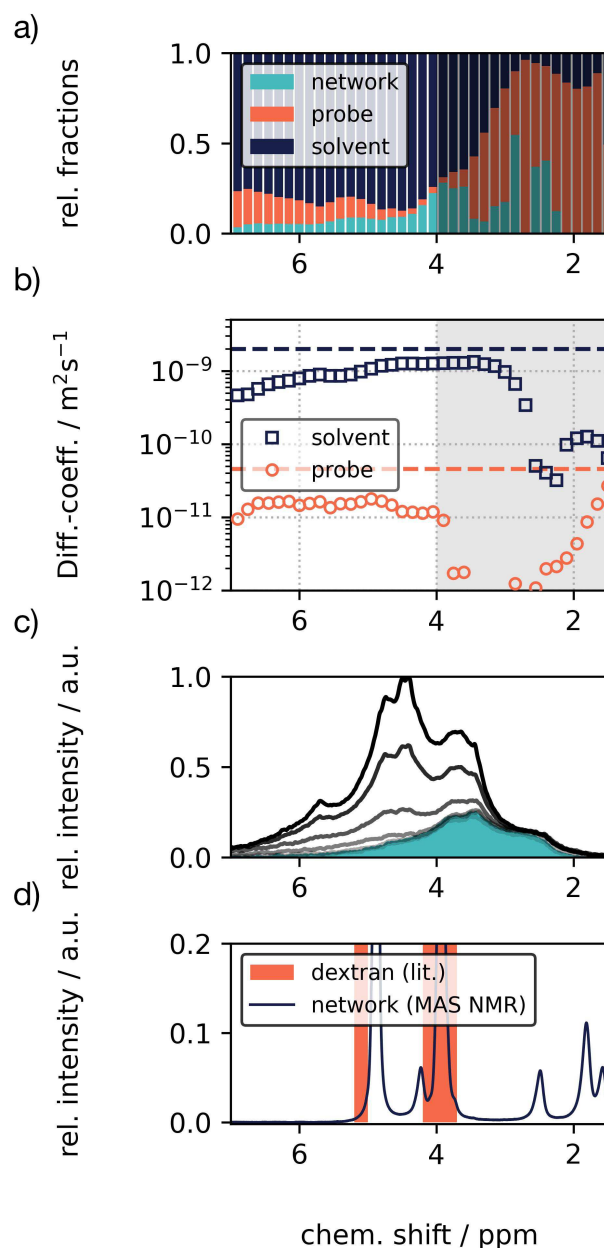


Figure 7.9: Exemplary analysis results for the PGSE experiment involving Dextran-20 kDa within the PEG-PCL network, as explained in the text. a) The bar plot illustrates fractions for each slice ( $\Delta=0.15$  ppm) within the ppm region, according to eq. 7.6. The shaded area corresponds to the region where the automated fit procedure exhibits instability. b) Diffusion coefficients for both the fast (solvent) and slow (probe) components corresponding to each slice. c)  $T_2$ -filtered ( $\Delta_{\text{diff}} = 25$  ms) proton  $^1\text{H}$ -NMR spectrum for different gradient strengths. The constant background originating from the remaining network after the  $T_2$ -filter is highlighted in blue. d) Exemplary  $^1\text{H}$  MAS NMR spectrum of the investigated ACPNs in  $\text{D}_2\text{O}$ , along with the theoretical peak positions of dextran (red rectangles). Fitting instabilities are the result of the significant contribution of the network, making it challenging to accurately attribute the network component to the dextran fraction. The substantial overlap of network and PSC resonances around 3.6–4 ppm limits integration to the broadened  $-\text{OH}$  resonance at around 5 ppm. Reprinted with permission from ref. [74]. Copyright 2023 American Chemical Society

a regression with complex multi-parameter models, only simple ("one parameter") models will be discussed here.

A popular model for describing the probe-network interaction proposed by Cukier [177] assumes that the unhindered diffusion coefficient  $D_0$  of the probe of radius  $R$  is continuously reduced by the hydrodynamic friction  $\zeta$  of the surrounding mesh that can on average be described by the screening constant  $\kappa$  which itself is dependent on the correlation length  $\xi_c$  as  $\kappa \propto \xi_c^{-1}$ . Therefore, the following relation between the reduced diffusion coefficient  $D/D_0$  and  $\xi_c$  is assumed:

$$\frac{D}{D_0} = \exp\left(-\frac{R_h}{\xi_c}\right) \quad (7.7)$$

An empirical relation for the diffusion of small (solvent) molecules was found by Fujiyabu et al. [178], by comparing the reduced diffusion coefficient of water molecules within a tPEG network with the correlation length  $\xi_c$  obtained from small-angle neutron scattering (SANS) measurements on the same type of sample. The resulting equation is similar to eq. 7.7 with differences arising only from the fact that the diameter  $d$  of the probe has to be used instead of the hydrodynamic radius  $R_h$ .

$$\frac{D}{D_0} = \exp\left(-\frac{d}{\xi_c}\right) \quad (7.8)$$

As shown in Figure 7.10, both data sets can be reasonably fitted to the Cukier hydrodynamic model, using the hydrodynamic radii obtained from the viscosity and Stokes-Einstein equation for the PSCs, while for the PS probes the empirical equation of Fetters et al. (see eq. 7.5) was used. The correlation lengths obtained from eq. 7.7 amount to  $\xi_c = 3.78$  nm for the PEG-PCL networks in water and  $\xi_c = 1.96$  nm for the PEG-PCL networks swollen in toluene. Comparing these values to  $\xi_c$  obtained at matching polymer volume fractions and sample conditions (= after a drying+reswelling cycle) by SAXS (see section 7.1 and Figure 7.1), a significant discrepancy is found. While PFG-NMR predicts  $\xi_c = 1.96$  nm in good solvent, SAXS finds about a factor of two less ( $\xi_c \approx 1$  nm) under similar conditions. While for the phase-separate state the value of  $\xi_c$  cannot be estimated by SAXS, the hereby obtained value of  $\xi_c = 3.96$  nm seems suspiciously high, as the clusters themselves should either reduce the diffusion or not interact with the probe at all. The difference in the effective degrees of swelling ( $Q_{D2O} \approx 7$  and  $Q_{tol.} \approx 5$ ) may contribute to this, but is not large enough to justify the observed difference since  $\xi_c \propto \phi^{-1} \propto Q^1$  (semi-dilute solution in a  $\theta$  solvent) is not strong enough for a scaling.

The most obvious issue in the application of this model to the data is the assumption that the probe molecules will behave like hard sphere particles of a defined radius  $R_h$ , which is similar to the assumption that the investigated system is in the dilute Zimm limit. At least for the PS probes, the latter assumption is easily discarded by the observation that even without the surrounding network the solutions of PS chains surpass their overlap concentration for at least some molecular weights, contradicting the idea of "isolated particles surrounded by solvent volume" which the Zimm limit relies on. Moving toward the Rouse limit, the effective solvent cage becomes smaller and localized in the chain segments, resulting in a decrease in the effective chain size, which - when neglected or not corrected by



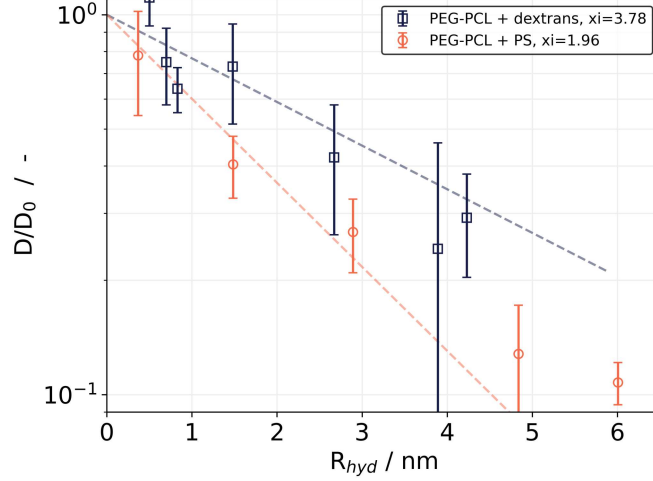


Figure 7.10: Analysis of the diffusion of PSC and PS probes of different  $R_h$  (calculated using  $M_w$ ) within a PEG-PCL network. The regression of the data follows the colloidal model described by eq. 7.7.

unknown prefactors - can result in an overestimate of the correlation length  $\xi_c$ . Therefore, any model used to characterize the present datasets cannot rely on a dilute solution of isolated probes.

### Hydrodynamic screening length estimated from the Zimm-Rouse transition model

As mentioned in the previous section, the application of a model that assumes hard-sphere probes is not sufficient for the experimental setup used. Therefore, another model motivated by chain dynamics and scaling laws (see section 2.29 and ref. [74] as developed by M. Lang) is used. Both datasets, for the PEG-PCL network in good and selective solvent respectively, are presented in a log-log plot (see Figure 7.11) and regressed by the previously discussed power law for  $D/D_0(M_w)$  describing the cross-over regime from the Zimm limit to the Rouse limit. Data points belonging to very small molecular weights that are - judged by eye - not part of the power law behavior are excluded for the regression, as  $D/D_0 \approx 1$  is expected for all probes in the Zimm limit (in contradiction to the hard-sphere models discussed before) when arguing in terms of polymer dynamics. The transition between the behaviors is expected once the hydrodynamic radius of the probe chain  $R_h$  reaches the size of the hydrodynamic screening length  $\xi_h$ . Therefore,  $\xi_h$  is estimated by the intercept of the power law scaling with  $D/D_0 = 1$  and converting the critical molecular weight to a length scale using the data measured in section 7.2.1 (for the PSC probes) or by using literature values (eq. 7.5, for the PS probes).

First, the slopes of the regression curves are analyzed, yielding scaling exponents of  $\alpha_{PS} = -0.53 \pm 0.08$  and  $\alpha_{PSC} = -0.42 \pm 0.13$ , both of which are reasonably close to  $-0.42$  (good solvent for PS probes) and  $-0.5$  ( $\theta$ -solvent for the PSC probes), respectively (see section 2.2.2). The intercepts of both curves yield critical molecular weights of  $M_{w,PSC} = 2.83 \pm 1.5 \text{ kDa}$  and  $M_{w,PS} = 1.88 \pm 0.8 \text{ kDa}$ , corresponding to hydrodynamic radii of

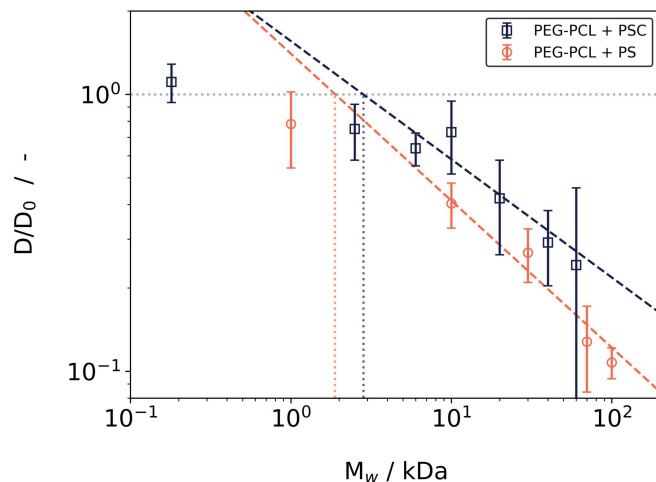


Figure 7.11: Reduced probe diffusion coefficients against their respective  $M_w$ . In the Zimm limit, an expectation of  $D/D_0 \approx 1$  is held for small  $M_w$ , whereas an anticipated transition, as per the scaling defined in equation 2.29, is expected as  $M_w$  increases. Extrapolating from the latter regime to determine  $D/D_0$  yields  $M_w = 1.88 \pm 0.8$  kDa for the PS probes and  $M_w = 2.83 \pm 1.5$  kDa for the PSC probes, resulting in hydrodynamic radii of  $R_h = 0.78 \pm 0.19$  nm (PS in  $d_8$ -toluene) and  $R_h = 0.83 \pm 0.23$  nm (PSC in  $D_2O$ ). Reprinted with permission from ref. [74]. Copyright 2023 American Chemical Society

$R_{h,PSC} = 0.83 \pm 0.23$  nm and  $R_{h,PS} = 0.78 \pm 0.19$  nm. Thus, no significant differences were observed in the permeability of the studied amphiphilic network in both good and selective solvents, even when the small differences in the swelling degree are taken into account. The primary reason for this finding may be the selective swelling of the PEG phase that comprises all the solvent, leading to a PEG phase with probably slightly stretched PEG chains. Interestingly, the topological constraints of the crosslinked network structure do not significantly reduce the permeability of the investigated network, while also allowing for a localized MPS that does not influence the diffusion of probe molecules (within the large error of the measurement). Finally, it should be noted that the hydrodynamic screening length obtained here for the network swollen in a good solvent is qualitatively in agreement with the correlation blob size of  $\xi_c = 1.01 \pm 0.06$  (see Figure 7.1) obtained from SAXS at an equivalent polymer volume fraction of  $1/Q \approx 1/6$  after a drying+reswelling process although both are estimated by two independent methods.

### 7.3 MAS DQ NMR for phase-specific estimates of dipolar couplings

Due to the induced microphase separation (MPS) and thereby connected increased topological complexity of the PEG-PCL ACPNs when swollen in a selective solvent ( $D_2O$ ), usage of the low-field Baum-Pines sequence as done in chapter 6 without chemical resolution is not feasible. Therefore, the  $^1H$  MAS POST-C7 sequence was used to study changes in the RDC values of the respective moieties (PEG backbone, PCL backbone and coupling agent) in both, good and selective solvent. For the experimental setup, the reader is referred to

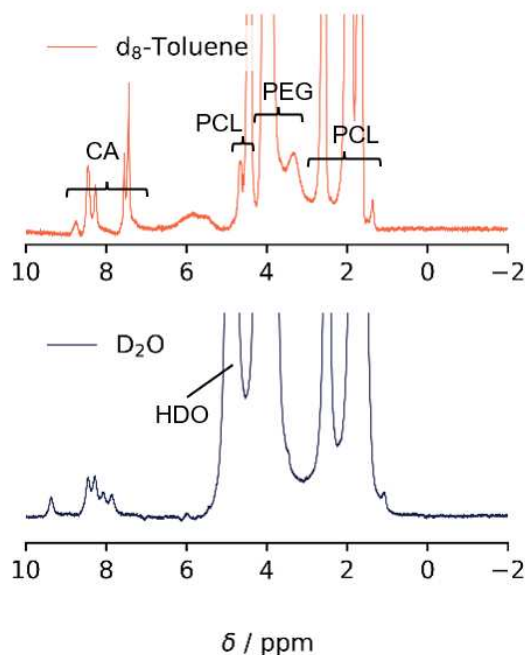


Figure 7.12:  $^1\text{H}$  MAS NMR spectra of the ACPN, both prepared at  $c = c^*$ , with  $\nu = 5$  kHz spinning. Top: Spectrum recorded at preparation conditions in  $d_8$ -toluene. Bottom: Spectrum obtained after drying and subsequent reswelling in  $\text{D}_2\text{O}$  at  $Q_{\text{eq}} \approx 4$ . The brackets denote the integration regions for the DQ build-up curve analysis presented in Figure 10. The overlap with solvent peaks presents no issue due to the isotropic tumbling, which allows for separation during the analysis. Reprinted with permission from ref. [74]. Copyright 2023 American Chemical Society

section 5.2 and for a basic introduction to the POST-C7 sequence the reader is referred to section 3.5.

Two PEG-PCL ACPNs were synthesized at  $c = c^*$  in  $d_8$ -toluene and one of the networks was dried and reswollen in  $\text{D}_2\text{O}$  ( $Q_{\text{eq}} \approx 4$ ), whereas the other network was measured under preparation conditions. The reduction of the obtained 2D dataset towards  $I_{\text{nDQ}}$  build-up curves was performed by defining three regions of interest corresponding to the respective polymer backbones and the crosslinker region (see Figure 7.12 for  $^1\text{H}$  MAS spectra) and integrating over the respective ppm regions for all DQ evolution times  $\tau_{\text{DQ}}$ . Surprisingly, no traces of multiple components are found in the signal curves obtained ( $I_{\text{ref}}$  and  $I_{\text{DQ}}$ ), hence a normalization procedure for obtaining  $I_{\text{nDQ}}$  according to section 3.4.1 and subsequent regression using the A.l.-function (eq. 3.9) could be performed (see Figure 7.13 for plots and Table 7.3 for the data obtained). Reasons for the unimodality of  $I_{\text{DQ}}$  may include the strong rotational forces arising from the MAS rotor spinning that most likely lead to an inhomogeneous and radial compression of the sample onto the rotor wall. This may also explain the unusual shape observed of  $I_{\text{nDQ}}$ .

It is found that the RDC values in the sample undergoing MPS are elevated in comparison to the as-prepared state, which is expected when considering that the PCL chains will be accommodated in clusters with no solvent inside, being comparable to e.g., melt-like chain dynamics. An RDC value of  $RDC_{\text{PCL}} = 251$  Hz is found for the PCL backbone which

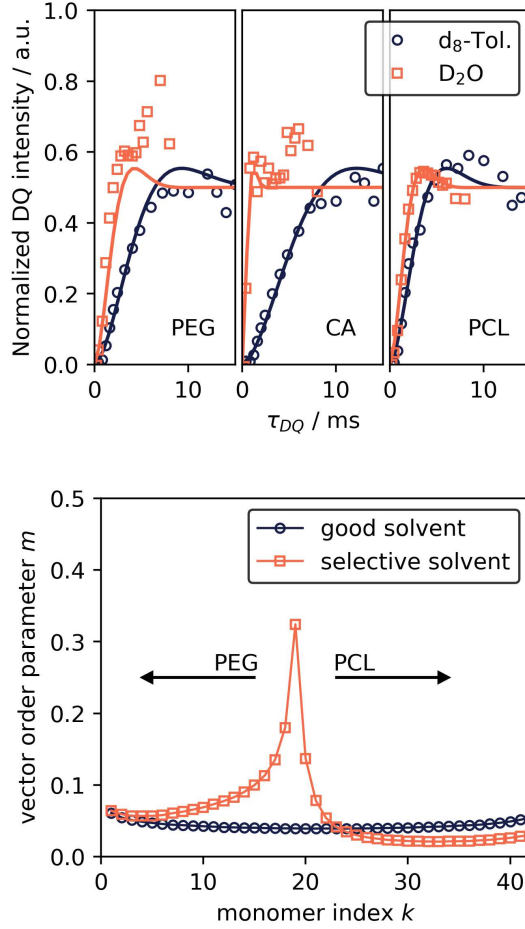


Figure 7.13: Comparison of normalized DQ build-up curves providing the fitted RDC values of CA, PEG, and PCL in ACPNs swollen in either a good solvent ( $d_8$ -toluene) or a poor solvent ( $D_2O$ ). Bottom: BFM simulation results for the vector order parameter 'm' for a chain, under as-prepared and after switching to a selective solvent conditions, respectively. Here, 'k' denotes the index in the crosslinked chain, starting from the PCL star core. The observable spike in the selective solvent conditions corresponds to the coupling position and its immediate surroundings. Reprinted with permission from ref. [74]. Copyright 2023 American Chemical Society

closely aligns with values obtained on an entangled PCL melt ( $\approx 200 - 300$ ) Hz in ref. [179] despite the significant topological differences in both systems, such as network constraints and the MPS itself. Furthermore, it is observed that the RDC value of the PEG chain is also strongly increased by a factor of approximately 2.2, which may be explained by stretching

Table 7.3: Site-specific RDC values of the ACPN in different solvents at  $c = c^*$  from DQ build-up curve analysis. Both the value and the error of the RDC value for the coupling agent (CA) in  $D_2O$  can only be roughly estimated due to the steep initial rise.

solvent	$RDC_{CA}$ (Hz)	$RDC_{PEG}$ (Hz)	$RDC_{PCL}$ (Hz)
tol.- $d_8$	$74 \pm 2$	$97 \pm 4$	$149 \pm 7$
$D_2O$	$748 \pm 100$	$212 \pm 20$	$251 \pm 6$

effects due to the MPS of the PCL phase or the fact that a significant amount of solvent is now selectively accommodated by the PEG phase as observed by the equilibrium degree of swelling of  $Q_{\text{eq}} \approx 4$ . Lastly, it is found that the RDC value of the coupling agent shows a very strong increase by a factor of roughly 10 to values of around  $\approx 750$  Hz, reaching the upper limit of what can be resolved by the experiment. This significant increase is assumed to be mediated by a strong orientation of the end groups along the normal of the PCL cluster surface, as the coupling agent will, by design, always exist at the boundary of the clustered PCL phase and the stretched PEG phase.

All of these qualitative observations are supported by bond-fluctuation model (BFM) simulations performed by Michael Lang [74] on the same system. Although it should be noted that the simulation results presented are expected to follow the experimental results only qualitatively (due to e.g., assumptions needed concerning the interaction parameters  $\chi$  of PCL and water), it will be shown that surprisingly, all simulation results are even in quantitative agreement with the experimental observations. For a screenshot of the simulated system that will be discussed later, the reader is referred to Figure 7.6. The BFM simulations confirm the clustered PCL phase with a strongly ordered "outer corona" of crosslinking agent molecules and the existence of only slightly stretched PEG chains in between. As these simulations are able to yield qualitative estimates of the vector order parameter  $m$  [107], the obtained ratios (as-prepared vs. selective solvent) are compared with the ratios obtained from the experiment ( $f_{\text{PEG}} = 2.2$ ,  $f_{\text{PCL}} = 1.6$ ,  $f_{\text{CA}} = 10$ ). As the simulations predict  $Q_{\text{eq}} = 5.8$  whereas  $Q_{\text{eq}} = 7$  is observed in the experiment, the vector order parameter of the PEG chain needs to be scaled accordingly, leading to the following final ratios obtained from the simulation as shown in Figure 7.13:  $f_{\text{PEG, sim}} = 2.0$ ,  $f_{\text{PCL, sim}} = 1.1$  and  $f_{\text{CA, sim}} = 9$ . Within the significant error of the experimental values, all of the ratios obtained here are in near perfect agreement and support the experimental observations.

Finally, it can be concluded that by a combination of  $^1\text{H}$  MAS DQ NMR and BFM simulations a qualitative understanding of the microscopic chain dynamics of the PEG-PCL ACPNs in a selective solvent could be obtained and preliminary conclusions regarding the topological arrangement of the respective moieties can be made.

## Chapter 8

# Summary

In this work,  $^1\text{H}$  static MQ NMR was used for a quantitative analysis of the discrete distribution of connectivity motifs found in different types of star polymer networks. During the course of the thesis, it was found that the well-known point-by-point normalization approach commonly used for analyzing rubber samples, fails to describe data obtained on the latter type of gel samples. Using a multi-component approach that is more suited for discrete distributions, several gel systems with different layers of complexity were successfully characterized in terms of their connectivity motifs and other structural features, such as small chain-scale clusters. A special focus was placed on the characterization of the amphiphilic tPEG-tPCL system, which was heavily inspired by the infamous tPEG-water system. A thorough characterization of the preparation state in good solvent was expanded by an investigation of the correlation length using SAXS, hydrodynamic screening length via the quantification of diffusion coefficients of probe molecules using PFG-NMR and finally a study on the length scales of clusters arising upon microphase separation by SAXS experiments.

Overall, the main experimental method of this thesis, which is  $^1\text{H}$  static low-field MQ-NMR, was applied to 5 types of swollen polymer networks, all of which are based on star-shaped precursors for enabling the quantification of well-defined connectivity motifs. The main difference between all these systems is the used coupling chemistry, consequently changing the emerging network structure. Broadly speaking, these can be divided into networks synthesized from the transient ion-mediated TPy coupling chemistry used by the Seiffert Lab Mainz and networks made from a stable chemical crosslinking reaction, including both the oxazinone-based reaction from the IPF Dresden and the disulfide-based chemistry from the ETH Zürich.

The most thoroughly investigated system of this thesis is the chemically-crosslinked tPEG-tPCL ACPN. whose connectivity motif distribution was studied in several good solvents in dependence of different synthesis-related factors. In close cooperation with the FOR-2811 research unit, networks were synthesized and analyzed using MQ-NMR, resulting in an overall assessment of these networks to be inferior in terms of SL fraction compared to the Sakai-type tPEG network. Despite this, the average RDC values, mechanical properties, and overall fraction of isotropic defects were found to be superior. Systematic investiga-

tions of temperature programs and solvents revealed no significant dependencies of these properties, leading to the conclusion that the synthesis procedure is adaptable and yields reproducible results. During the course of this investigation, additional peculiarities such as a post-curing effect upon drying of the gels and a significant change in the orientational order of the PEG chain upon switching from water to a non-polar solvent were observed. Eventually, the microphase-separated state of the tPEG-tPCL ACPNs was explored by studying the diffusion of probes in good and selective solvent, yielding estimates for the hydrodynamic screening length governing the diffusion process of penetrants through the network. Connected to this, an automated procedure for the evaluation of PFG-NMR data with indistinguishable peaks was presented and successfully applied. The values in good solvent showed qualitative agreement with the correlation length obtained from SAXS data, confirming empirical assumptions, while providing additional insights into the post-curing effect previously observed by NMR. Additional SAXS experiments in selective solvent and successive evaluation using both the Kinning-Thomas and Teubner-Strey models revealed that significant assumptions were needed to evaluate the data beyond the cluster distance. Additional bond-fluctuation model simulations on a qualitatively similar system were needed to narrow down the radius of gyration and aggregation number of the clusters. Lastly, the local chain dynamics of the different moieties after MPS were studied by POST-C7 NMR experiments and quantitatively confirm the BFM simulation predictions of a surface-localized immobilization of the crosslinking end group and the respective changes in the order parameter of the melt-like PCL chains and slightly oriented PEG chains.

An investigation of a homocomplementary chemically-crosslinked network, being the homocomplementary tPEG-SH system swollen in water, allowed for a quantification of changes occurring when switching to a coupling chemistry that does not prevent the formation of odd-numbered cyclic defect structures such as the primary loop defect. The system revealed a fraction of single links and average RDC value that displays a considerably steeper dependency on the relative preparation concentration  $c/c^*$  than predicted and measured for the heterocomplementary end-linked Sakai-type network. While this was expected considering the self-reactivity of the used precursors, the analysis of samples at preparation concentrations above  $c^*$  revealed SL fraction and RDC values, both of which are surprisingly comparable to the Sakai-type network. This may emphasize the importance of spatial distance between precursors and thereby-connected reaction kinetics in overcoming issues of the formation of elastically-inactive primary loops for the formation of networks from homocomplementary precursors.

A study of a of PEG-linPEG-TPy networks utilizing the active ester chemistry of Sakai et al. with an additional transient crosslink based on functional TPy groups and ions of different strength was performed using  $^1\text{H}$  static MQ-NMR. It produced several results that confirm theoretical findings concerning the expected strong increase in the primary loop content due to the usage of a linear chain as a crosslinker. A variation of the ion species (and the thereby connected cluster fraction) revealed that MQ NMR is not only sensitive to this type of localized chain-scale cluster, but additionally is able to distinguish

these from more mobile defect structures based on the respective relaxation times. The overall possibilities of this kind of linking chemistry on the emerging network structure was further investigated by studying a set of tPEG-tPEG gels that were transiently crosslinked using a combination of either terpyridine or a more sterically demanding phenantroline end group in combination with different ions. While MQ NMR was not able to detect large differences in the overall distribution of connectivity motifs, a clear correlation between the observed defect fraction and the preferences of the ions for certain coordination geometries competing with the sterical hindrances of the end groups, was observed. Thus, it could be confirmed that the defect content of these transient tPEG networks can be controlled by the degree of the self-sorting, which generally speaking may lead to a feasible platform for controllable gels with a reduced amount of large-scale frozen inhomogeneities.

Lastly, the connectivity motif distributions of networks resulting from mixtures with different ratios of tPEG-TPy precursors and 8-arm PEG-TPy precursors were investigated. The overall behavior - a strong increase in defects with an increase of the fraction of 8-arm PEG precursors - is in contradiction to both theoretical and recent experimental findings, both of which predict the opposite trend. The assumed reason is an underlying strong dependence of the emerging network structure on the overall conversion rate of the synthesis, which was strongly impacted by the low end group conversion of the 8-arm PEG precursors. Nevertheless, the experiments fortunately revealed a defect-controlled system whose mechanical and permeation properties could be precisely controlled by the introduction of defective precursors.

Summing up this work, a study of the chain connectivity motifs of several different types of tPEG-based networks, utilizing different cross-linking agents and both physical and chemical bonds, was performed. One of the generalized findings is that the crosslinking agent is the dominating factor that drives the overall microstructure and therefore the macroscopic properties. While MQ NMR excels in a surprisingly precise (but model-dependent) description of the microstructure, most of its value is accessed when compared with more-established methods such as rheology, swelling experiments or scattering. Nevertheless, for all systems it can be concluded that usage of one method alone might result in a severe mischaracterization of these samples, as the general (hierarchical) structure of gels tends to be complex. This work aims for providing a foundation when using MQ NMR as a connecting link in-between other methods for the characterization of such networks.



# Bibliography

- (1) Seymour, R. B.; Mark, H. F., *Applications of polymers*; Springer: 1988.
- (2) Zou, W.; Dong, J.; Luo, Y.; Zhao, Q.; Xie, T. *Advanced Materials* **2017**, *29*, 1606100.
- (3) Nakagawa, S.; Yoshie, N. *Polymer Chemistry* **2022**, *13*, 2074–2107.
- (4) Gu, Y.; Zhao, J.; Johnson, J. A. *Angewandte Chemie International Edition* **2020**, *59*, 5022–5049.
- (5) Rubinstein, M.; Colby, R. H., *Polymer physics*; Oxford University Press: Oxford ; 2007.
- (6) Golkaram, M.; Loos, K. *Macromolecules* **2019**, *52*, 9427–9444.
- (7) Rossow, T.; Habicht, A.; Seiffert, S. *Macromolecules* **2014**, *47*, 6473–6482.
- (8) Yan, T.; Schröter, K.; Herbst, F.; Binder, W. H.; Thurn-Albrecht, T. *Macromolecules* **2017**, *50*, 2973–2985.
- (9) Flory, P. J.; Rehner Jr, J. *The journal of chemical physics* **1943**, *11*, 521–526.
- (10) Ono, T.; Sugimoto, T.; Shinkai, S.; Sada, K. *Nature Materials* **2007**, *6*, 429–433.
- (11) Guo, Y.; Yu, G. *Accounts of Materials Research* **2021**, *2*, 374–384.
- (12) Correa, S.; Grosskopf, A. K.; Lopez Hernandez, H.; Chan, D.; Yu, A. C.; Stapleton, L. M.; Appel, E. A. *Chemical Reviews* **2021**, *121*, 11385–11457.
- (13) Nicolson, P. C.; Vogt, J. *Biomaterials* **2001**, *22*, 3273–3283.
- (14) Shi, Y.; Zhou, X.; Zhang, J.; Bruck, A. M.; Bond, A. C.; Marschilok, A. C.; Takeuchi, K. J.; Takeuchi, E. S.; Yu, G. *Nano Letters* **2017**, *17*, 1906–1914.
- (15) Tobis, J.; Boch, L.; Thomann, Y.; Tiller, J. C. *Journal of Membrane Science* **2011**, *372*, 219–227.
- (16) Yoshida, R. Design of Functional Polymer Gels and Their Application to Biomimetic Materials, 2005.
- (17) Kamata, H.; Li, X.; Chung, U.-i.; Sakai, T. *Advanced Healthcare Materials* **2015**, *4*, 2360–2374.
- (18) Hoffman, A. S. *Advanced Drug Delivery Reviews* **2012**, *64*, 18–23.
- (19) Allen, G.; Egerton, P. L.; Walsh, D. J. *Polymer* **1976**, *17*, 65–71.
- (20) Mark, J. E.; Sullivan, J. L. *The Journal of Chemical Physics* **1977**, *66*, 1006–1011.
- (21) Sakai, T.; Matsunaga, T.; Yamamoto, Y.; Ito, C.; Yoshida, R.; Suzuki, S.; Sasaki, N.; Shibayama, M.; Chung, U.-i. *Macromolecules* **2008**, *41*, 5379–5384.
- (22) Matsunaga, T.; Sakai, T.; Akagi, Y.; Chung, U.-i.; Shibayama, M. *Macromolecules* **2009**, *42*, 6245–6252.
- (23) Lange, F.; Schwenke, K.; Kurakazu, M.; Akagi, Y.; Chung, U.-i.; Lang, M.; Sommer, J.-U.; Sakai, T.; Saalwächter, K. *Macromolecules* **2011**, *44*, 9666–9674.
- (24) Zhong, M.; Wang, R.; Kawamoto, K.; Olsen, B. D.; Johnson, J. A. *Science* **2016**, *353*, 1264–1268.
- (25) Lang, M. *ACS Macro Letters* **2018**, *7*, 536–539.

- (26) Li, X.; Nakagawa, S.; Tsuji, Y.; Watanabe, N.; Shibayama, M. *Science advances* **2019**, *5*, eaax8647.
- (27) Li, X. *Polymer Journal* **2021**, *53*, 765–777.
- (28) Kondo, S.; Hiroi, T.; Han, Y.-S.; Kim, T.-H.; Shibayama, M.; Chung, U. I.; Sakai, T. *Advanced Materials (Deerfield Beach, Fla.)* **2015**, *27*, 7407–7411.
- (29) Gu, Y.; Kawamoto, K.; Zhong, M.; Chen, M.; Hore, M. J. A.; Jordan, A. M.; Korley, L. T. J.; Olsen, B. D.; Johnson, J. A. *Proceedings of the National Academy of Sciences* **2017**, *114*, 4875–4880.
- (30) Nicoletta, P.; Koziol, M. F.; Löser, L.; Saalwächter, K.; Ahmadi, M.; Seiffert, S. *Soft Matter* **2022**, 1071–1081.
- (31) Darby, D. R.; Stephens, L. F.; Chwatko, M.; Pham, J. T. *Macromolecular Chemistry and Physics* **2023**, *n/a*, 2300102.
- (32) Kawamoto, K.; Zhong, M.; Wang, R.; Olsen, B. D.; Johnson, J. A. *Macromolecules* **2015**, *48*, 8980–8988.
- (33) Ahmadi, M.; Seiffert, S. *Journal of Polymer Science* **2020**, *58*, 330–342.
- (34) Dänmark, S.; Aronsson, C.; Aili, D. *Biomacromolecules* **2016**, *17*, 2260–2267.
- (35) Seiffert, S.; Sprakel, J. *Chemical Society Reviews* **2012**, *41*, 909–930.
- (36) Cordier, P.; Tournilhac, F.; Soulié-Ziakovic, C.; Leibler, L. *Nature* **2008**, *451*, 977–980.
- (37) Patrickios, C. S., *Amphiphilic Polymer Co-networks*; Polymer Chemistry Series; The Royal Society of Chemistry: 2020, pp 001–368.
- (38) Chen, D.; Kennedy, J. P.; Allen, A. J. *Journal of Macromolecular Science - Chemistry* **1988**, *25*, 389–401.
- (39) Truong, V.; Blakey, I.; Whittaker, A. K. *Biomacromolecules* **2012**, *13*, 4012–4021.
- (40) Malkoch, M.; Vestberg, R.; Gupta, N.; Mespouille, L.; Dubois, P.; Mason, A. F.; Hedrick, J. L.; Liao, Q.; Frank, C. W.; Kingsbury, K. *Chemical Communications* **2006**, 2774–2776.
- (41) Lowe, A. B. *Polymer Chemistry* **2014**, *5*, 4820–4870.
- (42) Hiroi, T.; Kondo, S.; Sakai, T.; Gilbert, E. P.; Han, Y.-S.; Kim, T.-H.; Shibayama, M. *Macromolecules* **2016**, *49*, 4940–4947.
- (43) Kamata, H.; Akagi, Y.; Kayasuga-Kariya, Y.; Chung, U.-i.; Sakai, T. *Science* **2014**, *343*, 873–875.
- (44) Kepola, E. J.; Loizou, E.; Patrickios, C. S.; Leontidis, E.; Voutouri, C.; Stylianopoulos, T.; Schweins, R.; Gradzielski, M.; Krumm, C.; Tiller, J. C. *ACS Macro Letters* **2015**, *4*, 1163–1168.
- (45) Kitiri, E. N.; Patrickios, C. S.; Voutouri, C.; Stylianopoulos, T.; Hoffmann, I.; Schweins, R.; Gradzielski, M. *Polymer Chemistry* **2017**, *8*, 245–259.
- (46) Krumm, C.; Konieczny, S.; Dropalla, G. J.; Milbradt, M.; Tiller, J. C. *Macromolecules* **2013**, *46*, 3234–3245.
- (47) Bunk, C.; Löser, L.; Fribicz, N.; Komber, H.; Jakisch, L.; Scholz, R.; Voit, B.; Seiffert, S.; Saalwächter, K.; Lang, M.; Böhme, F. *Macromolecules* **2022**, *55*, 6573–6589.
- (48) Schwenke, K.; Lang, M.; Sommer, J.-U. *Macromolecules* **2011**, *44*, 9464–9472.
- (49) Stadler, F. J. *Proceedings of the National Academy of Sciences* **2013**, *110*, E1972–E1972.
- (50) Olsen, B. D.; Johnson, J. A. *Proceedings of the National Academy of Sciences* **2013**, *110*, E1973–E1973.
- (51) Dobrynin, A. V.; Tian, Y.; Jacobs, M.; Nikitina, E. A.; Ivanov, D. A.; Maw, M.; Vashahi, F.; Sheiko, S. S. *Nature Materials* **2023**, *22*, 1394–1400.

- (52) Zhou, H.; Woo, J.; Cok, A. M.; Wang, M.; Olsen, B. D.; Johnson, J. A. *Proceedings of the National Academy of Sciences* **2012**, *109*, 19119–19124.
- (53) Saalwächter, K. *Progress in Nuclear Magnetic Resonance Spectroscopy* **2007**, *51*, 1–35.
- (54) Saalwächter, K. In *Modern Magnetic Resonance*, Webb, G. A., Ed.; Springer International Publishing: Cham, 2018, pp 755–781.
- (55) Ahmadi, M.; Löser, L.; Fischer, K.; Saalwächter, K.; Seiffert, S. *Macromolecular Chemistry and Physics* **2020**, *221*, 1900400.
- (56) Seiffert, S. *Progress in Polymer Science* **2017**, *66*, 1–21.
- (57) Ornstein, L. S. *Proc. Akad. Sci.* **1914**, *17*, 793.
- (58) Hammouda, B.; Ho, D. L.; Kline, S. *Macromolecules* **2004**, *37*, 6932–6937.
- (59) Benski, L.; Viran, I.; Katzenberg, F.; Tiller, J. C. *Macromolecular Chemistry and Physics* **2021**, *222*, 2000292.
- (60) Guzman, G.; Nugay, T.; Kennedy, J. P.; Cakmak, M. *Langmuir* **2016**, *32*, 3445–3451.
- (61) Iván, B.; Haraszti, M.; Erdődi, G.; Scherble, J.; Thomann, R.; Mülhaupt, R. In *Macromolecular Symposia*, Wiley Online Library: 2005; Vol. 227, pp 265–274.
- (62) Haggmann, K.; Bunk, C.; Böhme, F.; von Klitzing, R. *Polymers* **2022**, *14*, 2555.
- (63) Richbourg, N. R.; Peppas, N. A. *Macromolecules* **2021**, *54*, 10477–10486.
- (64) Fatin-Rouge, N.; Starchev, K.; Buffle, J. *Biophysical Journal* **2004**, *86*, 2710–2719.
- (65) Sun, J.; Lyles, B. F.; Yu, K. H.; Weddell, J.; Pople, J.; Hetzer, M.; Kee, D. D.; Russo, P. S. *The Journal of Physical Chemistry B* **2008**, *112*, 29–35.
- (66) Colsenet, R.; Söderman, O.; Mariette, F. *Macromolecules* **2006**, *39*, 1053–1059.
- (67) Matsukawa, S.; Ando, I. *Macromolecules* **1997**, *30*, 8310–8313.
- (68) Amdursky, N.; Orbach, R.; Gazit, E.; Huppert, D. *Journal of Physical Chemistry C* **2009**, *113*, 19500–19505.
- (69) Lin, T.-S.; Wang, R.; Johnson, J. A.; Olsen, B. D. *Macromolecules* **2018**, *51*, 1224–1231.
- (70) Lang, M.; Scholz, R.; Löser, L.; Bunk, C.; Fribicz, N.; Seiffert, S.; Böhme, F.; Saalwächter, K. *Macromolecules* **2022**, *55*, 5997–6014.
- (71) Meng, Z.; Löser, L.; Saalwächter, K.; Gasser, U.; Klock, H.-A. *Macromolecules (submitted)* **2023**.
- (72) Teubner, M.; Strey, R. *The Journal of Chemical Physics* **1987**, *87*, 3195–3200.
- (73) Amsden, B. G. *Macromolecules* **2022**, *55*, 8399–8408.
- (74) Löser, L.; Bunk, C.; Scholz, R.; Lang, M.; Böhme, F.; Saalwächter, K. *Macromolecules* **2024**, DOI: 10.1021/acs.macromol.3c02139.
- (75) Tsuji, Y.; Li, X.; Shibayama, M. Evaluation of Mesh Size in Model Polymer Networks Consisting of Tetra-Arm and Linear Poly(ethylene glycol)s, 2018.
- (76) Sakai, T., *Physics of polymer gels*; John Wiley & Sons: 2020.
- (77) Flory, P. J. *The Journal of Chemical Physics* **1949**, *17*, 303–310.
- (78) Fisher, M. E. *The Journal of Chemical Physics* **1966**, *44*, 616–622.
- (79) Le Guillou, J. C.; Zinn-Justin, J. *Physical Review Letters* **1977**, *39*, 95–98.
- (80) Flory, P. J., *Principles of polymer chemistry*; Cornell university press: 1953.
- (81) Cotton, J. P.; Decker, D.; Benoit, H.; Farnoux, B.; Higgins, J.; Jannink, G.; Ober, R.; Picot, C. d.; Des Cloizeaux, J. *Macromolecules* **1974**, *7*, 863–872.
- (82) Einstein, A. *Annalen der Physik* **1905**, *322*, 549–560.

- (83) Von Smoluchowski, M. *Annalen der Physik* **1906**, *326*, 756–780.
- (84) Zimm, B. H. *The Journal of Chemical Physics* **1956**, *24*, 269–278.
- (85) Prakash, J. R. *Current Opinion in Colloid & Interface Science* **2019**, *43*, 63–79.
- (86) De Gennes, P. G. *The Journal of Chemical Physics* **1971**, *55*, 572–579.
- (87) Winter, H. H.; Chambon, F. *Journal of Rheology* **1986**, *30*, 367–382.
- (88) De Gennes, P.-G., *Scaling concepts in polymer physics*; Cornell University Press: 1979.
- (89) Flory, P. J. *Macromolecules* **1982**, *15*, 99–100.
- (90) Scanlan, J. *Journal of Polymer Science* **1960**, *43*, 501–508.
- (91) Matsunaga, T.; Sakai, T.; Akagi, Y.; Chung, U.-i.; Shibayama, M. *Macromolecules* **2009**, *42*, 1344–1351.
- (92) Nishi, K.; Fujii, K.; Katsumoto, Y.; Sakai, T.; Shibayama, M. *Macromolecules* **2014**, *47*, 3274–3281.
- (93) Lin, T.-S.; Wang, R.; Johnson, J. A.; Olsen, B. D. *Macromolecules* **2018**, *51*, 1224–1231.
- (94) Akagi, Y.; Matsunaga, T.; Shibayama, M.; Chung, U.-i.; Sakai, T. *Macromolecules* **2010**, *43*, 488–493.
- (95) Okumoto, M.; Nakamura, Y.; Norisuye, T.; Teramoto, A. *Macromolecules* **1998**, *31*, 1615–1620.
- (96) Morris, G. A. *NMR in Biomedicine* **2009**, *22*, 240–241.
- (97) Keeler, J., *Understanding NMR spectroscopy*; John Wiley & Sons: 2010.
- (98) Duer, M. J., *Solid state NMR spectroscopy: principles and applications*; John Wiley & Sons: 2008.
- (99) Saalwächter, K.; Spiess, H. W. In *Polymer Science: A Comprehensive Reference*, Matyjaszewski, K., Möller, M., Eds.; Elsevier: Amsterdam, 2012, pp 185–219.
- (100) Cohen-Addad, J. P. *J. Phys. France* **1982**, *43*, 1509–1528.
- (101) Cohen-Addad, J. P.; Dupeyre, R. *Polymer* **1983**, *24*, 400–408.
- (102) Brereton, M. G. *Macromolecules* **1990**, *23*, 1119–1131.
- (103) Brereton, M. G. *The Journal of chemical physics* **1991**, *94*, 2136–2142.
- (104) Bayro, M. J.; Huber, M.; Ramachandran, R.; Davenport, T. C.; Meier, B. H.; Ernst, M.; Griffin, R. G. *The Journal of Chemical Physics* **2009**, *130*, 114506.
- (105) Saalwächter, K. *ChemPhysChem* **2013**, *14*, 3000–3014.
- (106) Sommer, J.-U.; Chassé, W.; Valentín, J. L.; Saalwächter, K. *Physical Review E* **2008**, *78*, 51803.
- (107) Chassé, W.; Saalwächter, K.; Sommer, J.-U. *Macromolecules* **2012**, *45*, 5513–5523.
- (108) Baum, J.; Pines, A. *Journal of the American Chemical Society* **1986**, *108*, 7447–7454.
- (109) Saalwächter, K.; Heuer, A. *Macromolecules* **2006**, *39*, 3291–3303.
- (110) Baum, J.; Munowitz, M.; Garroway, A. N.; Pines, A. *The Journal of Chemical Physics* **1985**, *83*, 2015–2025.
- (111) Saalwächter, K.; Ziegler, P.; Spyckerelle, O.; Haidar, B.; Vidal, A.; Sommer, J. U. *Journal of Chemical Physics* **2003**, *119*, 3468–3482.
- (112) Levitt, M. H. *Journal of Magnetic Resonance (1969)* **1982**, *48*, 234–264.
- (113) Reichert, D.; Hempel, G. *Concepts in Magnetic Resonance* **2002**, *14*, 130–139.
- (114) Saalwächter, K. *The Journal of Chemical Physics* **2003**, *120*, 454–464.

- (115) Chassé, W.; Valentin, J. L.; Genesky, G. D.; Cohen, C.; Saalwächter, K. *Journal of Chemical Physics* **2011**, *134*.
- (116) Saalwächter, K. *Rubber Chemistry and Technology* **2012**, *85*, 350–386.
- (117) Andrew, E. R.; Bradbury, A.; Eades, R. G. *Nature* **1958**, *182*, 1659.
- (118) Lowe, I. J. *Physical Review Letters* **1959**, *2*, 285.
- (119) Tycko, R.; Dabbagh, G. *Chemical Physics Letters* **1990**, *173*, 461–465.
- (120) Feike, M.; Demco, D. E.; Graf, R.; Gottwald, J.; Hafner, S.; Spiess, H. W. *Journal of Magnetic Resonance, Series A* **1996**, *122*, 214–221.
- (121) Lee, Y. K.; Kurur, N. D.; Helmle, M.; Johannessen, O. G.; Nielsen, N. C.; Levitt, M. H. *Chemical Physics Letters* **1995**, *242*, 304–309.
- (122) Levitt, M. H. *Magnetic Resonance* **2007**.
- (123) Hohwy, M.; Jakobsen, H. J.; Edén, M.; Levitt, M. H.; Nielsen, N. C. *The Journal of Chemical Physics* **1998**, *108*, 2686–2694.
- (124) Hahn, E. L. Spin echoes, 1950.
- (125) Carr, H. Y.; Purcell, E. M. *Physical Review* **1954**, *94*, 630–638.
- (126) Stejskal, E. O.; Tanner, J. E. *The journal of chemical physics* **1965**, *42*, 288–292.
- (127) Tanner, J. E. *The Journal of Chemical Physics* **2003**, *52*, 2523–2526.
- (128) Price, W. S. *Concepts in Magnetic Resonance* **1997**, *9*, 299–336.
- (129) De Jeu, W. H., *Basic X-ray scattering for soft matter*; Oxford University Press: London, England, 2016.
- (130) Roe, R.-J. (*No Title*) **2000**.
- (131) Strobl, G. R.; Strobl, G. R., *The physics of polymers*; Springer: 2007; Vol. 2.
- (132) Zernike, F.; Prins, J. A. *Zeitschrift für Physik A Hadrons and nuclei* **1927**, *41*, 184–194.
- (133) Porod, G. In *Small angle X-ray scattering*, 1982.
- (134) Sinha, S. K.; Sirota, E. B.; Garoff, S.; Stanley, H. B. *Physical Review B* **1988**, *38*, 2297–2311.
- (135) Oikawa, H.; Murakami, K. *Macromolecules* **1991**, *24*, 1117–1122.
- (136) Fujiyabu, T.; Yoshikawa, Y.; Chung, U.-i.; Sakai, T. *Science and Technology of Advanced Materials* **2019**, *20*, 608–621.
- (137) Kafouris, D.; Gradzielski, M.; Patrickios, C. S. *Macromolecules* **2009**, *42*, 2972–2980.
- (138) Apostolides, D. E.; Patrickios, C. S.; Simon, M.; Gradzielski, M.; Blanas, A.; Mus-sault, C.; Marcellan, A.; Alexander, N.; Wesdemiotis, C. *Polymer Chemistry* **2023**, *14*, 201–211.
- (139) Tsitsilianis, C.; Serras, G.; Ko, C.-H.; Jung, F.; Papadakis, C. M.; Rikkou-Kalourkoti, M.; Patrickios, C. S.; Schweins, R.; Chassenieux, C. *Macromolecules* **2018**, *51*, 2169–2179.
- (140) Debye, P.; Bueche, A. M. *Journal of Applied Physics* **1949**, *20*, 518–525.
- (141) Thünemann, A. F.; Gruber, A.; Klinger, D. *Langmuir* **2020**, *36*, 10979–10988.
- (142) Kinning, D. J.; Thomas, E. L. *Macromolecules* **1984**, *17*, 1712–1718.
- (143) Percus, J. K.; Yevick, G. J. *Physical Review* **1958**, *110*, 1–13.
- (144) Wertheim, M. S. *Physical Review Letters* **1963**, *10*, 321–323.
- (145) Thiele, E. *The Journal of Chemical Physics* **1963**, *39*, 474–479.
- (146) Narimani, R.; Yang, A. C. C.; Tsang, E. M. W.; Rubatat, L.; Holdcroft, S.; Frisken, B. J. *Macromolecules* **2013**, *46*, 9676–9687.

- (147) Kinning, D. J.; Thomas, E. L.; Fetters, L. J. *The Journal of Chemical Physics* **1989**, *90*, 5806–5825.
- (148) Yan, T.; Schröter, K.; Herbst, F.; Binder, W. H.; Thurn-Albrecht, T. *Macromolecules* **2014**, *47*, 2122–2130.
- (149) Mordvinkin, A.; Suckow, M.; Böhme, F.; Colby, R. H.; Creton, C.; Saalwächter, K. *Macromolecules* **2019**, *52*, 4169–4184.
- (150) Hall, L. M.; Seitz, M. E.; Winey, K. I.; Opper, K. L.; Wagener, K. B.; Stevens, M. J.; Frischknecht, A. L. *Journal of the American Chemical Society* **2012**, *134*, 574–587.
- (151) Bunk, C.; Fribicz, N.; Löser, L.; Geisler, M.; Voit, B.; Seiffert, S.; Saalwächter, K.; Lang, M.; Böhme, F. *Polymer Chemistry (submitted)* **2023**.
- (152) Ahmadi, M.; Löser, L.; Pareras, G.; Poater, A.; Saalwächter, K.; Seiffert, S. *Chemistry of Materials* **2023**, *35*, 4026–4037.
- (153) Parker, J. R. *Computing* **2000**, *65*, 291–312.
- (154) Löser, L.; Saalwächter, K. Solid-State NMR Python codes for evaluating MQ-NMR and PFG-NMR data; 10.5281/zenodo.10560019, 2024.
- (155) Sivia, D.; Skilling, J., *Data analysis: a Bayesian tutorial*; OUP Oxford: 2006.
- (156) Schäler, K.; Roos, M.; Micke, P.; Golitsyn, Y.; Seidlitz, A.; Thurn-Albrecht, T.; Schneider, H.; Hempel, G.; Saalwächter, K. *Solid State Nuclear Magnetic Resonance* **2015**, *72*, 50–63.
- (157) Koenig, J. L.; Angood, A. C. *Journal of Polymer Science Part A-2: Polymer Physics* **1970**, *8*, 1787–1796.
- (158) Tasaki, K. *Journal of the American Chemical Society* **1996**, *118*, 8459–8469.
- (159) Ferreira, T. M.; Medronho, B.; Martin, R. W.; Topgaard, D. *Physical Chemistry Chemical Physics* **2008**, *10*, 6033–6038.
- (160) Fribicz, N.; Hagmann, K.; Bunk, C.; Böhme, F.; von Klitzing, R.; Seiffert, S. *Macromolecular Chemistry and Physics* **2023**, *n/a*, 2300389.
- (161) Gong, J. P. *Soft Matter* **2010**, *6*, 2583–2590.
- (162) Levitt, M. H., *Spin Dynamics: Basics of Nuclear Magnetic Resonance*; Wiley: 2013.
- (163) Appel, E. A.; Biedermann, F.; Hoogland, D.; del Barrio, J.; Driscoll, M. D.; Hay, S.; Wales, D. J.; Scherman, O. A. *Journal of the American Chemical Society* **2017**, *139*, 12985–12993.
- (164) Holyer, R. H.; Hubbard, C. D.; Kettle, S. F. A.; Wilkins, R. G. *Inorganic Chemistry* **1966**, *5*, 622–625.
- (165) Begam, N.; Ragulskaya, A.; Girelli, A.; Rahmann, H.; Chandran, S.; Westermeier, F.; Reiser, M.; Sprung, M.; Zhang, F.; Gutt, C.; Schreiber, F. *Physical Review Letters* **2021**, *126*, 98001.
- (166) Mohanty, B.; Aswal, V. K.; Kohlbrecher, J.; Bohidar, H. B. *Journal of Polymer Science Part B: Polymer Physics* **2006**, *44*, 1653–1667.
- (167) Lust, S. T.; Hoogland, D.; Norman, M. D. A.; Kerins, C.; Omar, J.; Jowett, G. M.; Yu, T.; Yan, Z.; Xu, J. Z.; Marciano, D.; da Silva, R. M. P.; Dreiss, C. A.; Lamata, P.; Shipley, R. J.; Gentleman, E. *ACS Biomaterials Science & Engineering* **2021**, *7*, 4293–4304.
- (168) Raeber, G. P.; Lutolf, M. P.; Hubbell, J. A. *Biophysical Journal* **2005**, *89*, 1374–1388.
- (169) Fleischer, G.; Zgadzai, O. E.; Skirda, V. D.; Maklakov, A. I. *Colloid and Polymer Science* **1988**, *266*, 201–207.

- (170) Augé, S.; Schmit, P.-O.; Crutchfield, C. A.; Islam, M. T.; Harris, D. J.; Durand, E.; Clemancey, M.; Quoineaud, A.-A.; Lancelin, J.-M.; Prigent, Y.; Taulelle, F.; Delsuc, M.-A. *The Journal of Physical Chemistry B* **2009**, *113*, 1914–1918.
- (171) Wallace, M.; Adams, D. J.; Iggo, J. A. *Soft Matter* **2013**, *9*, 5483–5491.
- (172) Morris, E. R.; Cutler, A. N.; Ross-Murphy, S. B.; Rees, D. A.; Price, J. *Carbohydrate Polymers* **1981**, *1*, 5–21.
- (173) Tirtaatmadja, V.; Dunstan, D. E.; Boger, D. V. *Journal of Non-Newtonian Fluid Mechanics* **2001**, *97*, 295–301.
- (174) Köhler, W.; Rosenauer, C.; Rossmannith, P. *International Journal of Thermophysics* **1995**, *16*, 11–21.
- (175) Braeckmans, K.; Peeters, L.; Sanders, N. N.; De Smedt, S. C.; Demeester, J. *Biophysical Journal* **2003**, *85*, 2240–2252.
- (176) Fetters, L. J.; Hadjichristidis, N.; Lindner, J. S.; Mays, J. W. *Journal of Physical and Chemical Reference Data* **1994**, *23*, 619–640.
- (177) Cukier, R. I. *Macromolecules* **1984**, *17*, 252–255.
- (178) Fujiyabu, T.; Li, X.; Chung, U.-i.; Sakai, T. *Macromolecules* **2019**, *52*, 1923–1929.
- (179) Kurz, R.; Schulz, M.; Scheliga, F.; Men, Y.; Seidlitz, A.; Thurn-Albrecht, T.; Saalwächter, K. *Macromolecules* **2018**, *51*, 5831–5841.





# ACKNOWLEDGEMENTS

Aus Datenschutzgründen entfernt.

# CURRICULUM VITAE

## **Persönliche Informationen**

Name: Lucas Löser  
Nationalität: Deutsch

## **Beruf**

seit 02/2024: Digital Engineering Consultant, Akkodis DCE (Leipzig)  
12/2018 – 12/2023: Wissenschaftlicher Mitarbeiter, MLU Halle-Wittenberg (Halle)

## **Ausbildung**

12/2018 – 12/2023: Doktorand, MLU Halle-Wittenberg  
10/2016 – 11/2018: Master of Science, Medizinische Physik, MLU Halle-Wittenberg  
10/2013 – 09/2016: Bachelor of Science, Medizinische Physik, MLU Halle-Wittenberg  
08/2007 – 06/2013: Schulische Ausbildung, Gymnasium Prenzlau

Halle (Saale), den 21.06.2024

Lucas Löser

# EIDESSTAATLICHE ERKLÄRUNG

Hiermit versichere ich, die vorliegende Arbeit selbstständig und ohne fremde Hilfe verfasst und keine anderen als die von mir angegebenen Quellen und Hilfsmittel verwendet zu haben. Die den benutzten Werken wörtlich oder inhaltlich entnommenen Stellen habe ich als solche kenntlich gemacht. Ich erkläre, keine anderweitigen Promotionsversuche unternommen und die vorliegende Dissertation weder in der jetzigen noch in einer anderen Fassung einer anderen wissenschaftlichen Einrichtung vorgelegt zu haben.

Halle (Saale), den

Lucas Löser